ISSN en trámite

Geofísica Internacional

Revista Trimestral Publicada por el Instituto de Geofísica de la Universidad Nacional Autónoma de México

México
Volume 58 Number 1
January - March
2019

— Geofísica Internacional —

GEOFÍSICA INTERNACIONAL, Año 58, Vol. 58, Núm. 1, enero - marzo de 2019 es una publicación trimestral, editada por la Universidad Nacional Autónoma de México, Ciudad Universitaria, Alcaldía Coyoacán, C.P. 04150, Ciudad de México, a través del Instituto de Geofísica, Circuito de la Investigación Científica s/n, Ciudad Universitaria, Alcaldía Coyoacán, C.P. 04150, Ciudad de México, Tel. (55)56 22 41 15. URL: http://revistagi.geofisica.unam.mx, correo electrónico: revistagi@igeofisica.unam.mx. Editora responsable: Andrea Rostan Robledo. Certificado de Reserva de Derechos al uso Exclusivo del Título: 04-2022-081610251200-102, ISSN: en trámite, otorgados por el Instituto Nacional del Derecho de Autor (INDAUTOR). Responsable de la última actualización Saúl Armendáriz Sánchez, Editor Técnico. Fecha de la última modificación: 31 de diciembre 2018, Circuito de la Investigación Científica s/n, Ciudad Universitaria, Alcaldía Coyoacán, C.P. 04150, Ciudad de México.

Geofísica Internacional

Vol. 58, Núm. 1, enero-marzo de 2019

Contents

Prólogo

"En otro tiempo el fondo del cráter estaba silencioso como una tumba abandonada. Sólo turbaba su sepulcral silencio la caída de los peñascos que el viento arrancaba de sus bordes. Hoy, el viejo sepulcro se ha convertido en una fragua."
"En el fondo, una enorme prominencia se levanta como una flor de fuego, y a su alrededor largas fumarolas, pistillos ondulantes, forman movible corona. Las fuerzas interiores se han abierto paso por entre los peñascos que taparon la antigua boca y la lava hierve entre escorias, con fúlgido esplendor."
"Violentas explosiones remueven el líquido candente. Brotan, silbando, gruesos chorros de vapor y de humo mezclados de partículas de lava, de piedras y de cenizas. Llueven peñascos y lumbre. Un rumor trepidante sacude la Montaña y en el enorme agujero fulgura y ruge la sangre del Planeta."
(Gerardo Murillo, Dr Atl, 1921. "En el fondo del cráter", de las Sinfonías del Popocatépetl, Ediciones México Moderno.)
Esta vívida descripción del inicio de la erupción de domos de lava entre marzo de 1919 y junio de 1920, la que se prolongó hasta 1927 puede aplicarse en gran medida a lo ocurrido entre diciembre de 1994 y marzo de 1996, periodo en el que se inicia la segunda erupción de domos de lava del Popocatépetl en el Siglo XX. Esta erupción continúa hasta la fecha, y para el 25 aniversario de su inicio, GEOFÍSICA INTERNACIONAL invitó a la comunidad científica internacional a someter los resultados de sus investigaciones para ser incluidos en los dos primeros números de 2019. Aunque estos números son conmemorativos del inicio del actual episodio eruptivo, sus contenidos no son exclusivos del tema volcánico, ya que también incluyen artículos de otros tópicos de las ciencias de la Tierra, que mantienen la diversidad que caracteriza a nuestra Revista. Esperamos que nuestros lectores encuentren estos contenidos útiles e interesantes.

Servando De la Cruz Reyna
Editor Jefe

Roberto Carniel
Editor de Vulcanología

Andrea Rostan Robledo
Editora Técnica

Foreword

"Once, the bottom of the crater was silent like an abandoned grave. The sepulchral silence was only disturbed by the fall of crags that the wind ripped from its edges. Today, the old tomb has become a forge."
"In the crater bottom, a huge prominence rises like a flower of fire, and around it long fumaroles, undulating pistils, form a movable crown. The internal forces have made their way through the crags that covered the old mouth, and now the lava boils between slags, with flaring splendor."
"Violent explosions remove the red-hot liquid. Bristling, whistling, thick jets of steam and smoke mixed with lava particles, stones and ashes. Boulders and fire rains. A dreadful murmur shakes the Mountain and in the enormous hole it flares and roars the blood of the Planet."
(Gerardo Murillo, Dr Atl, 1921. "En el fondo del cráter", from Sinfonías del Popocatépetl, México Moderno Eds.)
This vivid description of the eruption of lava domes onset between March 1919 and June 1920, which lasted until 1927, can be freely applied to what happened between December 1994 and March 1996, a period in which the second 20th century lava domes eruption of Popocatépetl began. This eruption continues to the present, and for the 25th anniversary of its beginning, GEOFÍSICA INTERNACIONAL invited the international scientific community to submit results of their research to be included in the first two issues of 2019. Although these numbers are commemorative of the beginning of the current eruptive episode, their contents are not exclusive to the volcanic theme, since they also include other topics of the Earth sciences to maintain the diversity that characterizes our journal. We hope our readers find these contents useful and interesting.

Servando De la Cruz Reyna
Editor-in-Chief

Roberto Carniel
Editor of Volcanolgy

Andrea Rostan Robledo
Technical Editor

Geofísica Internacional (2019) 58-1: 7-32

Original paper

A vulnerability-based risk assessment of the threatened area surrounding Popocatépetl Volcano to support decision-making during a volcanic crisis

Esteban Ramos Jiménez

Received: June 13, 2017; accepted: October 04, 2018; published on line: January 18, 2019

Resumen

El volcán Popocatépetl, ubicado en la parte central de México, se encuentra rodeado por una región densamente poblada que excede los 20 millones de habitantes. Su actividad histórica de los últimos 500 años se ha limitado a varias erupciones de pequeñas a moderadas, análogas al episodio actual (1994 al presente). Sin embargo, desde la destrucción del cono ancestral hace unos 23 000 años B.P., el Popocatépetl ha dado lugar a una amplia gama de erupciones tanto en tamaño como en tipo, incluyendo eventos plinianos y colapsos masivos de sector.

Muchas de de las erupciones mayores han dado lugar a grandes volúmenes de material de caída de tefra que se han extendido al menos unos 20 kilómetros hacia el sureste, entre 10 y 15 kilómetros al noreste y 15 a 18 kilómetros en el sector oeste. Sin embargo, la mayoría de los eventos plinianos cubrieron áreas más extensas con material de caída de pómez, flujos de piroclásticos y depósitos de lahar. Basados en la distribución actual de población y de los asentamientos humanos, y considerando la experiencia de evacuación efectuada durante los picos de actividad volcánica, en este trabajo se ha desarrollado una evaluación del riesgo basado en la vulnerabilidad de las áreas amenazadas alrededor del Popocatépetl, con la finalidad de apoyar la toma de decisiones ante una potencial crisis volcánica.

Palabras clave: Popocatépetl, volcán, crisis, riesgo, evaluación, decisiones.

Abstract

Popocatépetl Volcano, located in central Mexico, is surrounded by a densely populated region exceeding 20 million people. The activity of Popocatépetl in the past 5 centuries has been limited to several small to moderate eruptions, similar in style to the current eruptive episode (1994-present). However, since the destruction of an ancestral volcano 23 000 years B. P., Popocatépetl has produced eruptions ranging widely in size and style, including Plinian events and massive sector collapses. Many of the major eruptions have resulted in large volumes of tephra-fall deposits that typically extended at least 20 kilometers to the southeast, about 10 and 15 kilometers to the northeast, and 15 to 18 kilometers to the west. Moreover, some Plinian events have covered much larger areas with pumice-fall, pyroclastic flows and lahar deposits. Based on the present distribution of population and settlements, and considering the experience of evacuations carried out during peaks of the ongoing volcanic activity, in the present work a vulnerability-based risk assessment of the threatened area surrounding Popocatépetl Volcano has been developed. This assessment can provide additional information to support decision-making during the on-going volcanic crisis.
.

Key words: Popocatépetl, volcano, crisis, risk, assessment, decisions.

E. Ramos Jiménez
Posgrado en Ciencias de la Tierra
UNAM
Instituto de Geofísica

Coordinación General de Protección Civil
del Estado de México
Km 36.5 Carretera Federal México-Pachuca
C.P. 55740, Tecámac, México
Corresponding author: investigacion10@yahoo.com.mx

Introduction

The management of volcanic risk must be supported by a variety of information elements that permits the decision making during an event of volcanic crisis. A useful approach to such management requires that the information elements are defined and prepared well in advance of a potential volcanic activity. For instance, together with hazard maps, it is essential to consider, and analyze, the likely scenarios that may occur in a potential crisis.

Another important crisis-management tool is the event tree (Newhall and Hoblitt 2002), and the more probabilistically oriented Bayesian Event Tree (Marzocchi *et al*., 2008). Such tools assign probabilities to the scenarios inferred from the hazards maps according to the progression of the volcanic activity. An application of the event-tree analysis to the hazard assessment of a specific type of pyroclastic flows at Arenal Volcano in Costa Rica is illustrated in Meloy (2006), who estimated the occurrence probabilities of possible eruptive events based on the activity of previous years. Similarly, Martí *et al*. (2008) developed a risk event tree for Teide-Pico Viejo volcanoes (Canary Islands, Spain), which also involved geology, eruptive history and present activity, as a useful tool for decision-making by civil protection authorities. Neri *et al*. (2008), and Sandri *et al*. (2009) applied event-tree methodologies to Vesuvius Volcano in Italy, extending the event concatenation from precursors along a progressive activity, then focusing on diverse eruption types and associated phenomena, such as ballistics ejection, lava flows, lahars, collapses and tsunamis in the Naples coastal zone and surrounding area. The tree branching was based on the eruptive record and data from the ongoing monitoring. Ideally, the integral management of the volcanic risk should include extensions of the event tree to describe the possible crisis scenarios and the corresponding methods of management.

However, studies focused on the management of volcanic crises are not as profuse in the scientific literature as those mentioned previously to assess the volcanic hazards. Managing a major emergency is a very complex task, and requires the deployment of considerable resources.

Frequently, evacuations are prompted by diverse circumstances, including: incorrect perception of the hazard by the threatened population and civil authorities, and failures of the response systems (Kent 1994, Leonard *et al*. 2008, Marrero *et al*. 2013); inadequate emergency plans (Sorensen 2000, Solana *et al*. 2008, Marrero *et al*. 2012); lack of protocols (Mener 2007, Solana *et al*. 2008); deficiencies in the communication of alerts, warnings and instructions (De la Cruz-Reyna and Tilling 2008, Paton *et al*. 2008, Haynes *et al*. 2008, Johannesdottir and Gisladottir 2010).

In this work we describe some methods to develop a vulnerability-based risk assessment methods of the threatened areas surrounding Popocatépetl Volcano, aiming to support decision-making during the ongoing volcanic crisis. The proposed methods would be compatible with a branching method to be inserted in an integral-management event tree (Newhall and Hoblitt 2002, Marzocchi *et al*. 2008, Sandri *et al*. 2009). Figure 1 shows an example of an event tree that initiates from a condition of low-level background activity at Popocatepetl volcano, and the branches represent subsequent events according to possible paths of activity evolution, according to the past events reaching a possible outcome, in this case the maximum observed event of December 2000-January 2001.

Popocatépetl Volcano

Popocatépetl Volcano, rising 5,452 m. a. s. l., is located at 19^0 01.38' N and 98^0 37.29' W, on the southern end of the Sierra Nevada, which separates the valleys of Mexico and Puebla. The recent eruptive history of this volcanic edifice begins 23,000 years B.P, when the pre-existing ancestral Popocatépetl collapsed, generating massive debris avalanches (Robin and Boudal 1987; Boudal and Robin 1989; Siebe *et al*., 1995). Since then, its activity has been characterized by several major explosive eruptions and many smaller eruptions. The most recent explosive eruptions occured ca. 3000 B.C., between 800 and 200 B.C., and ca. 800 A. D. (Siebe *et al*., 1996; Siebe and Macías 2004). Afterwards, the activity of Popocatépetl has remained moderate for nearly 1,200 years. Historical reports since 1354 describe at least 19 episodes of activity, some of which probably involved dome growth-and-destruction processes similar to those of the current, ongoing activity (De la Cruz-Reyna *et al*., 1995; De la Cruz-Reyna and Tilling 2008, De la Cruz-Reyna *et al.,* 2017).

The proximity of Popocatépetl with large population centers (Table 1) such as The Metropolitan Area of Valley of Mexico to the NW; Puebla City, 42 kilometers to the NE; Cuernavaca City, 65 kilometers to the SW (INEGI, 2010); and a myriad of smaller

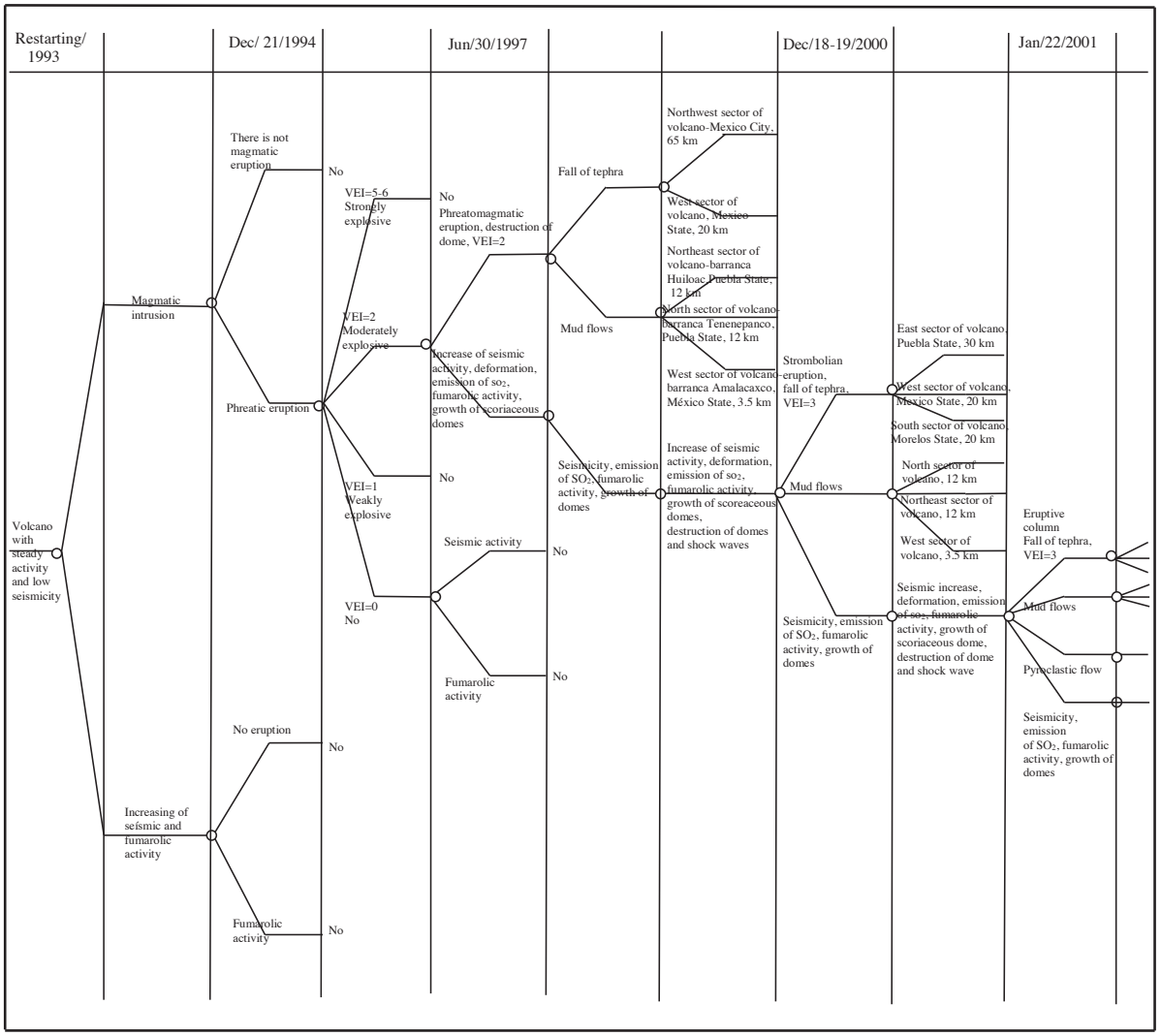

Figure 1. Example of an event tree for Popocatépetl Volcano, according to the methodology of Newhall and Hoblitt (2002) that starting from a background condition, it evolves to different conditions from 1993 until 2001.

settlements in the States of Mexico, Morelos, and Puebla, with the above mentioned diversity of eruptive styles makes Popocatépetl a high risk volcano. It is therefore necessary to continue developing, and refining, decision-making tools to reduce risk, in the event of a possible future major escalation in the ongoing crisis. Popocatépetl's most recent eruptive activity previous to the current 1994-present episode was during 1919-1927, which has been described in detail by several authors (Waitz 1920b, 1921; Weitzberg, 1922, 1923; Camacho, 1925; Atl, 1939; Gómez-Vázquez A. *et al*., 2016). The 1919-1927 activity has helped to define the lower bound of the most likely scenarios for evolution of the present activity.

Table 1. Areas influenced by the activity of the Popocatépetl Volcano and its corresponding populations (INEGI, 2010).

Zone	Population
Metropolitan area of Valley of Mexico	19,764,540
Puebla City	1,539,819
Cuernavaca City	365,168
Myriad of smaller settlements, in the States of Mexico, Morelos, and Puebla	1,040,979

Methodology

To carry out a vulnerability-based risk assessment in a readily accessible platform we use Google Earth (Google™ Earth, *V 7.1.5 1557*), since its easy of use, and has a wide accessibility to the general public. To do this, all the field information is incorporated in the same platform, which can be interacted with new field information that may arise over time.

We selected a quadrant (Figure 2) that delimits a sufficient area to include the risk areas shown on the hazard map of Popocatépetl Volcano (Macías *et al*., 1995a; Arana *et al*., 2016). Within that quadrant (indicated by red rectangle) the following parameters of information are included:

- The areas with high, medium, and low risk, are delimited by digitized red, orange and yellow lines, respectively.

- The villages of high risk for the three states (indicated by red squares in Figure 3, are located within the area bounded by the red line. Digital information for each village includes: its official name and municipality; geographic coordinates and altitude above sea level; their most recent population according to the emergency planning map; their meeting place with address; the alerting device; the detailed evacuation route to its designated temporary shelter with address and capacities; distance in km to the shelter and travel time in minutes from the village to its designated shelter. The latter may vary depending on weather conditions.

- The villages of medium risk (indicated by orange squares) are represented in the zone between the orange and red lines (Figure 4). Each of these villages includes the same type information as in (b).

- The villages of low risk (indicated by green squares) are represented in the zone between the yellow and orange lines (Figure 5). Each village also includes the same type of information as in (b).

- Figure 6 shows the most important drainages capable of channeling lahars (marked in dark blue), as well as the communities (blue squares) exposed to this hazard; some larger communities also appear as polygons (light blue). Each community includes the same type of information as in (b), but it also includes the populations bordering the valley that must move to higher ground in case of mudflows.

All data used in these maps were obtained in the field through direct visits to each town in the area. Each of the evacuation routes was tracked directly in the field to identify the optimum traffic control points.

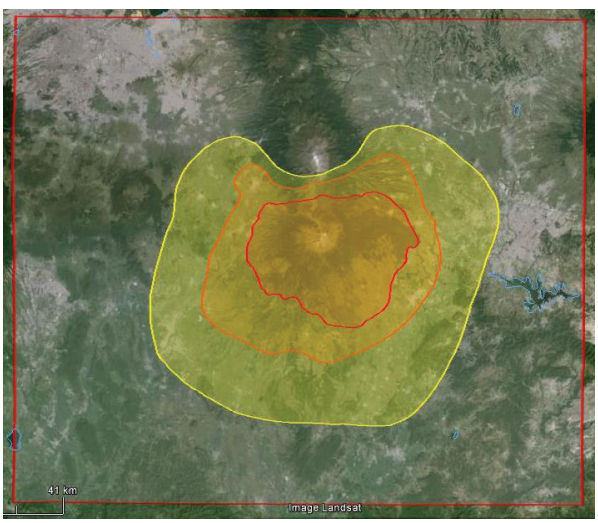

Figure 2. Quadrant delimited by points P1(190 27’ N, 990 16’ W; P2(190 27’ N, 980 05’ W); P3(180 30’ N, 990 16’ W) and P4(180 30’ N, 980 05’ W) covering a sufficient area to include the hazard map of the Popocatépetl Volcano (Macías *et al.*, 1995a, Arana *et al.*, 2016).

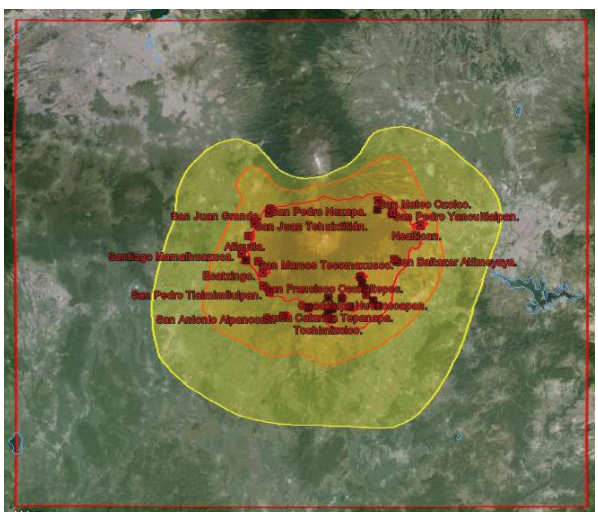

Figure 3. High risk villages for the states of México, Morelos and Puebla.

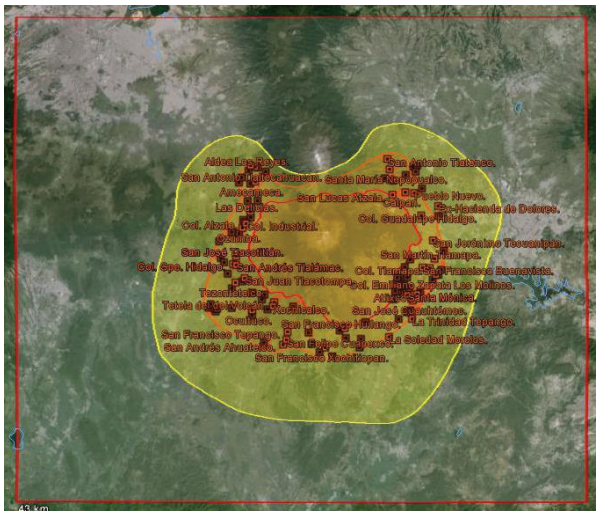

Figure 4. Villages with medium risk in México, Morelos and Puebla States.

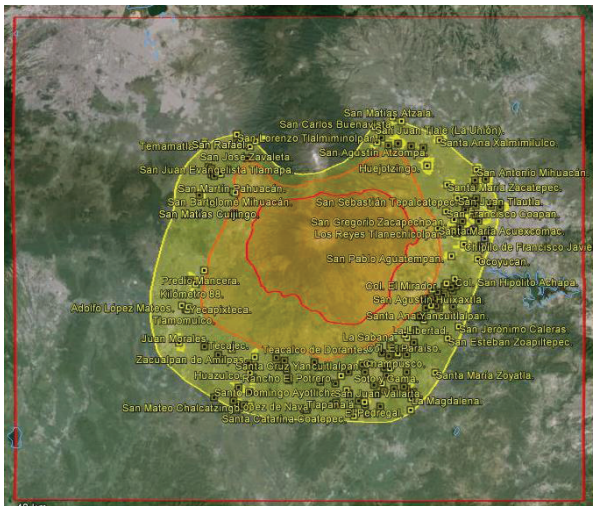

Figure 5. Villages with low risk in México, Morelos and Puebla States.

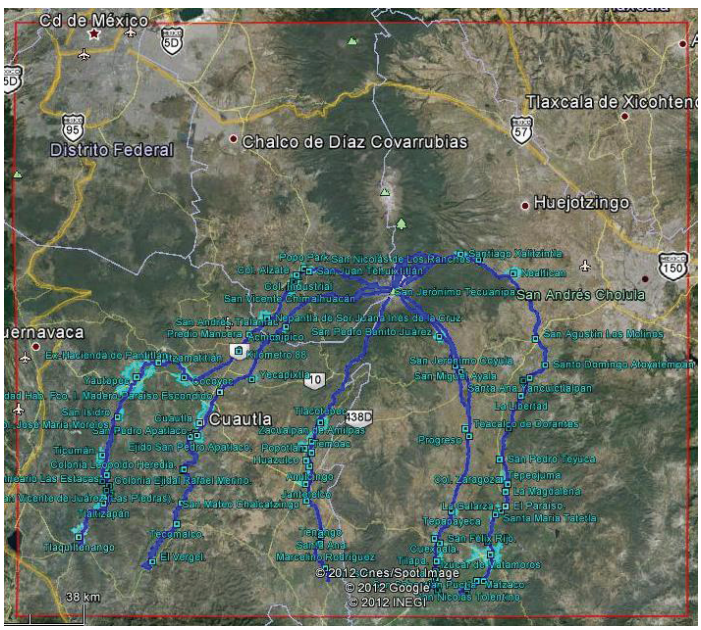

Figure 6. The most important drainages from the point of view of potential risk from lahars in México, Morelos and Puebla States.

Eruptive period, from December 21, 1994 to the present

The most important features of the current eruptive episode of Popocatépetl are summarized in Table 2 (Appendix 1), in reverse chronological order from 2017 to 1994. The analysis and communications of such features have influenced the perceptions of the volcanic hazards among the population and civil authorities, their reactions to different levels of activity and the choice of meeting places, escape routes and shelter locations, which in addition to the available hazard maps (Macías *et al*., 1995a; Arana *et al*., 2016) provided the basic data and criteria utilized in this present work.

Settlements within high-risk areas around Popocatépetl Volcano

The villages located within the high-hazard areas around Popocatépetl Volcano are as follows: Eight in the State of México (Table 3), two in the State of Morelos (Table 4) and twenty in the State of Puebla (Table 5).

Table 3. Villages with high risk in State of México.

VILLAGE	MUNICIPALITY	RISK SECTOR	POPULATION
San Pedro Nexapa	Amecameca	1-7	4,633
San Juan Grande	Amecameca	1-7	429
Atlautla de Victoria	Atlautla	1-7	10,967
San Juan Tehuixtitlán	Atlautla	1-7	6,743
San Juan Tepecoculco	Atlautla	1-7	3,790
Ecatzingo de Hidalgo	Ecatzingo	1-7	7,058
San Marcos Tecomaxusco	Ecatzingo	1-7	1,022
Santiago Mamalhuazuca	Ozumba	1-7	2,182
Total: 8	4		36,824

Information taken from INEGI, 2010.

Table 4. Villages with high risk in Morelos State.

VILLAGE	MUNICIPALITY	RISK SECTOR	POPULATION
San Francisco Ocoxaltepec	Ocuituco	1-6	1,338
San Pedro Tlalmimilulpan	Tetela del Volcán	1-6	1,637
Total: 2	2		2,975

Information taken from INEGI, 2010.

Table 5. Villages with high risk in Puebla State.

VILLAGE	MUNICIPALITY	RISK SECTOR	POPULATION
San Mateo Ozolco	Calpan	1-2	2,713
San Nicolás de los Ranchos	San Nicolás de los Ranchos	1-2	5,685
San Pedro Yancuitlalpan	San Nicolás de los Ranchos	1-2	2,694
Santiago Xalitzintla	San Nicolás de los Ranchos	1-2	2,196
San Baltazar Atlimeyaya	Tianguismanalco	1-3	1,104
San Pedro Atlixco	Tianguismanalco	1-3	867
San Pedro Benito Juárez	Atlixco	1-3	3,153
San Juan Ocotepec	Atlixco	1-3	825
Colonia Agrícola Ocotepec	Atlixco	1-3	1,898
Guadalupe Huexocoapan	Atlixco	1-3	442
San Miguel Ayala	Atlixco	1-3	1,628
San Jerónimo Coyula	Atlixco	1-3	6,622
Tochimilco	Tochimilco	1-4	3,289
La Magdalena Yancuitlalpan	Tochimilco	1-4	2,210
San Martín Zacatempan	Tochimilco	1-4	721
San Miguel Tecuanipan	Tochimilco	1-4	1,378
Santa Catalina Cuilotepec	Tochimilco	1-4	439
Santa Catarina Tepanapa	Tochimilco	1-4	681
Santa Cruz Cuautomatitla	Tochimilco	1-4	1,405
Santiago Tochimizolco	Tochimilco	1-4	747
Total: 20	6		40,697

Information taken from INEGI, 2010.

Operational (response) plans for Popocatépetl Volcano

When the most recent activity of Popocatépetl began, on December 21, 1994, the States of Mexico, Morelos, and Puebla States began to develope their respective response operational plans within the framework of the National System of Civil Protection, involving the three levels of government: federal, state and municipal, and the social and private sectors of each state (Figure 7).

In such operational plans, all participating offices are governed according to liability matrices defining their specific functions, under the constitutional headship of the Governor of each state. Such governance includes the emergency coordination, emergency plans, warning, evacuation, temporary shelters, public safety, supplies, strategic services, equipment and goods, search of missing people, rescue and assistance, medical attention, damage assessment and emergency social communications. Since Civil Protection authorities may change when are state elections (usually every 6 years), occur one of the objectives of the present work is to maintain the conceptual framework to help new officials in understanding and implementing the operational plans.

Temporary shelters

The sites to serve as temporary shelters –in case of volcanic emergency- in the states of México, Morelos, and Puebla were selected in different localities (Figure 8), necessarily outside the volcanic risk area. The shelters for the same three states which are generally schools are indicated as green small house icons with a flag, with their geographical location, height above sea level, address and capacity.

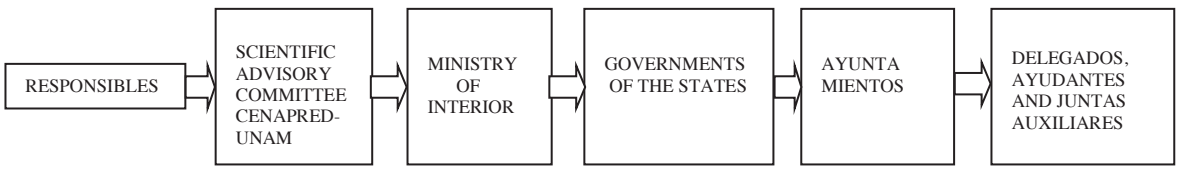

Figure 7. Activation Diagram for Popocatépetl Volcano Operative Plan (Decision Making).

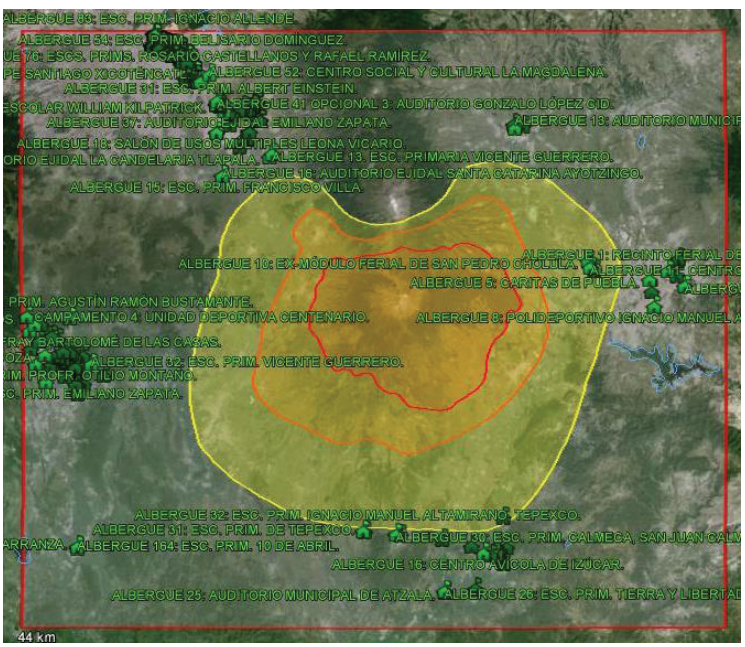

Figure 8. Locations of the temporary shelters of the States of México, Morelos and Puebla, which are outside the risk area.

A prime prerequisite for their selection was that they had the necessary infrastructure to provide the necessities and services required by the expected amount of people during their stay, such as: drinking water, electricity, telephone, toilets, showers, sleeping area, kitchen area and mess halls; recreational areas, medical service, psychological support, and religious and worship services. The establishments that were considered for use during a possible contingency include schools of all levels (from kindergarten to high schools), CONALEP (National College of Technical Vocational Education), CEBETIS (Center for Technical, Industrial and Services Studies), gymnasiums, halls of multiple uses, social and cultural centers, municipal and farmer halls; exhibition fairs sites, sports center sites, trade union buildings, Rotary and Lion clubs, among others. The number and capacities of the temporary shelters of the States of México, Morelos, and Puebla are summarized in Table 6.

Response and evacuations during the eruptive episode of December 18-19, 2000

On December 18-19, 2000, Popocatépetl activity occured and a contingency situation was developed. The available operational plans for each of the States at the time allowed to deal with that contingency. However, some difficulties arose during the contingency, particularly the overreactions in some towns; these problems were among the reasons to undertake the present study. The plans required, as a first stepts, rais the awareness of the risks related to volcanic activity, among the populations of the three States, through talks, lectures, brochures, calendars, evacuation drills (at least three in México State, eight in Puebla, and five in Morelos in 2000), radio spots at the most popular broadcasting stations in high-risk areas, and improvement of roads and highways with the construction of some bridges and beltways like in Atlautla, State of México. Additionally, there were early agreements reached with associations of taxis and minibuses, commercial carriers and private vehicles that could be used at for evacuation, in the case of a contingency.

The increase in volcanic activity, the associated intensity in the volcano-monitoring, and the persistence of energetic harmonic tremor, prompted the Scientific Advisory Committee (SAC) to recommend to the authorities of the National Coordination of Civil Protection of SEGOB to rise the level of alert, particularly for the most vulnerable communities at risk, considering the increased probability of a major eruptive event. The SAC advised that such activity may pose a threat on settlements located in zone 1 of higher risk, according to the existing map of hazards of Popocatépetl (Macías *et al*. 1995a). In addition the SAC noted the increasing probability of damage to settlements located along river valleys that could channel destructive lahars. Such lahars potentially could be generated by erosion and melting of glaciers in the north and northwest sectors of the volcanic cone caused by potential pyroclastic flows.

Therefore, on December 15, 2000, a declaration of emergency was issued in the Diario Oficial de la Federación (2000)

Table 6. Temporary shelters established in México, Morelos, and Puebla States. (Tabulated from data in: Plan Operativo Popocatépetl (2012); Plan Fuerza de Tarea Popocatépetl (2001); Plan de Protección Civil para el Volcán Popocatépetl (2000); Programa Especial para la Emergencia del Volcán Popocatépetl (2007).

STATE	TOTAL NUMBER OF SHELTERS	TOTAL CAPACITY (PEOPLE)
Edo. Mex.	114	34,830
Morelos	42	12,048
Puebla	34	38,561
Total: 3	190	85,439

Note: Additionally, for Puebla State temporary shelters are contemplated for 237 schools in Puebla municipality, 33 schools in San Pedro Cholula municipality, six schools in San Martin Texmelucan and 67 schools in Izúcar de Matamoros municipality.

that involved the release of funds from the Emergency Reserve of Fund for the Emergency Care (FONDEN) (http://www.proteccioncivil.gob.mx/work/models/ProteccionCivil/Resource/21/12/images/Definicion%20del%20FAE.pdf). Accordingly, the three States, through their State Systems of Civil Protection (General Directorate of Civil Protection in México State, General Directorate of Civil Protection in Morelos State, and State System of Civil Protection in Puebla), coordinated with the federal Civil Protection to start evacuation operations. These actions involved: 13 communities in the México State (with 28,539 persons); three communities in the State of Morelos (with 2,720 persons), and 20 communities in six municipalities of the State of Puebla (with 55,281 inhabitants). Of the total of 86,540 persons affected, 8,592 people who were transported via 13 evacuation routes remained at 23 temporary shelters of the México State (Memoria de las Acciones del Plan Operativo Volcán Popocatépetl del 15 al 27 de Diciembre del año 2000). In the State of Morelos, four temporary shelters and four evacuation routes were used to transport and accommodate a total of 2,664 people (Contingencia Volcánica Morelos, Diciembre 2000); and the State of Puebla housed 8,289 people in 23 shelters, transported via 10 evacuation routes (Resumen de las acciones llevadas a cabo durante la evacuación de las comunidades aledañas al volcán Popocatépetl en Diciembre de 2000). Of the remaining population (nearly 66,995), some self-evacuated to other places, mainly to homes of friends or relatives outside the risk areas, while others decided not to leave. In high-risk areas of the State of Puebla, about 1,598 people expressed their reluctance to leave (Resumen de las acciones llevadas a cabo durante la evacuación de las comunidades aledañas al volcán Popocatépetl en Diciembre de 2000), while in the State of México 11,360 people were not evacuated (Memoria de las Acciones del Plan Operativo Volcán Popocatépetl del 15 al 27 de Diciembre del año 2000). There is no report from Morelos State.

In the areas of highest risk, 20 towns in Puebla State, 8 in México State, and 2 in Morelos State were evacuated; in areas of intermediate risk, also 5 towns in México State, 1 in Puebla State, and 2 in Morelos State were evacuated. In addition, the San Buenaventura Nealtican community in Puebla was evacuated, because it was in the lahar flow path along the Huiloac ravine, which originates on the north side of the volcanic cone, at the glacier which potentially could be eroded and melted by pyroclastic flows. In México State, San Diego Huehuecalco, San Juan Tlacotompa, San Andrés Tlalámatl, Colonia Guadalupe Hidalgo and San José Tlacotitlán (Memoria de las Acciones del Plan Operativo Volcán Popocatépetl del 15 al 27 de Diciembre del año 2000); and in Morelos Huecahuaxco and Hueyapan were also evaluated (Contingencia Volcánica-Morelos Diciembre 2000).

Evacuation operations began in all the towns simultaneously on December 15, 2000, and involved the respective State Units of civil protection, the National Coordination of Civil Protection of SEGOB, and the National Center of Disaster Prevention. The Scientific Advisory Committee closely followd the evolution of the volcanic activity.

The eruption reached its maximum intensity on December 18 and 19, after which it decreased gradually, until it was decided on December 27 to allow all evacuees to return to their homes.

Evacuation routes

Evacuation routes around Popocatépetl Volcano were chosen after a comprehensive analysis of the existing roads and dirt tracks, to determine which were the most efficient and fastest access between the endangered towns and the sites of the temporary shelters designated by civil protection authorities of the states of Mexico, Morelos, and Puebla. Along each evacuation route, transit control points are included to prevent evacuation vehicles using a wrong route. In these control points state and municipal traffic officers should remain to ensure the secure flow during a contingency. To improve the capacity of the routes, some of them were paved or repaved, some bridges were expanded, and others constructed. Some dangerous curves were realigned, and some beltways roads were built to bypass towns and population centers, as was the case for the Atlautla-Popo Park beltway. In such manner this way, six routes for the western sector of the volcano, corresponding to State of México, were selected (Appendix 2, Figures 9 to 14). In the State of Morelos, evacuation routes for two villages with high risk were established in the southern sector of the volcano (Appendix 2, Figures 15 and 16), and for the State of Puebla on eastern side of volcano, ten evacuation routes were established (Appendix 2, Figures 17 to 25; the Figure 19 contents evacuation routes 3 and 4).

Distances and travel times between the meeting sites of high-risk villages

For decision-making to be effective during a volcanic crisis in an effective risk-management scheme, it is essential to know the travel times between key geographic points (Marrero et al., 2013). To measure the travel times between the settlements located in the high-risk areas and the temporary shelters, timed journeys at average speeds of 40 km/h with support of urban buses were performed along the evacuation routes marked in each of the state's operational plans (Mexico, Morelos and Puebla). With this information, time-distance tables and plots have been prepared to support evacuation decision-making and planning.

For the purpose of this paper, we present only four examples of high-risk settlements in the State of México (Appendix 3, Tables 7 to 10 and Figures 26 to 29), two in the State of Morelos (Appendix 3, Tables 11 and 12, and Figures 30 and 31), and four in the State of Puebla (Appendix 3, Tables 13 to 16, and Figures 32 to 35). The complete set of travel-time data and plots may be consulted in Ramos (2018).

Meeting sites for the population in case of volcanic contingency

Civil-protection authorities of each state, together with municipality officials, jointly defined meeting points (or assembly or gathering places) for the population in case of contingency, as occurred in December 18-19, 2000. In most cases, such meeting points were set in the central parts of towns or at the municipal city halls, such as: near the Municipal Delegations at the State of México; near the Municipal Inspector and Auxiliary Presidencies at Puebla State; and near the Municipal Assistantships in the state of Morelos. In some cases, meeting sites were designated at other locales, such as: municipal and communal auditoriums; civic squares, near civil courts, chapels and shrines, elementary and secondary schools, sports fields, markets, at jagüeyes (small natural water dams), meeting rooms, roundabouts, squares, parks and gardens, in culture houses, trade unions and in offices of agricultural commissions.

Warning system and alerting devices

The general warning system used in Mexico is the Traffic Light Alert System TLAS (De la Cruz-Reyna 1995, 1996; De la Cruz-Reyna and Tilling, 2008; De la Cruz-Reyna et al., 2017). The colors universally used for Traffic lights indicate the level of warning and awareness of the population, and the phases within each of the three colors (green, yellow and red) indicate the level of response of the Civil Protection authorities. The way in which these levels are communicated to the population may vary between different towns. During a contingency, in the case when the population must move to assembly points or meeting sites different alerting devices activated by every local authority are used, and these can include special ringing of bells in churches, rockets, sirens and loudspeakers, whistles of some local companies, systems of particular sounds, paging with sound in private vehicles, sirens of ambulances, local broadcasting stations, and home announcements. Mass media such as radio and television stations, internet, newspapers, etc. are also widely used.

Discussion and conclusions

Decision-making during a volcanic crisis situation is a highly complex problem involving volcanological, social, economic, health, cultural, meteorological, and other factors. This complexity makes it very difficult to develop a general methodology for the management of risk, particularly during episodes of enhanced volcanic activity, because the nature and dimension of the response critically depends on the progression of the activity, and on the related spatial distribution of hazard and exposure. An optimal mitigation of risk requires a layout of information and criteria that provides the Civil Protection and other authorities of the factors needed for appropriate decision-making. The present work intends to provide a risk-management tool to assist the involved stakeholders in determining the appropriate and adequate level of response. This tool or layout -in the form of maps, tables, and data- that is described here builds on the experience of the risk management gained over more than 20 years of eruptive activity at Popocatépetl Volcano, including the response to some critical situations during which precautionary evacuations were necessary. The possibility of other scenarios corresponding to much larger eruptions, such as some that occurred in the geological record of Popocatépetl, are also considered indirectly.

Of particular importance is the use of the layout for the choice of evacuation routes, community-shelter links, and the determination of evacuation travel timings for different possible volcanic activity scenarios. Equally important, the layout can serve as a practical

communication tool among the involved municipal, state and federal authorities, as it constitutes a single database for all levels of government. Given a potential red-level alert of the TLAS in a region determined by the consensus of the Advisory Scientific Committee, the layout will assist municipal, state and federal authorities to develop and undertake -in a short time- the optimal, mitigative actions to reduce potential risks for the population affected. However, in order to remain valid and useful, the information in the database must be updated as frequently as possible.

Acknowledgements

This work was supported by the National Center of Disaster Prevention of SEGOB, Earth Science Postgraduate Program at the Institute of Geophysics UNAM, and Special thanks for the help provided by Arturo Mendez Ferrer of the Earth Sciences Library of UNAM.

References

Arana L., Bonasia R., Capra L., Córdoba G., Cortés J., Delgado H., Ferrés M. D., Fonseca R., García J. A., Gisbert G., Jaimes M. del C., Macías J. L., Martin A. L., Portocarrero J., Salinas S., Siebe C., Telles E., 2016, Grupo de trabajo para la actualización de los mapas de peligros del volcán Popocatépetl. SEGOB-UNAM.

Atl, 1939, Volcanes de México. La actividad del Popocatépetl. *Volumen 1, Editorial Polis, México; 74 p.*

Boudal C., Robin C., 1989, Volcán Popocatépetl: Recent Eruptive History, and Potential Hazards and Risks in Future Eruptions. In: Latter JH (ed.) Volcanic Hazards. IAVCEI Proceedings in Volcanology. Springer-Verlag Berlín: 110-128

Camacho H., 1925, Apuntes acerca de la actividad actual del volcán Popocatépetl en relación con la sismología. *Anales del Instituto Geológico de México. Páginas 38-60.*

Contingencia volcánica-Morelos, diciembre 2000, Dirección General de Protección Civil del Estado de Morelos, Elaborada en febrero de 2001.

De la Cruz-Reyna S., 1995, Un Código de Alerta para el Manejo de Emergencias Antes y Durante Potenciales Erupciones del Volcán Popocatépetl. En: "Volcán Popocatépetl Estudios Realizados Durante la Crisis de 1994-1995". Coedición del Sistema Nacional de Protección Civil, El Centro Nacional de Prevención de Desastres y la UNAM (ISBN: 970-628-127-4), pp. 327-333. (1995).

De la Cruz-Reyna S., 1996, Un Código de Alerta para el Manejo de Emergencias Volcánicas. En: "Riesgo Volcánico", R. Ortiz, Ed. Serie Casa de los Volcanes No. 5. Cabildo de Lanzarote-CSIC, I. Canarias, España (ISBN: 84-87021-34-4), pp. 181-187 (1996).

De la Cruz-Reyna S., Tilling R., 2008, Scientific and public response to the ongoing volcanic crisis at Popocatépetl volcano, México: importance of an effective hazards warning system. J. Volcanol. Geotherm. Res 170: 121-134.

De la Cruz-Reyna S., Tilling R. I., Valdés-González C., 2017, Challenges in responding to a sustained and continuing volcanic crisis: The case of Popocatepétl volcano, Mexico, 1994-present. En: OBSERVING THE VOLCANO WORLD: VOLCANO CRISIS COMMUNICATION. Ed. C.J. Fearnley, B. McGuire, G. Jolly, D. Bird and K. Haynes. A Springer-Verlag book, ADVANCES IN VOLCANOLOGY series. eBook ISBN 978-3-319-44097-2; Hardcover ISBN 978-3-319-44095-8. DOI: 10.1007/11157_2016_37.

Contingencia volcánica-Morelos, diciembre 2000, Dirección General de Protección Civil del Estado de Morelos, Elaborada en febrero de 2001.

Diario Oficial de la Federación, 2000, Declaratoria de Emergencia Preventiva para efectos de las Reglas de Operación del Fondo de Desastres Naturales (FONDEN), por el sensible incremento en la actividad del volcán Popocatépetl. – 15 de diciembre de 2000,- Primera Sección- Diario Oficial, No. 11.- 2 http://dof.gob.mx/nota_detalle.php?codigo=788168&fecha=15/01/2001

FONDEN, Fondo para la Atención de Emergencias, http://www.proteccioncivil.gob.mx/work/models/ProteccionCivil/Resource/21/12/images/Definicion%20del%20FAE.pdf

Gómez-Vázquez A., De la Cruz-Reyna S., Mendoza-Rosas A., 2016, The ongoing dome emplacement and destruction cyclic process at Popocatepetl volcano, Central Mexico. Bull. Volcanol. (2016) 78:58

Google™ Earth *Version 7.1.5 1557*

Haynes K., Barclay J., Pidgeon N., 2008, Whose reality counts? factors affecting the perception of volcanic risk. J Volcanol Geotherm Res 172(3):259–272

INEGI, 2010, Instituto Nacional de Estadística, Geografía e Informática, Censos 2010, http://www.inegi.org.mx/est/lista_cubos/consulta.aspx?p=pob&c=1 http://coespo.edomex.gob.mx/zonas_metropolitanas

Johannesdottir G., Gisladottir G., 2010, People living under threat of volcanic hazard in southern Iceland: vulnerability and risk perception. Nat Hazards Earth Syst Sci 10:407–420.

Kent R., 1994, Disaster preparedness guide. 2nd Ed. Disaster Management Training Programme. UNDP, UNDRO

Leonard G., Johnston D., Paton D., Christianson A., Becker J., Keys H., (2008), Developing effective warning systems: ongoing research at Ruapehu Volcano, New Zealand. J Volcanol Geotherm Res 172(3):199–215.

Macías J. L., Carrasco G., Delgado H., Martin A. L., Siebe C., Hobblit R. P., Sheridan M., Tilling R. I., 1995a, Mapa de Peligros del Volcán Popocatépetl. *Instituto de Geofísica, UNAM- CENAPRED, México, D.F. (Mapa y folleto explicativo de 12 páginas).*

Marrero J. M., Garcia A., Llinares A., López P., Ortiz R., 2012, Assessing the vulnerability of the evacuation emergency plan: the case of the El Hierro, Canary Island, Spain. Geophysical Research Abstracts Vol. 14, EGU2012-12374-2, 2012 EGU General Assembly 2012.

Marrero J. M., García A., Llinares A., De la Cruz-Reyna S., Ramos S., Ortiz R., 2013, Virtual tools for volcanic crisis management, and evacuation decision support: applications to El Chichón volcano (Chiapas, México) Natural Hazards (2013) 68: 955-980. doi:10.1007/s11069-013-0672-4.

Martí J., Aspinall W. P., Sobradelo R., Felpeto A., Geyer A., Ortiz R., Baxter P., Cole P., Pacheco J., Blanco M. J., López C., 2008, A long-term volcanic hazard event tree for Teide-Pico Viejo stratovolcanoes (Tenerife, Canary Islands). *Journal of Volcanology and Geothermal Research 178 (2008) 543-552.*

Marzocchi W., Sandri L., Selva J., 2008, BET_EF: a probabilistic tool for long- and short-term eruption forecasting. Bull Volcanol 70: 623-632. doi: 10.1007/s00445-007-0157-y

Meloy A. F., 2006, Arenal-type pyroclastic flows: A probabilistic event tree risk analysis. *Journal of Volcanology and Geothermal Research 157 (2006) 121-134.*

Memoria de las Acciones del Plan Operativo Volcán Popocatépetl del 15 al 27 de Diciembre del año 2000, Dirección General de Protección Civil del Estado de México. Sistema Estatal de Protección Civil.

Mener A., 2007, Disaster response in the United States of America: an analysis of the bureaucratic and political history of a failing system. PhD thesis, CUREJ: College Undergraduate Research Electronic Journal, University of Pennsylvania.

Neri W. P., Aspinall R., Cioni A., Bertagnini P. J., Baxter G., Zuccaro D., Andronico S., Barsotti P. D., Cole T., Esposti Ongaro T., Hincks G., Macedonio P., Papale M., Rosi R., Santacroce G., Woo G., 2008, Developing an Event Tree for probabilistic hazard and risk assessment at Vesuvius. *Journal of Volcanology and Geothermal Research 178 (2008) 397-415.*

Newhall, C. G.,·Hoblitt R. P., 2002, Constructing event tree for volcanic crisis. *Bull. Volcanol. (2002) 64:3-20.*

Paton D., Smith L., Daly M., Johnston D., 2008, Risk perception and volcanic hazard mitigation: individual and social perspectives. J. Volcanol. and Geotherm. Res. 172(3):179–188.

Plan de Protección Civil para el Volcán Popocatépetl, 2000, Gobierno del Estado de Puebla. 79 Páginas.

Plan Fuerza de Tarea Popocatépetl 2001, Dirección General de Protección Civil del Estado de Morelos. Gobierno del Estado de Morelos, 52 páginas.

Plan Operativo Popocatépetl, 2012, Gobierno del Estado de México, Dirección General de Protección Civil del Estado de México. 104 páginas.

Programa Especial para la Emergencia del Volcán Popocatépetl, Dirección del Plan Popocatépetl, 2007, Secretaría de Gobernación del Estado de Puebla, 38 páginas.

Quaas, R., González, R., Guevara, E., Ramos, E. y De la Cruz-Reyna, S., 1995. Monitoreo volcánico: instrumentación y métodos de vigilancia. Volcán Popocatépetl: Estudios realizados durante la crisis de 1994-1995. CENAPRED, p. 25-76.

Ramos E., 2018, Una evaluación de riesgos basada en la vulnerabilidad de la zona amenazada en torno volcán Popocatépetl para apoyar la toma de decisiones en una posible crisis volcánica. Tesis doctoral. 90 pág.

Resumen de las acciones llevadas a cabo durante la evacuación de las comunidades aledañas al volcán Popocatépetl en Diciembre de 2000, Gobierno del Estado de Puebla. Secretaría de Gobernación. Subsecretaría de Asuntos Políticos. Protección Civil-Dirección del Plan Popocatépetl.

Robin C., Boudal C., 1987, A gigantic Bezymianny-type event at the beginning of modern volcán Popocatépetl. J Volcanol Geotherm Res 31: 115-130

Sandri L., Guidoboni E., Marzocchi W., Selva J., 2009, Bayesian event tree for eruption forecasting (BET_EF) at Vesuvius Italy: a retrospective forward application to the 1631 eruption. *Bulletin of Volcanology. Vol. 71, pp. 729-745.*

Siebe C., Abrams M., Macías J. L., 1995, Derrumbes Gigantes, Depósitos de Avalancha de Escombros y Edad del Actual Cono del Volcán Popocatépetl. In: Volcán Popocatépetl, Estudios Realizados Durante la Crisis de 1994-1995. CENAPRED-UNAM, México, D.F, pp. 195-220.

Siebe C., Abrams M., Macías J. L., Obenholzner J., 1996, Repeated volcanic disasters in pre-Hispanic time at Popocatépetl, Central Mexico. Past key to the future? Geology 24: 399-402

Siebe C., Macias J. L., 2004, Volcanic hazards in the Mexico City metropolitan area from eruptions of Popocatépetl, Nevado de Toluca, and Jocotitlán stratovolcanoes and monogenetic scoria cones in the Sierra Chichinautzin. Volcanic Field guide, Penrose Conf. Neogene-Quaternary Continental margin Volcanism. Geol Soc Am, pp 1- 77

Solana M., Kilburn C., Rolandi G., 2008, Communicating eruption and hazard forecasts on Vesuvius, Southern Italy. J Volcanol Geotherm Res 172(3):308–314

Sorensen J., 2000, Hazard warning systems: review of 20 years of progress. Nat. Hazards Rev. 1(2):119–125

Waitz P., 1920b, La nueva actividad y el estado actual del volcán Popocatépetl. *Mem. de la Soc. Científica "Antonio Alzate". Tomo 37, México: 295-313.*

Waitz P., 1921, Popocatépetl again in activity. *Am. J. Sci. 5th Ser. V.1: 81-85.*

Weitzberg F., 1922, El ventisquero del Popocatépetl. *Memorias y Revista de la Sociedad Científica "Antonio Alzate". Tomo 41, N^{os} 2 y 3. Noviembre-diciembre de 1922.*

Weitzberg F., 1923, El ventisquero del Popocatépetl. *Memorias de la Sociedad*

Appendix 1

Table 2. Summary of recent eruptive history of Popocatépetl Volcano, 1994-2017.

YEAR	BRIEF DESCRIPTION OF ACTIVITY	REFERENCES
	In 2017, 58,217 exhalations of low to moderate intensity, 651 volcanic earthquakes with magnitudes between 1.0 and 3.7 and 300 hours with 51 minutes of harmonic tremor were recorded. Major exhalations occurred on May 18, July 3, August 14, September 27, October 5 and 12; and November 23 and 27.	
	In 2016, 38,454 exhalations of low to moderate intensity, 756 volcanic earthquakes with magnitudes between 1.0 and 3.8 and 548 hours with 13 minutes of harmonic tremor were recorded. Major exhalations occurred on January 16, 19, 20 and 22; February 17; March 29; April 3 and 18; July 31; and November 25 and 29.	
	In 2015, 23,164 exhalations, 193 volcanic earthquakes with magnitudes between 1.1 and 2.9; and 146 hours with 48 minutes of high frequency and low to moderate amplitude harmonic tremor were detected. Major exhalations occurred on February 15 and 24; and May 21.	
	In 2014, 21,320 exhalations of low to moderate intensity, 231 volcanic earthquakes with magnitudes between 1.0 and 3.2 and 39 hours with 57 minutes of high frequency and low-moderate amplitude harmonic tremor were recorded. Major exhalations occurred on August 31, October 7, 12 and 29; November 4 and December 8 and 18.	
	In 2013, 13,525 exhalations of low to moderate intensity; 331 volcanic earthquakes with magnitudes between 1.0 and 3.6 and 532 hours 26 minutes of harmonic tremor of high frequency and low and moderate amplitudes were recorded. Major exhalations occurred on 7 and 26 March; 13 and 18 April; 7, 11, 14 and 15 May; 17 and 18 June; and, 4, 7, 9, 10 and 12 July.	
	In 2012, 14,188 exhalations of low to moderate intensity, 150 volcanic earthquakes with magnitudes between 1.1 and 3.6, and 370 hours of high-frequency harmonic tremor with low to moderate amplitudes were detected. Major exhalations occurred on January 25; on April 13, 16 and 18; on May 3, 6 and 12; on August 6 and December 2.	
	In 2011, 2,616 exhalations of low to moderate intensity, 46 volcanic earthquakes with M<1.9. In addition, there were 47 hours with 41 minutes of harmonic tremor of high frequency and low-moderate amplitudes. Major exhalations occurred on January 31, May 22; 3, 4 and June 17; 9 and August 30; 26 and September 27; November 20 and December 8.	
	In 2010, 2,042 exhalations of low to moderate intensity, 25 volcanic earthquakes with M<1.8 and 42 hours with 31 minutes of high-frequency harmonic tremor were detected. Major exhalations occurred on May 25; 7, 9 and June 11 and August 23.	
2002-2017	In 2009, 3,351 exhalations of low to moderate intensity, 23 volcanic earthquakes with M<2.2 and 12 hours with 52 minutes of harmonic tremor of high frequency and low-moderate amplitudes were recorded. Major exhalations occurred on January 21, 6 and February 13, March 23, April 1, September 10, 9 and October 29 and 14 and November 21.	National Center for Disaster Prevencion
	In 2008, a total of 3,829 exhalations of low to moderate intensity, 32 volcanic earthquakes with M<2.9 and 31 hours with 2 minutes of	

	harmonic tremor of high frequency and low-moderate amplitudes were recorded. Major exhalations occurred on 4, 11, 14 and February 21. For 2007, 3,339 exhalations of low to moderate intensity, 93 volcanic earthquakes with M<3.1 and 51 hours with 9 minutes of harmonic tremor of high frequency and low-medium amplitude were recorded. Major exhalations occurred on January 6, November 26 and 1 and December 31. During 2006, there were 4,475 exhalations of low to moderate intensity, 112 volcanic earthquakes with M<3.0 and 69 hours with 20 minutes of harmonic tremor with low and high frequency and low and medium amplitude. Major exhalations occurred on 6, 25 and January 26; and July 25. During the 2005 5,747 exhalations of low to moderate intensity, 75 volcanic earthquakes with M<2.9 and 10 hours with 37 minutes of harmonic tremor of high frequency and low amplitude were recorded. Major exhalations occurred on 9 and January 22; March 9, June 23, 29 and July 30, 23 and October 24, 1, 4, 13, and December 25. In general, the recorded activity during this year also remained low and stable. For 2004, there were a total of 4,187 exhalations of low intensity, 55 volcanic earthquakes with magnitudes between 1.7 and 2.8 and 1 hour with 2 minutes of harmonic tremor low amplitude. In general, it is considered that the recorded activity during this year remained low and stable. In 2003 27 events involving emission of ash and incandescent fragments at short distances of the crater. Some of them provoked fires in nearby grassland. There were also reports of fall of ash on Santiago Xalitzintla and San Nicolás de Los Ranchos, of Puebla State; on Tetela del Volcán, Yecapixtla, Ocuituco, Atlatlahucan and Totolapan, inside of Morelos State; and on San Pedro Nexapa, San Diego Huehuecalco, San Juan Tehuixtitlán, Atlautla, Ozumba, Ecatzingo, Santiago Mamalhuazuca, San José Tlacotitlán, Tepetlixpa, Juchitepec, Tenango del Aire and Amecameca in México State. The most important event of July 19, caused to thin ash fall in most of Mexico City. In 2002 10 eruptive events occurred related with small explosions, accompanied by emission of ash and incandescent fragments over short distances of the crater. There were some reports of ash fall in San Pedro Nexapa, Ecatzingo and Tecomaxusco, in Edo. Mex.; Tetela del Volcán, in Morelos State; San Pedro Benito Juárez and some sectors of Puebla City.	
2001	Dome destruction activity continued throughout January 2001. A major explosion on January 22, destroyed a considerable part of the dome producing pyroclastic flows and an ash column 8 km of high above the summit and some mud flows. None of these phenomena affected the population; although a few houses were flooded with a mud deposit as much as 60 centimeters thick.	National Center for Disaster Prevencion
2000	On 10 and May 24 small lahars flowed through the Tenenepanco gully. In November 1 is detected a sudden increase in the volcano's internal activity. From December 10, large amplitude harmonic tremors with increasing duration and intensity were recorded for several days. On 12 December 200 exhalations are recorded per day, some of them reaching 5 to 6 kilometers over the volcano summit, and glow within the crater. This type of activity continued for three days, causing light ash falls on communities around the volcano. On December 15, the harmonic tremor signal saturated monitoring seismograms and were recorded at seismological stations at 150 km from Popocatépetl. These signals could be felt in some communities close to the volcano. After 10 hours of intense tremor, the activity of the volcano waned abruptly	National Center for Disaster Prevencion Gómez-Vázquez *et al*. 2016

	the morning of December 16, and 16 hours later, another episode of saturating harmonic tremor damaged some seismographs. All devices of monitoring: seismographs, tilt meters, gas detectors, etc. detect signals without precedent. Aerial photos taken on December 16 showed a lava dome with a volume exceeding all previous and growing 5 to 10 times faster than any of the previous ones. In these conditions, the Civil Protection authorities declared an increase in the level of alert and begin a preventive evacuation. Approximately 40,000 people to go out areas of risk. It is estimated that at that time the dome contained about 6~7x106 m3 of lava (Gómez-Vázquez et al. 2016). On December 18 the volcano erupted incandescent debris on its flanks about 5 or 6 kilometers from the crater. A similar eruption but lower-intensity followed on December 24, and the activity waned afterwards. Shortly after Christmas, the people returned to their communities.	
1996-1997	On 4 March 1996 a seismic crisis and ash emissions was related to the emplacement a large dome within the crater in March 25 1996 (Gómez-Vázquez et al. 2016). The growth of this dome, the trapped gases and the seismicity, were followed by a moderate explosion on April 30, 1996 partially destroyed the dome and ejected incandescent debris causing the death of 5 climbers near the lower rim of the crater. On June 30 1997 major explosion combined with a northwest wind, causes a light ash fall on Mexico City, shaking the public opinion (De la Cruz-Reyna et al. 2017). A small lahar reached some houses of the town of Santiago Xalitzintla in Puebla State.	Gómez-Vázquez *et al*. 2016 De la Cruz Reyna and Tilling 2017 Macías *et al*. 1995a.
1995	Gradually, the volcano reaches a state of equilibrium, with frequent exhalations similar to those described in the first stage of activity of the episode 1919-1925. This reduced activity permitted to increase the level of monitoring of the volcano. Geologists of the UNAM (Macías et al. 1995a) produced a first volcanic hazards map for the Popocatépetl, and later (Arana et al., 2016) issued a second version for same volcano, which describe the nature and extent of probable volcanic events. An early warning system is prepared to keep permanently informed the population of the condition that presents the volcano, which is called volcanic Alert Traffic Light (De la Cruz- Reyna 1995, 1996; De la Cruz-Reyna y Tilling 2008; De la Cruz-Reyna et al., 2017).	Arana *et al*. 2016. (De la Cruz-Reyna 1995, 1996; De la Cruz-Reyna and Tilling 2008; De la Cruz-Reyna *et al*. 2017).
1994	The onset of seismo-volcanic activity causes the development of the Plan Popocatépetl, involving state and federal authorities for Civil Protection and by scientists of the UNAM, the National Center for Disaster Prevention, technical advisory body of the National Civil Protection System of the Ministry of the Interior and other institutions, in order to develop contingency plans initially using the available volcanic maps of Robin and Boudal (Boudal C., Robin, C. 1989) as a basis for the risk assessments. This year it is also installed on the southwest flank of the volcano, about 4 kilometers from the crater, the telemetric station Chipiquixtle (PPX) by the National Center for Disaster Prevention (CENAPRED) and another seismic station telemetric: Colibrí (PPC), about 7 kilometers to the southeast of the crater (Quaas et al. 1995). At 01:31 (local time) on the morning of December 21 1994, a series of larger volcanic earthquakes mark the beginning of a new phase of activity at the volcano. At 01:54 hours (local time), a related to the opening of the volcanic conduit, ejected greater quantities of gas and ash. At dawn, ash falls on Puebla City and other nearby locations cause unrest among people. At 9:00 a.m. (local time) a Scientific Advisory Committee composed of experts from the National Autonomous University of Mexico (UNAM) and the CENAPRED has an emergency meeting requesting a reconnaissance flight; while both the ash emissions as in the seismicity kept on the rise (De la Cruz-Reyna and Tilling 2008; De la Cruz-Reyna et al. 2017). That afternoon and evening, the Response Programs and attention to the population: in Puebla State,	(Boudal C., Robin C. 1989). Quaas *et al*. 1995. (De la Cruz-Reyna and Tilling 2008; De la Cruz-Reyna *et al*. 2017)

was activated and 23 towns with an estimated 25,000 inhabitants were evacuated. A similar number of people auto-evacuated by their own means to homes of relatives and friends. In the State of Morelos 716 people from the village of Tetela del Volcán were evacuated. In the three following days several COSPEC flights showed high output of SO2. More seismic station and three telemetric electronic tilt meters were installed with the support of the United States of Geological Survey (USGS). Some of the evacuated populations gradually returned to their places of origin.

Appendix 2. Evacuation routes for the States of Mexico. Morelos, and Puebla.

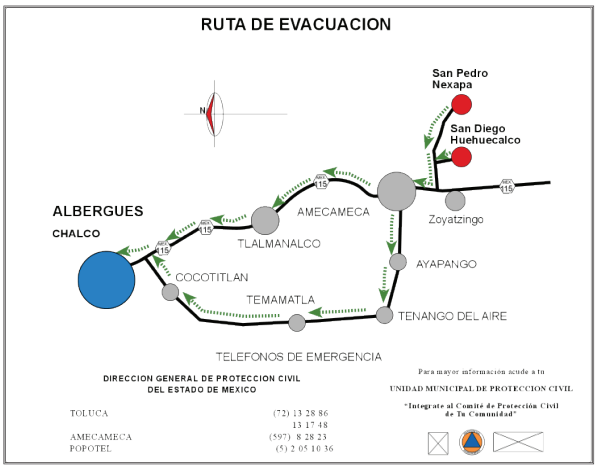

Figure 9. Evacuation routes for San Pedro Nexapa and San Diego Huehuecalco with high risk (red circles) in México State, which have a designated shelter (blue circle) at Chalco, State of México.

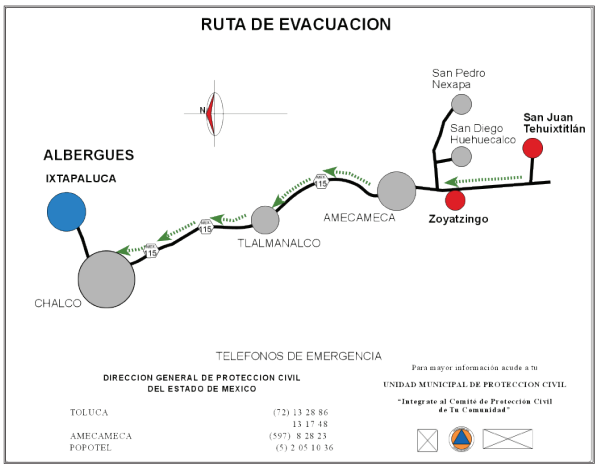

Figure 10. Evacuation routes for San Juan Tehuixtitlán and Zoyatzingo with high risk (red circles) in México State, which have a designated shelter (blue circle) at Ixtapaluca, State of México.

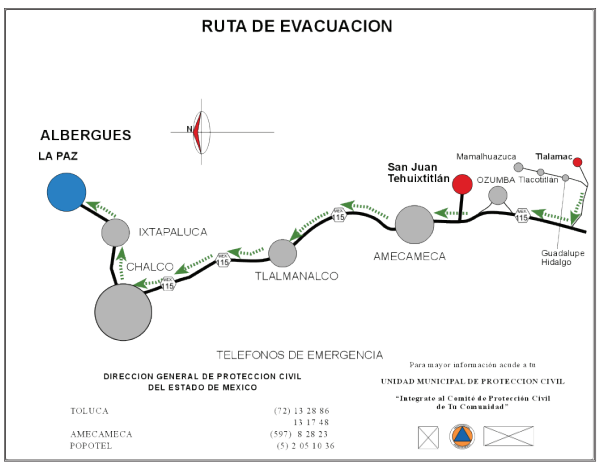

Figure 11. Evacuation routes for Tlalámac and San Juan Tehuixtitlán with high risk (red circles) in México State, which have a designated shelter (blue circle) at La Paz, State of México.

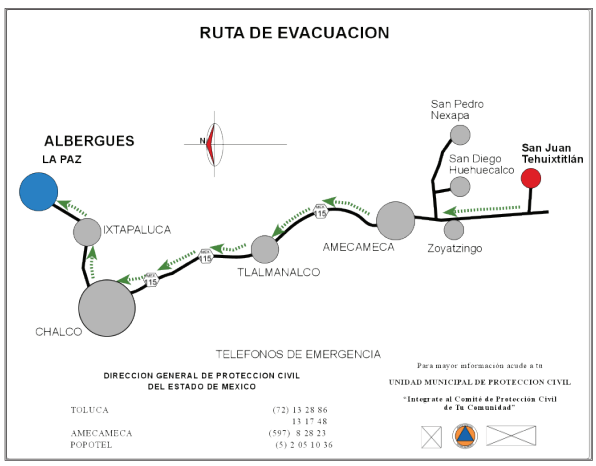

Figure 12. Evacuation route for San Juan Tehuixtitlán with high risk (red circle) in México State, which has a designated shelter (blue circle) at La Paz, State of México.

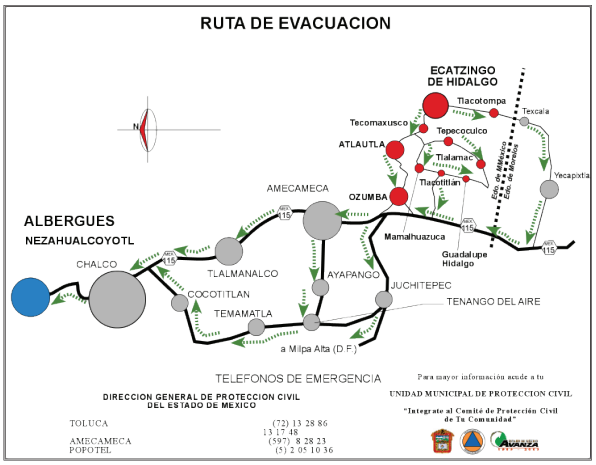

Figure 13. Evacuation routes for Ozumba, Atlautla, Tecomaxusco, Ecatzingo, Tlacotompa, Tepecoculco, Guadalupe Hidalgo, Tlalámac, Mamalhuazuca and Tlacotitlán with high risk (red circles) in México State, which have a designated shelter (blue circle) at Ciudad Nezahualcóyotl, State of México.

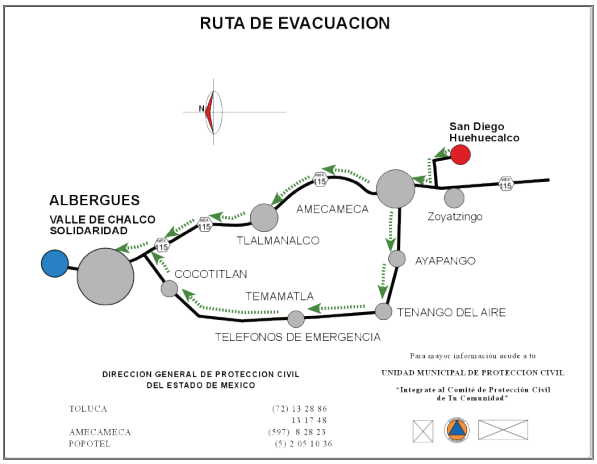

Figure 14. Evacuation route for San Diego Huehuecalco with high risk (red circle) in México State, which has a designated shelter (blue circle) at Valle de Chalco, State of México.

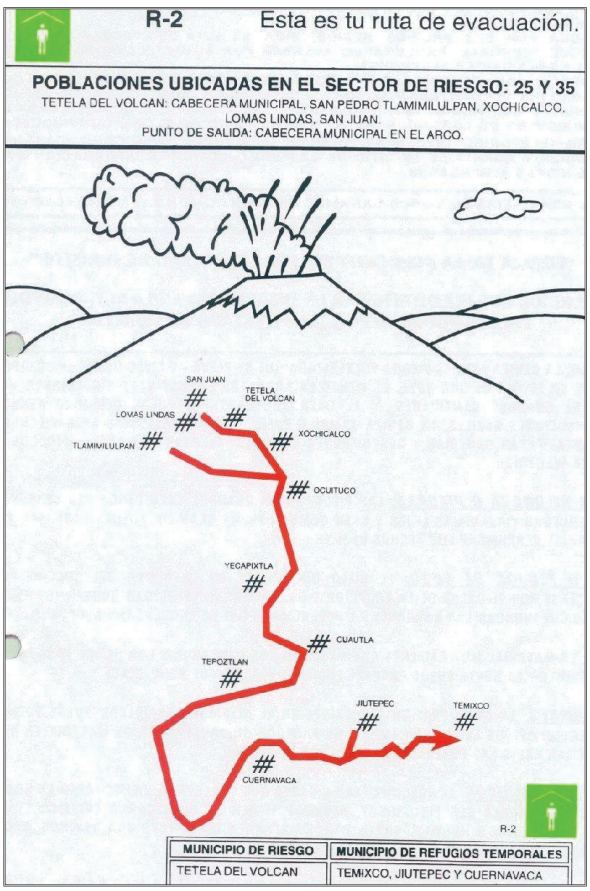

Figure 15. Evacuation route for San Pedro Tlalmimilulpan with high risk in Morelos State, which has designated shelters at Temixco, Jiutepec and Cuernavaca, Morelos.

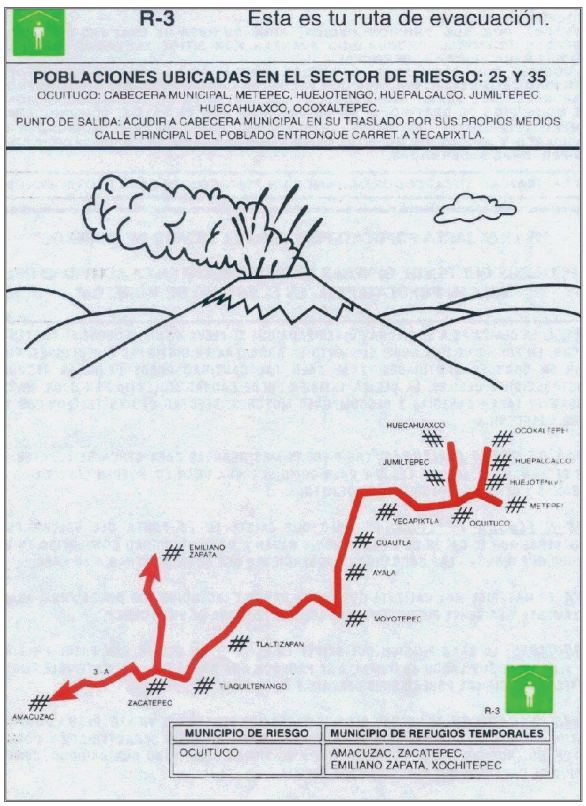

Figure 16. Evacuation route for San Francisco Ocoxaltepec with high risk in Morelos State, which has designated shelters at Amacuzac, Zacatepec, Emiliano Zapata and Xochitepec, Morelos.

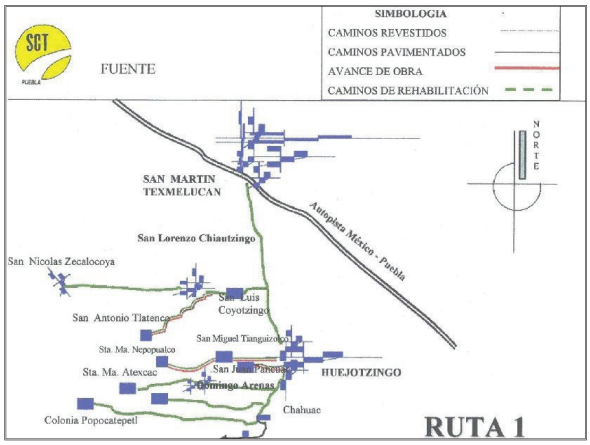

Figure 17. Evacuation routes for settlements with high risk in Puebla State, in which shelters are located at San Martin Texmelucan, Puebla.

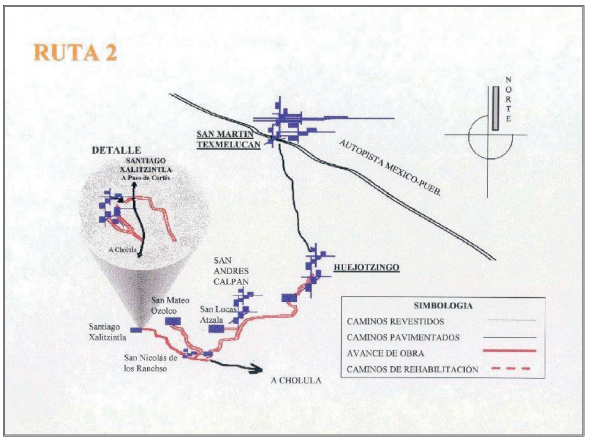

Figure 18. Evacuation routes for Santiago Xalitzintla, San Nicolás de los Ranchos and San Mateo Ozolco with high risk in Puebla State, in which shelters are located at San Pedro Cholula, Puebla.

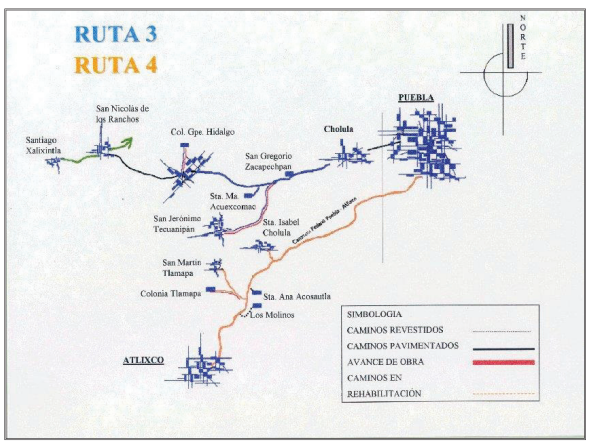

Figure 19. Evacuation routes for Santiago Xalitzintla and San Nicolás de los Ranchos with high risk in Puebla State, in which shelters are located at San Pedro Cholula, Puebla.

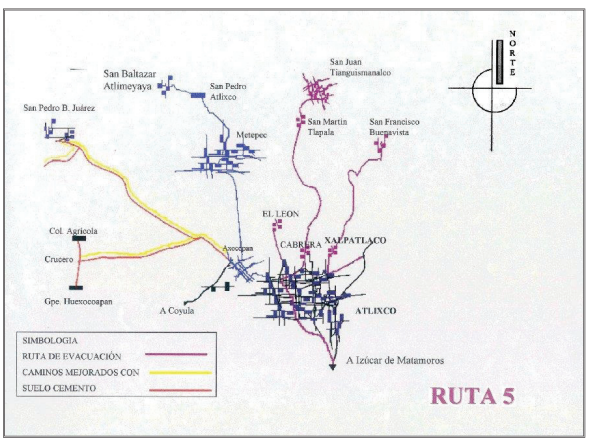

Figure 20. Evacuation routes for San Pedro Benito Juárez, Colonia Agricola and Guadalupe Hexocoapan with high risk in Puebla State, in which shelters are located at Izúcar de Matamoros, Puebla.

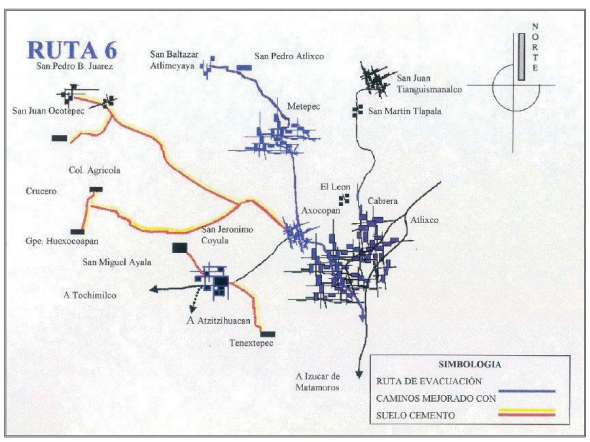

Figure 21. Evacuation routes for San Juan Ocotepec, Colonia Agricola and Guadalupe Hexocoapan with high risk in Puebla State, in which the shelter is located at Izúcar de Matamoros, Puebla.

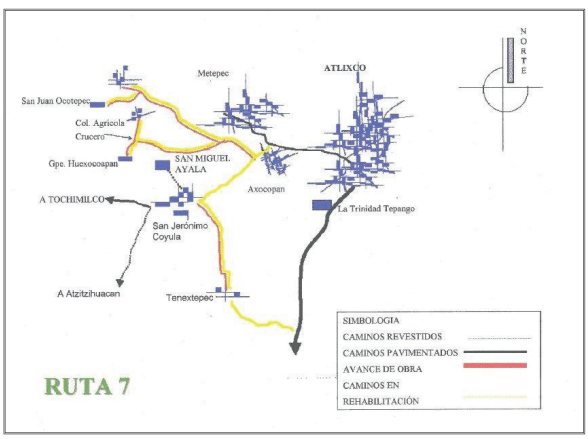

Figure 22. Evacuation routes for San Juan Ocote-pec, Colonia Agricola and Guadalupe Hexocoapan with high risk in Puebla State, in which shelters are located at Izúcar de Matamoros, Puebla.

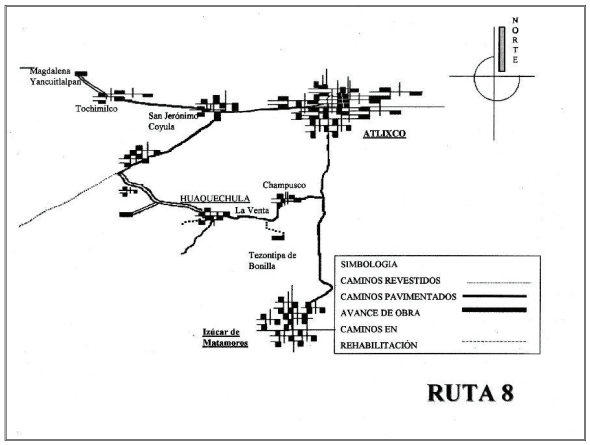

Figure 23. Evacuation routes for La Magdalena Yancuitlalpan, Tochimilco and San Jerónimo Coyula with high risk in Puebla State, in which shelters are located at Izúcar de Matamoros, Puebla.

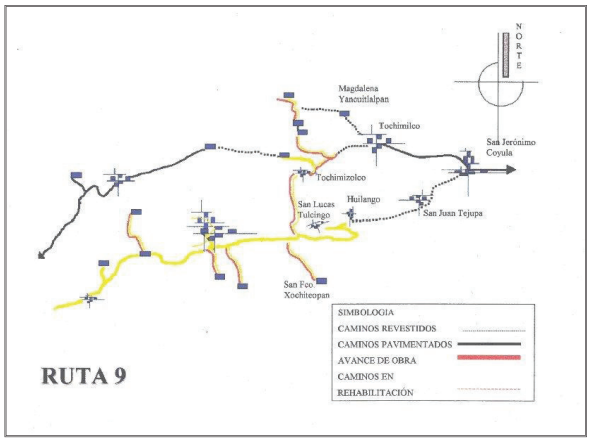

Figure 24. Evacuation route for Tochimizolco with high risk in Puebla State, in which the shelter is located at Tepexco, Puebla.

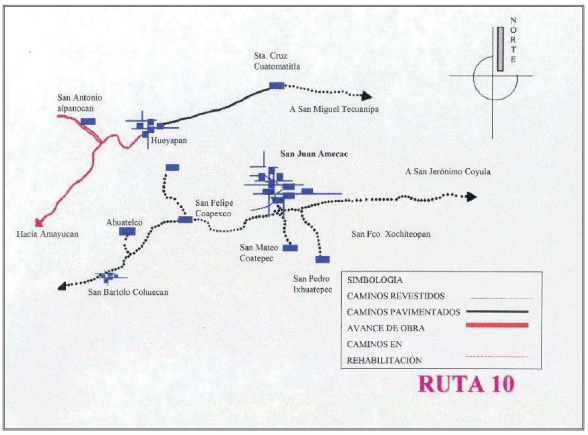

Figure 25. Evacuation routes for San Antonio Alpanocan, Santa Cruz Cuautomatitla and San Miguel Tecuanipan with high risk in Puebla State, in which shelters are located at Izúcar de Matamoros, Puebla.

Appendix 2. Tables containing times and distances from each village (origin) to temporary shelter respective (destination).

Table 7. Times and distances from San Pedro Nexapa to temporary shelters at Chalco, State of México (See Fig. 26).

San Pedro Nexapa (origin)		Chalco (destination)
VILLAGE	CUMULATIVE TIME (MINUTES)	CUMULATIVE DISTANCE (KM)
San Pedro Nexapa	0	0
Amecameca	11	8
Tlalmanalco	31	18
Cocotitlán	41	26
Chalco (temporary shelters 10, 11, 12, 13 and 14).	50	34

Note: Maximum time and distance are up to the temporary shelter 11 of San Marcos Huixtoco.

Table 8. Times and distances from San Diego Huehuecalco to temporary shelters at Chalco, State of México (See Fig. 27).

San Diego Huehuecalco (origin)		Chalco (destination).
VILLAGE	CUMULATIVE TIME (MINUTES)	CUMULATIVE DISTANCE (KM)
San Diego Huehuecalco	0	0
Amecameca	9	5
Ayapango	18	10
Tenango del Aire	31	18
Temamatla	43	23
Cocotitlán	52	28
Chalco (temporary shelters 1, 2, 3, 4, 8, 9, 15 and 16).	67	36

Note: Maximum time and distance are up to the temporary shelter 1 of Chalco.

Table 9. Times and distances from San Juan Grande to temporary shelters at Chalco, State of México (See Fig. 28).

San Juan Grande (origin)		Chalco (destination)
VILLAGE	CUMULATIVE TIME (MINUTES)	CUMULATIVE DISTANCE (KM)
San Juan Grande	0	0
San Pedro Nexapa	5	2
Amecameca	16	10
Ayapango	24	15
Tenango del Aire	37	23
Temamatla	49	28
Cocotitlán	58	33
Chalco (temporary shelters 5 and 6).	71	39

Note: Maximum time and distance are up to the temporary shelter 5 of Chalco.

Table 10. Times and distances from San Marcos Tecomaxusco to temporary shelter at Chalco, State of México (See Fig. 29).

San Marcos Tecomaxusco (origin)		Chalco (destination).
VILLAGE	CUMULATIVE TIME (MINUTES)	CUMULATIVE DISTANCE (KM)
San Marcos Tecomaxusco	0	0
Atlautla	19	8
Popo Park	24	11
Zoyatzingo	30	15
Amecameca	36	20
Ayapango	44	25
Tenango del Aire	57	33
Temamatla	69	38
Cocotitlán	78	43
Chalco (temporary shelter 7).	91	49

Note: Maximum time and distance are up to the temporary shelter 7 of Chalco.

Table 11. Times and distances from Ocoxaltepec to temporary shelters at Jiutepec, Morelos (See Fig. 30).

Ocoxaltepec (origin)		Jiutepec, Mor. (destination).
VILLAGE	CUMULATIVE TIME (MINUTES)	CUMULATIVE DISTANCE (KM)
Ocoxaltepec	0	0
Tlalmimilulpan	8	3
Huepalcalco	16	6
Huejotengo	22	7
Ocuituco	32	11
Yecapixtla	50	21
Cuautla	71	35
Cocoyoc	84	41
Yautepec	103	52
Jiutepec (temporary shelters: no. 34, Esc. Primaria Emilio Rivapalacio Morales; 35, Esc. Primaria Jaime Torres Bodet; 36, Esc. Primaria Benito Juárez; 37, Esc. Primaria Mariano Matamoros; 38, Jardín de Niños Tolteca; 39, Jardín de Niños Tepehuanes; 40, Jardín de Niños Miguel Ángel Buonarroti; y 41, Jardín de Niños Cometa Halley).	148	72

Note: Maximum time and distance are up to the temporary shelter 34, Esc. Prim. Emilio Rivapalacio Morales at Jiutepec, Mor.

Table 12. Times and distances from Tlalmimilulpan to temporary shelters at Cuernavaca, Morelos (See Fig. 31).

Tlalmimilulpan (origin)		Cuernavaca, Mor. (destination).
VILLAGE	CUMULATIVE TIME (MINUTES)	CUMULATIVE DISTANCE (KM)
Tlalmimilulpan	0	0
Huepalcalco	8	3
Huejotengo	14	4
Ocuituco	24	8
Yecapixtla	42	18
Cuautla	60	30
Oaxtepec	74	37
Tepoztlán	105	55
Cuernavaca (temporary shelters: no. 24, Esc. Primaria Plan de Ayala; 22, Esc. Primaria Fray Bartolomé de las Casas; 23, Esc. Primaria Niños Héroes de 1847 y 25, Esc. Primaria Carmen Serdán).		

Note: Maximum time and distance are up to the temporary shelter 24, Esc. Prim. Plan de Ayala at Cuernavaca, Mor.

Table 13. Times and distances from San Mateo Ozolco to temporary shelter at San Pedro Cholula, Puebla (See Fig. 32).

San Mateo Ozolco (origin)		San Pedro Cholula (destination).
VILLAGE	CUMULATIVE TIME (MINUTES)	CUMULATIVE DISTANCE (KM)
San Mateo Ozolco	0	0
San Pedro Yancuitlalpan	7	4
San Andrés Calpan	16	9
San Pedro Cholula (temporary shelter 10, Ex Módulo Ferial).	45	26

Table 14. Times and distances from Santiago Xalitzintla to temporary shelter at San Pedro Cholula, Puebla (See Fig. 33).

Santiago Xalitzintla (origin)		San Pedro Cholula (destination).
Village	CUMULATIVE TIME (MINUTES)	CUMULATIVE DISTANCE (KM)
Santiago Xalitzintla	0	0
San Nicolás de los Ranchos	7	4
San Pedro Yancuitlalpan	11	5
San Andrés Calpan	20	10
San Pedro Cholula (temporary shelter 10, Ex Módulo Ferial).	49	27

Table 15. Times and distances from San Nicolás de los Ranchos to temporary shelter at San Pedro Cholula, Puebla (See Fig. 34).

San Nicolás de los Ranchos (origin)		San Pedro Cholula (destination).
VILLAGE	CUMULATIVE TIME (MINUTES)	CUMULATIVE DISTANCE (KM)
San Nicolás de los Ranchos	0	0
San Pedro Yancuitlalpan	4	1
San Andrés Calpan	13	6
San Pedro Cholula (temporary shelter 9, Recinto Ferial).	42	25

Table 16. Times and distances from San Pedro Benito Juárez to temporary shelter at Izúcar de Matamoros, Puebla (See Fig. 35).

San Pedro Benito Juárez (origin)		Izúcar de Matamoros (destination).
VILLAGE	CUMULATIVE TIME (MINUTES)	CUMULATIVE DISTANCE (KM)
San Pedro Benito Juárez	0	0
Lomas de Axocopan	24	11
La Magdalena Axocopan	28	12
San Jerónimo Coyula	34	16
San Juan Los Laureles	47	22
La Trinidad Tepango	53	26
Tepeojuma	75	41
Izúcar de Matamoros (temporary shelter 33, Centro Escolar Lázaro Cárdenas).	98	57

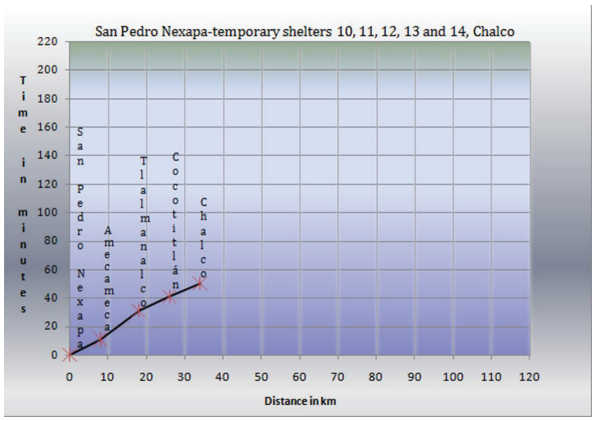

Figure 26. Time and distance diagram among San Pedro Nexapa and their temporary shelters 10, 11, 12 and 13 at Chalco, State of México.

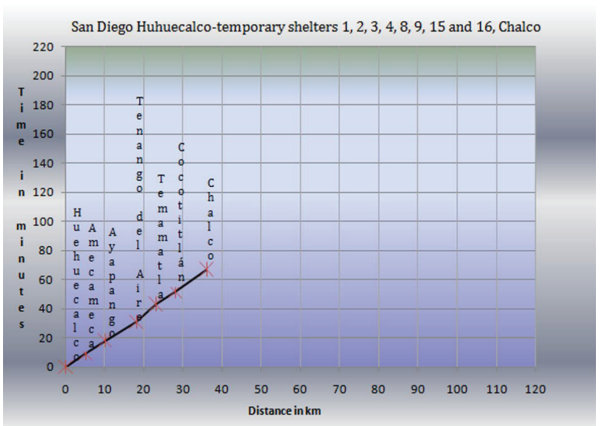

Figure 27. Time and distance diagram among San Diego Huehuecalco and their temporary shelters 1, 2, 3, 4, 8, 9, 15 and 16 at Chalco, State of México.

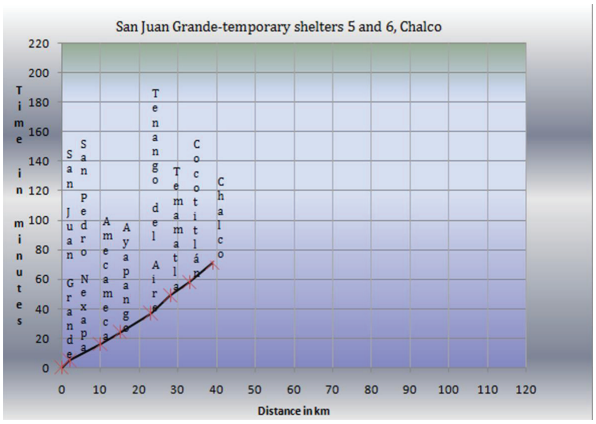

Figure 28. Time and distance diagram among San Juan Grande and their temporary shelters 5 and 6 at Chalco, State of México.

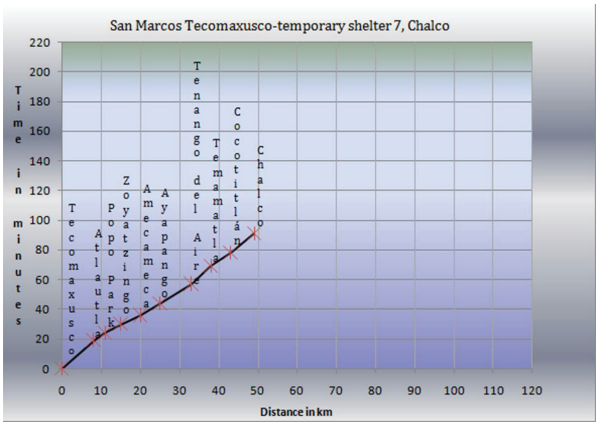

Figure 29. Time and distance diagram among San Marcos Tecomaxusco and its temporary shelter 7 at Chalco, State of México.

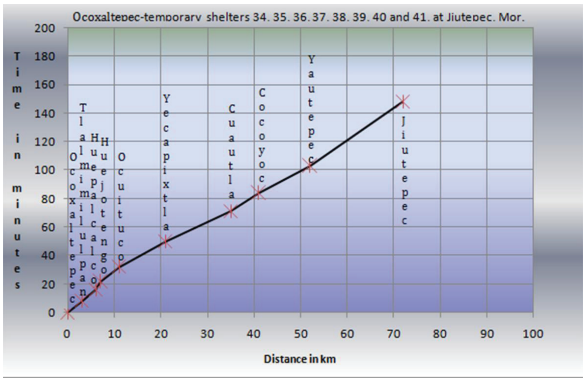

Figure 30. Time and distance diagram among San Francisco Ocoxaltepec and their temporary shelters 34, 35, 36, 37, 38, 39, 40 and 41 at Jiutepec, Morelos.

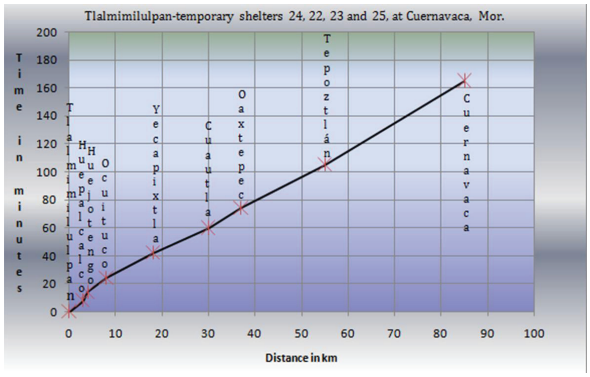

Figure 31. Time and distance diagram among San Pedro Tlalmimilulpan and their temporary shelters 22, 23, 24 and 25 at Cuernavaca, Morelos.

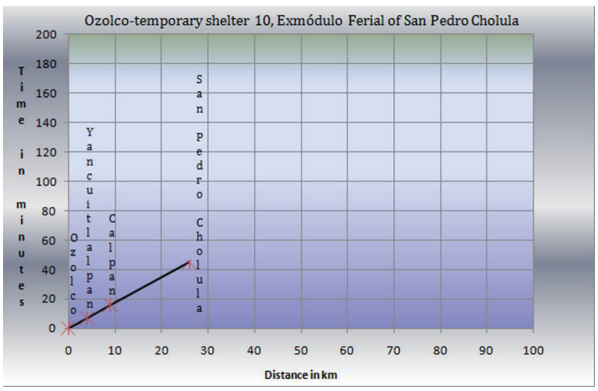

Figure 32. Time and distance diagram among San Mateo Ozolco and its temporary shelter 10 at Ex módulo Ferial of San Pedro Cholula, Puebla.

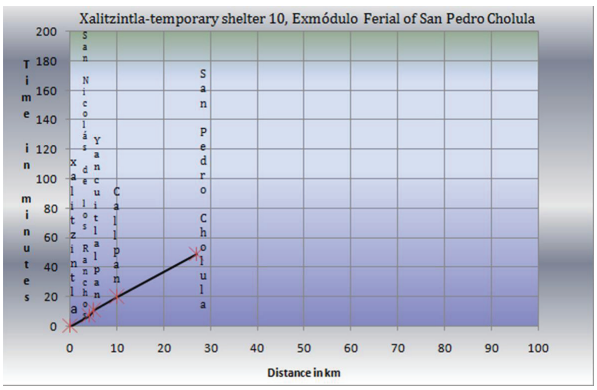

Figure 33. Time and distance diagram among Santiago Xalitzintla and its temporary shelter 10 at Ex módulo Ferial of San Pedro Cholula, Puebla.

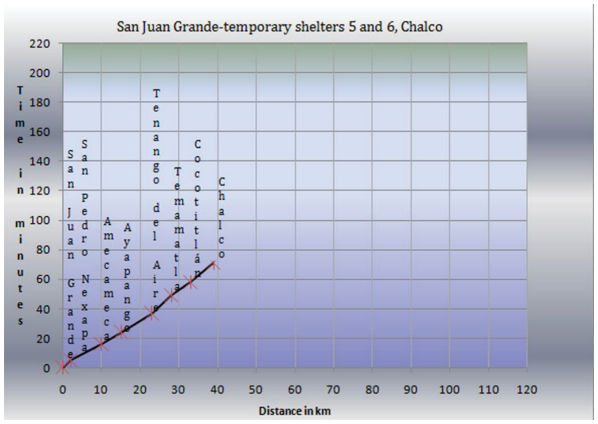

Figure 34. Time and distance diagram among San Nicolás de los Ranchos and its temporary shelter 9 at Recinto Ferial of San Pedro Cholula, Puebla.

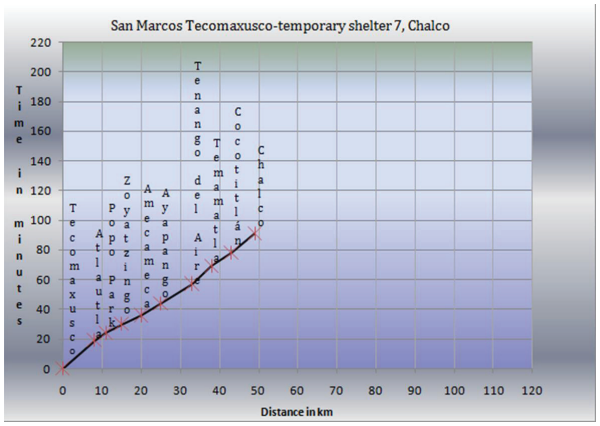

Figure 35. Time and distance diagram among San Pedro Benito Juárez and its temporary shelter 33 at Centro Escolar Lázaro Cárdenas of Izúcar de Matamoros, Puebla.

Geofísica Internacional (2019) 58-1: 33-48

Original paper

Hazard assessment of the ongoing lava dome eruption at Popocatépetl volcano from the statistical analysis of significant explosive events in the period of 1997 to 2016.

Ana Teresa Mendoza-Rosas* and Servando De la Cruz-Reyna

Received: January 04, 2018; accepted: June 25, 2018; published on line: January 18, 2019

Resumen

El volcán Popocatépetl inició un episodio eruptivo en 1994 después de un periodo de 70 años de quietud. Este episodio, que persiste hasta el momento, se caracteriza por una secuencia de episodios sucesivos de emplazamiento y destrucción de domos de lava. Esta actividad va acompañada por la producción de columnas eruptivas de ceniza que alcanzan alturas considerables, tanto en las etapas de formación como de destrucción de los domos. Debido a que la altura de la columna es un indicador de la tasa de liberación de energía de cada evento y de su poder de dispersión y potencial destructivo, utilizamos ese parámetro como indicador del peligro asociado a esa actividad. Por lo tanto, hemos construido una base de datos de las columnas producidas por explosiones significativas que han superado la altura de 4 km sobre la cumbre del volcán en el período de 1997 a 2016. Considerando la ocurrencia de las columnas como una variable aleatoria que representa el peligro de dicha actividad explosiva, analizamos las características estadísticas de esa base de datos. Encontramos que se puede describir la ocurrencia de explosiones significativas como un proceso puntual que se desarrolla en al menos dos etapas, con un punto de cambio significativo en 2003. La primera etapa 1997-2003 tiene un marcado carácter no-estacionario, y se describe bien con una distribución de Mezcla de Exponenciales (MOED), mientras que la segunda, de 2003 a 2016 se comporta de forma estacionaria y se ajusta satisfactoriamente a una distribución exponencial. Esta característica produce diferencias importantes en los resultados de evaluación del peligro de ocurrencia de columnas eruptivas significativas, por lo que es importante analizar continuamente las características estadísticas del proceso para identificar posibles cambios en la dependencia temporal del proceso, que por lo general no van acompañados de manifestaciones físicas evidentes.

Palabras clave: volcán Popocatépetl, erupción de domos de lava, explosiones vulcanianas, columnas eruptivas, emisión de cenizas, exhalaciones, análisis estadístico.

A. T. Mendoza-Rosas*
CONACYT
Centro de Ingeniería y Desarrollo Industrial
Av. Playa Pie de la Cuesta 702
Desarrollo San Pablo CP 76125
Querétaro, Qro, México
*Corresponding author: ana.mendoza@cidesi.edu.mx

S. De la Cruz-Reyna
Instituto de Geofísica
Universidad Nacional Autónoma de México
C. Universitaria CDMX, 04510
México

Abstract

After 70 years of quiescence Popocatépetl volcano began a new episode of activity in 1994, which is still ongoing. The predominant activity has been a succession of dome emplacements followed by sequences of dome-destruction explosions producing prominent volcanic ash columns. Moreover, relatively large eruptive columns have also been produced during the dome growth stages. To assess the hazard of this activity we use the height of the columns as an indicator of the rate of energy release of the events and of their dispersive power and destructive potential. We hence built a database of the events producing columns exceeding heights of 4 km above the volcano summit for the period 1997 to 2016. Considering the occurrences of such columns as a random variable representing the hazard of such explosive activity, we studied the statistical features of the database, and found that the occurrence rate of significant explosions is a point process developing in at least two stages, with the significant change-point in 2003. The first stage from 1997 to 2003 is non stationary, while the second one, from 2003 to 2016, shows a stationary behavior. While the former is well described by a Mixture of Exponentials distribution (MOED), the latter fits well an Exponential distribution. The probabilities of significant eruptive columns occurring in given time intervals result to be strongly dependent on the stationarity of the process. The assessment of hazard thus requires a continuous testing of the time dependence of the ongoing process, since there is no clear physical evidence of the factors controlling this behavior.

Key words: Popocatépetl volcano, lava dome eruption, vulcanian explosions, eruptive columns, ash emission, exhalations, statistical analysis.

Introduction

After nearly 70 years of dormancy, Popocatépetl volcano reawakened on December 21 1994 with an activity predominantly consisting of dacitic lava dome-forming episodes and their subsequent destruction by vulcanian explosions. This lava dome eruption is still ongoing and there is no certainty on the way in which it may evolve in the future.

The assessment of the hazard related to such activity at the light of the available information may help to reduce the vulnerability through the preparation and set up of a series of specifically designed measures (such as mitigation and evacuation plans) for the most probable eruption scenario (De la Cruz-Reyna and Tilling 2008).

However, assessing hazard is a complex task requiring a broad understanding of the patterns of occurrence of the different volcanic manifestations. In the ongoing eruption, the intensity of the eruptive activity has been limited to moderately large explosions and exhalations (protracted explosions with extended gas output) producing significantly high eruptive columns with substantial dispersion of ash and volcanic gases into the atmosphere. Such events are not necessarily related to dome destruction explosions, as they often occur during dome growth episodes. In addition to the wind parameters, the dispersion forecasts are strongly dependent on the source term, which describes both the intensity rate of volcanic emissions and their initial vertical distribution in the atmosphere, both controlling the height of the columns.

Here, we address this problem considering volcanic hazard as a measure of the probability that a threatening volcanic event occurs in a specific time interval, and defines, along with the exposure and the vulnerabilities to that manifestation, the volcanic risk. To calculate the volcanic hazard we analyze the statistics of the volcanic manifestations that may have some degree of damaging potential in the current state of Popocatépetl´s activity, this is the explosive events generating eruptive columns exceeding 4 km above the volcano summit henceforth referred to as "significant explosions" or "SE". The data were obtained from the daily activity reports of CENAPRED (Centro Nacional de Prevención de Desastres). Among other volcano surveillance devices, CENAPRED maintains a seismic monitoring network and an array of three video cameras surrounding the volcano, transmitting in real time to its monitoring center. The images are included in the website of CENAPRED with photos updated every 60 sec. The surveillance monitors at CENAPRED have graphic scales allowing, weather permitting, quick estimates of the column heights, which are included in the daily reports.

Popocatépetl volcano

Popocatépetl volcano, rising 5454 m.a.s.l and with an 800 x 600 m wide crater is considered one of the high-risk active volcanoes in North America. This quaternary volcano is located in the Trans-Mexican Volcanic Belt, about 70 km southeast of México City and 40 km from the city of Puebla, with more than 80,000 people living in a high-risk area, and nearly one million

in intermediate-risk areas (Ramos-Jiménez, 2017, this issue). Over 20 million living within a radius of 100 km around the volcano may be exposed to ash falls associated with a major eruption (De la Cruz-Reyna and Tilling 2008, De la Cruz-Reyna *et al*., 2017). At least three previous major cones have been destroyed by gravitational failure during the Pleistocene producing massive debris-avalanche deposits covering broad areas to the south (Robin and Boudal 1987; Boudal and Robin 1989; Siebe *et al*., 1995; Siebe *et al*., 1997; De la Cruz-Reyna and Siebe 1997; Sosa-Ceballos *et al*., 2012). The volcano eruptive history includes a wide spectrum of eruption styles, including 9 plinian events in the last 23,000 years (Siebe *et al*., 1996; Siebe and Macías 2006; Mendoza-Rosas and De la Cruz-Reyna 2008, Siebe *et al*., 2017) and about 19 eruptions with VEI (Volcanic Explosivity Index, Newhall and Self, 1982) in the range 2 ~ 3 in the last 500 years (De la Cruz-Reyna and Tilling 2008; Mendoza-Rosas and De la Cruz-Reyna 2008; 2009).

Since Popocatépetl volcano reawakened on December of 1994, it has been the focus of volcanologists attention due to its peculiarities, such as a very high passive gas output (Delgado-Granados, *et al*., 2001; Grutter *et al*., 2008), and the lengthy lava dome eruption episode so far lasting more than 20 years (De la Cruz-Reyna *et al*., 2017). In this period, at least 40 distinct lava domes have been emplaced in the crater of Popocatépetl. Gómez-Vázquez *et al*. (2016) and Mendoza-Rosas *et al*. (2017) analyzed this process and found that the activity has developed as a succession of five high- and low-rate regimes of emplacements and lava production rates, and that the volumes and thicknesses of the emplaced domes are scaled by exponential distributions. However, as discussed below, the succession of SE shows a different pattern of occurrence to that of the dome emplacements, and we therefore analyze it as a separate process.

Eruptive column height database

In this paper we analyze the eruptive activity that has generated columns with heights ≥4 km above the volcano summit (SE) for the period 1997 – 2016 using the eruptive column data from CENAPRED

(http://www.cenapred.gob.mx/reportesVolcan/BuscarReportesVolcan?optBusqueda=1), and from Martin-Del Pozzo *et al*. (2008), and Martin-Del Pozzo (2012). That period was chosen to ensure the reliability and completeness of the record, since the column height-calibrated video monitoring system of CENAPRED has been fully operative since 1997 and most of the columns higher than 4 km above the volcano summit could be seen above the cloud layer unlike smaller columns.

We counted 64 SE events producing column heights reaching or exceeding 4 km over the Popocatépetl summit from June 1997 to November 2016 (Figure 1). The highest columns exceeding 7 km above the volcano summit (about 13 km above sea level) occurred on 30 Jun 1997, 29 Nov 1998 and 22 Jan 2001 (local times).

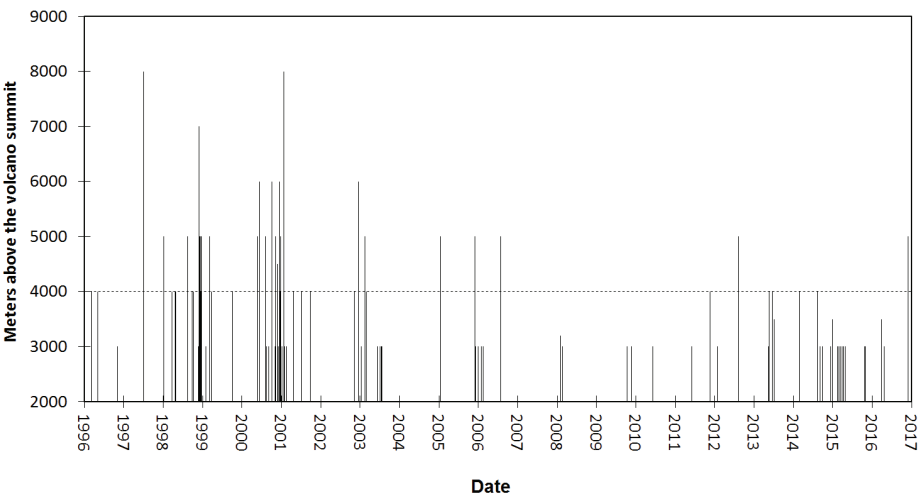

Figure 1. Plot of 138 eruptive events producing columns exceeding 3000 m above the volcano summit since 1996. Data from CENAPRED (website), Martin-Del Pozzo et al. (2008) and Martin-Del Pozzo (2012). About 47% of these emissions reached or exceeded 4 km above the summit (dashed line level). Although the 3 km exceedance series may be incomplete, as smaller columns are frequently hidden by meteorological clouds, the 4 km of higher series (SE) is probably complete. The volcano is 5454 m high.

Figure 2 shows the cumulative number of SE events. The grey and white areas in the figure mark the five high and low regimes of dome emplacement and long-term magma production rates described in Gómez-Vazquez *et al*. (2016) and Mendoza-Rosas *et al*. (2017). Inspection of the figure reveals an irregular stepwise behavior of the higher eruptive column occurrences, with high rates and drastic slope changes around 1998, 2000-2001, 2003 (marked with red vertical lines). These changes occur near, but not coincident with, the first three regime transitions of the dome emplacement rates.

The transitions between dome emplacement rates marked as regimes IV and V in Gómez-Vázquez *et al*. (2016) and Mendoza-Rosas *et al*. (2017) are not reflected in the cumulative number of major eruptive columns, and only a significant reduction of the rate of events is observed after July 2003 (Álvarez-Ramírez *et al*., 2009). This indicates that the processes controlling the larger explosions involves additional factors than those controlling the lava dome emplacements, and may thus have a different statistical behavior.

Features of the significant explosion sequence

We first test the whole data of eruptive columns ≥ 4 km above the summit for independence and stationarity. To test for independence we calculated the autocorrelation function (ACF) of the time intervals between successive eruptive column occurrences. Figure 3 shows that there is no significant correlation between one time interval and the next (one-lag serial correlation is only 0.204). However, at some larger lags, the ACF exceeds the 5% Kolmogorov-Smirnov (K-S) significance level (0.244) needed to reject independence, suggesting some long-term effects as in Lag 3 and 7 with 0.27 and 0.26 correlation values respectively may reveal some shrouded dependence effects.

We then tested the stationarity of the sequence performing a 3-points moving average test (Klein 1982; De la Cruz-Reyna 1996; Mendoza-Rosas and De la Cruz–Reyna 2008; 2009; 2010). Figure 4 shows the results of the test for the highest eruptive columns sequence. The circles represent averages of three consecutive repose interval (time between major explosions) plotted at the date of explosion ending with the third repose interval marked as a filled circle (Klein, 1982; De la Cruz-Reyna, 1996). The solid horizontal line is the mean of all the repose times; the thin dotted line represents the 95% upper confidence level, and the thick dashed line represents the 90% upper confidence level. In figure 4 four open circles and one filled circle fall well above both confidence levels revealing the non-stationarity of the process mostly caused by the significantly different eruptive activity rates before and after 2003.

As a further test of the whole period 1997-2016 under an intrinsic hypothesis of weak stationarity, we computed a variogram for multiples of the spacing between the events. The variogram method is commonly applied to spatial geo-statistical analyses as it readily

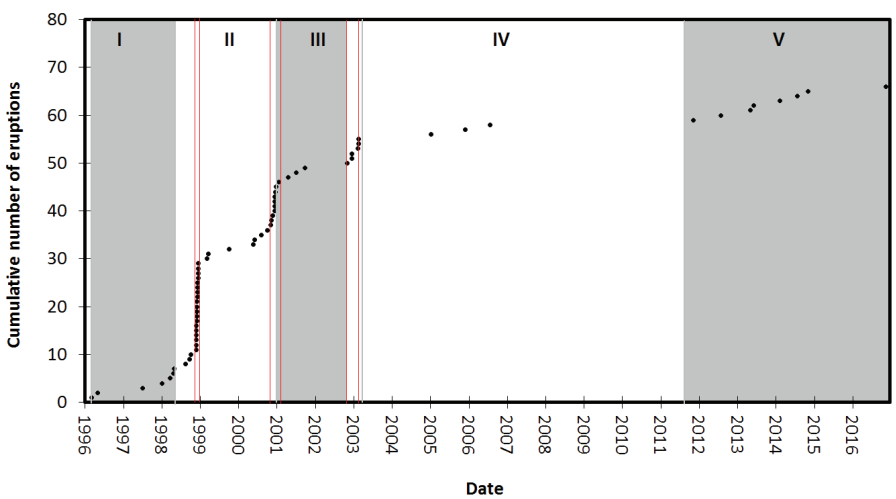

Figure 2. Cumulative number of SE at Popocatépetl volcano producing columns of 4 km or more above the volcano summit. The red lines mark the evident transitions between occurrence rates of those explosions. The gray (high rate) and white (low rate) areas (Roman numerals) represent the alternated regimes of lava dome emplacements and mean lava extrusion rates described in Gómez-Vázquez *et al*. (2016) and Mendoza-Rosas *et al*. (2017).

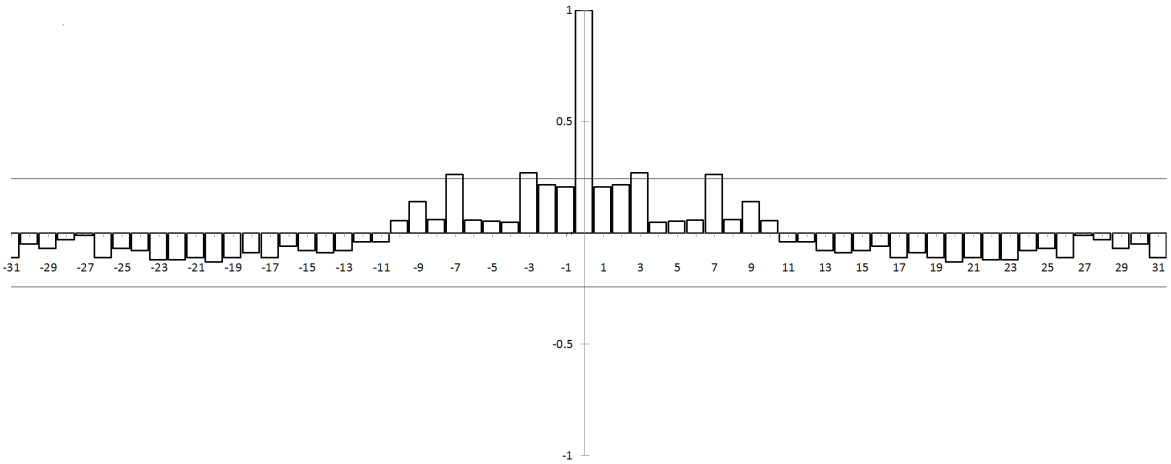

Figure 3. Autocorrelation function of the successive time intervals between eruptive events with eruptive columns ≥ 4 km above the summit from 1997 to 2016. The horizontal thin solid lines represent the 5% significance level Kolmogorov - Smirnov values needed to reject independence.

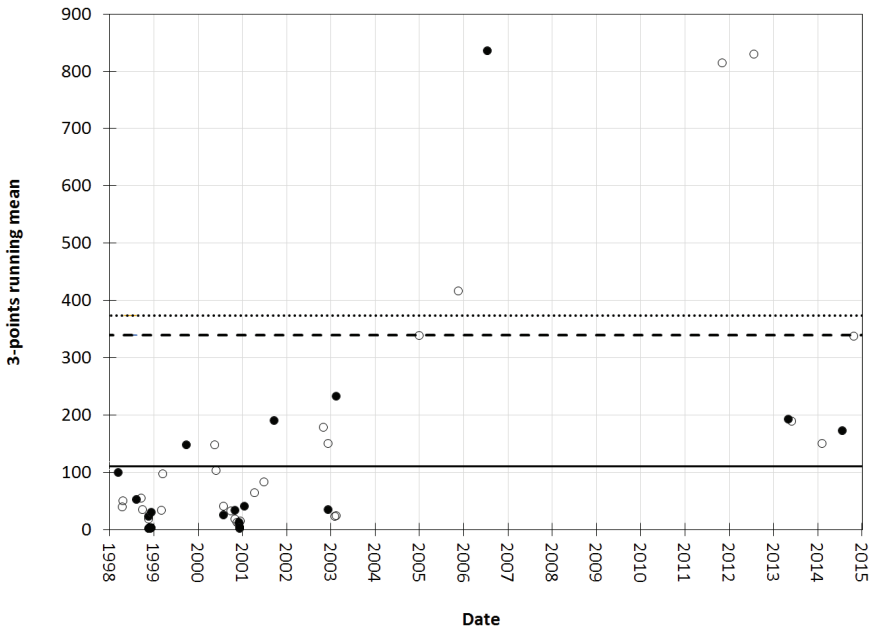

Figure 4. Moving average of three-consecutive reposes of eruptive activity with column heights ≥4km, both in period from 1997 to last eruptive activity in 2016. The solid horizontal line is the mean of all the time periods between events. The dotted line represents the 95% upper confidence level, and the dashed line represents the 90% upper confidence level calculated with the chi-square and the binomial distribution (De la Cruz-Reyna, 1996)

identifies the homogeneity of the increments in the studied stochastic process (Cox and Miller, 1965, Jaquet and Carniel 2001, 2006; Jaquet *et al*., 2006). In the present case, we obtained an unbounded variogram confirming the non-stationary character of the whole SE sequence. We conclude that the process is non-stationary with a significant change in the occurrence rate around year 2003.

The time-dependence of the process presents an interesting feature. Inspection of Figure 4 reveals that points of the moving average tend to cluster near the horizontal axis (indicating short mean repose times and thus higher rates of SE near the time at which the largest explosions were recorded). This suggests that the rate at which the volcano releases thermal energy (closely related to the eruptive column height) is partitioned between a higher rate

of explosions and an increase in the power of explosions. This issue and its consequences on the hazard assessment are addressed in the discussion and conclusions section.

Statistical analysis

To deal with the relatively high autocorrelation values at lags 3 and 7 (Figure 3), and to fulfill a condition of independence, we perform the statistical analysis separately for two different periods: From Jun 30, 1997 to February, 2003, and from February 2003 to December, 2016. 2003 is the year when significant changes in the rate of dome emplacements and in the rate of significant explosions were reported (Álvarez-Ramirez *et al*., 2009; Gómez-Vázquez *et al*., 2016; Mendoza-Rosas *et al*., 2017). The moving mean analysis (Figure 4) also shows significant changes in those periods. Figures 5 and 6 show the autocorrelation function and the stationarity tests respectively for each of the periods.

Figures 5 a and b respectively show that the time intervals between significant eruptive column occurrences in the periods 1997 to 2003 and 2003-2016 are uncorrelated and thus independent, as in each case the ACF does not exceed the K-S 5 % level of significance. However, the stationarity tests in Figure 6 show that while the period 2003-2016 is a stationary process, this is not the case for the period 1997-2003, in which several points are well above the confidence levels. We thus proceed to analyze these periods separately, but not without underscoring that the gradual clustering of points near the horizontal axis reveals that the effect of "surges" of higher rates of more powerful explosions occurs in both periods. This suggests that the moving average analysis could be a helpful, simple to use tool to recognize a condition of increased probability of powerful explosions at Popocatépetl, particularly when the amount of data are insufficient for a valid variogram or to perform another type of analysis.

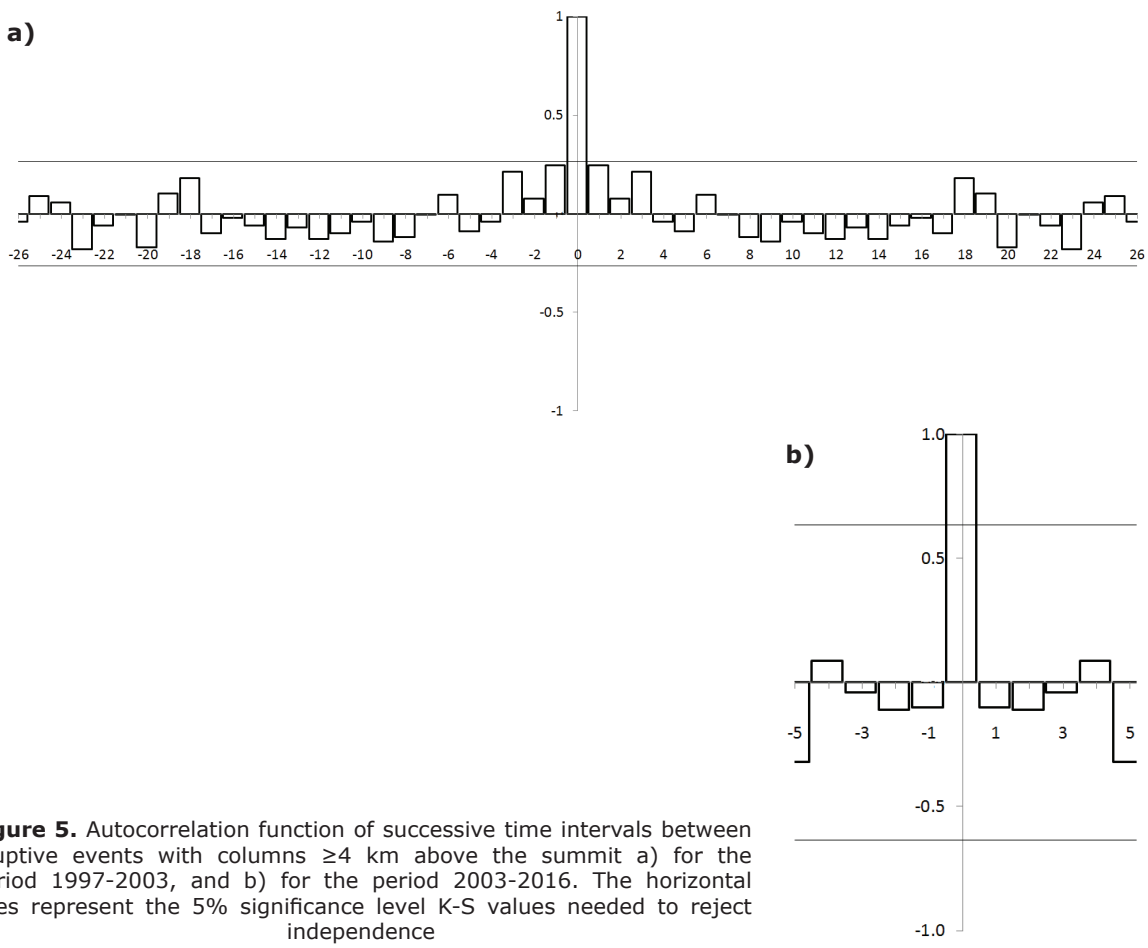

Figure 5. Autocorrelation function of successive time intervals between eruptive events with columns ≥4 km above the summit a) for the period 1997-2003, and b) for the period 2003-2016. The horizontal lines represent the 5% significance level K-S values needed to reject independence

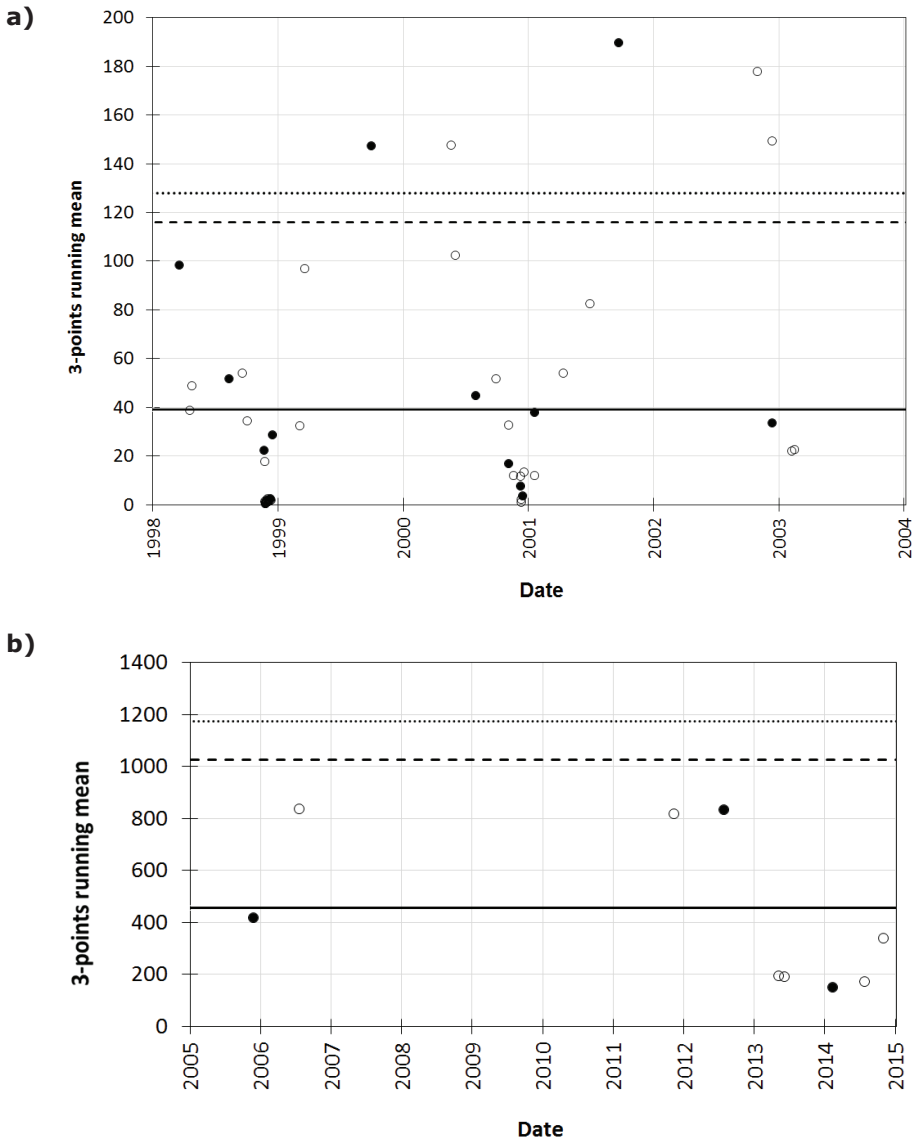

Figure 6. a) Moving averages of three consecutive reposes of eruptive activity with eruptive columns ≥ 4 km above the summit from 1997 to February, 2003, b) the same for the period 2003-2016. Horizontal lines as in Figure 4.

Probabilities of eruptive columns ≥4km above the volcano summit

To assess the hazard, and considering that we have to analyze and compare the results between the stationary and non-stationary periods of time with different characteristics of independence described in the previous section, we obtained occurrence probabilities of events with eruptive columns ≥ 4 km above the summit for the specific time intervals: from 1997 to 2003 and from 2003 to 2016. We tested different probability distributions for the periods: the mixture of exponentials distribution (MOED), the exponential distribution, describing the waiting times between events of a Poisson process, and the Weibull distribution (Mendoza-Rosas and De la Cruz-Reyna 2008; 2009; 2010; Mendoza-Rosas *et al*. 2017; De la Cruz-Reyna 1991; 1993; 1996; Bebbington 2007; Bebbington and Lai 1996).

The exponential distribution is frequently used in life-testing statistical analysis of events occurring at random in time but in a stationary and memoryless fashion. A random variable *X* has an exponential distribution if it has a probability density function of the form

$$f_X(x) = \lambda e^{-(x-\theta)\lambda}, \quad x > \theta; \lambda > 0$$

If $\theta = 0$ and $\lambda = 1$ the distribution is called the standard exponential distribution. Its probability density function is

$$f_X(x) = e^{-x}, \; x > 0$$

Sometimes the exponential distribution may not adequately describe a process, particularly, when the rate of event occurrences may change with time, as for example in systems with age-dependent failure rates. In such a case, a generalization of the exponential distribution may be used, as for example the Weibull distribution (Eq. 1), often applied in reliability and quality control work (Weibull 1951; Kao 1958, 1959; Franck 1988; Berrettoni 1964) since it may accommodate rate variations through the proper choice of its parameters.

A random variable X has a Weibull distribution if there are values of the parameters c, α, and β such that

$$Y = \left(\frac{X - \beta}{\alpha} \right)^c$$

has the standard exponential distribution with probability density function

$$f_Y(y) = e^{-y}, \; y > 0$$

The probability density function of the Weibull random variable X is then

$$f_x(x) = \frac{c}{\alpha} \left(\frac{x - \beta}{\alpha} \right)^{c-1} e^{-\left[(x-\beta)/\alpha \right]^c}, \; x > \beta$$

and the cumulative distribution function is

$$F_X(x) = 1 - e^{-[(x-\beta)/\alpha]^c}, \; x > \beta \qquad (1)$$

The Weibull survival (or reliability) function is

$$R_X(x) = 1 - F_X(x), \; x > \beta$$

The Weibull distribution is a power transformation of the exponential distribution, presenting a convenient way to introduce some flexibility to fit a model through the power (or shape) parameter c, thus becoming suitable when the conditions for "strict randomness" needed for the exponential distribution are not fulfilled.

Another generalization of the exponential distribution to describe a process with piece-wise changes in the rate of event occurrences is a generalized mixture of exponentials, defined as the weighted sum of the component distributions

$$f(t|\Lambda) = \sum_{j=1}^{m} w_j f_j(t|\lambda_j)$$

where t is the time between events, and the parameters $\Lambda = (w_1, \ldots w_m, \lambda_1, \ldots \lambda_m)$ are such that $w_i > 0$ for ($j = 1, \ldots, m$), and $\sum_{i=1}^{m} w_i = 1$. w_j is a weighting factor, and f_i an exponential density function parameterized by λ_j. More generally, a mixture distribution can be composed of m component distributions f_j, each of a different type.

Feldmann and Whitt (1998) showed that any monotone probability distribution function can be approximated by a finite mixture of exponentials. They also showed that a Mixture of Exponentials distribution is especially useful in modeling long-tailed data without some of the mathematical complications of other distributions such as the Pareto (Johnson and Kotz, 1953) and Weibull probability distributions. The Mixture of Exponentials distribution (MOED), also called the hyperexponential distribution, has also been applied (referred to as the Schuhl distribution) to study headway (time between successive vehicles) in traffic flow models (Petigny 1966), to represent some demographic distributions (Susarla and Pathala, 1965) and several other applications (Titterington *et al*., 1985, Everitt and Hand, 1981, among others).

A mixture of m exponentials cumulative distribution function has the form:

$$F(t|\Lambda) = \sum_{j=1}^{m} w_j (1 - e^{-\lambda_j t}) \qquad (2)$$

with a survival probability distribution:

$$S(t|\Lambda) = 1 - F(t|\Lambda) \; ,$$

and a probability density function:

$$f(t|\Lambda) = \sum_{j=1}^{m} w_j \lambda_j e^{-\lambda_j t} \; ,$$

where λ_j, $w_j > 0$ for ($j = 1, \ldots, m$), and $\sum_{i=1}^{m} w_i = 1$.

The conditional probability of at least one event occurring within the next t years, and the most recent event occurred s years ago (assuming a duration t in years) is

$$P(T \le s + t | T > s) = 1 - \frac{1 - F(s+t)}{1 - F(s)}$$

The MOED is particularly useful to model eruption sequences when the distribution of the eruption rate varies upon translation in a fixed interval (Cox and Lewis, 1966) and develops as a succession of eruptive regimes, each with its own characteristic eruption rate. The MOED has been used successfully in different volcanoes of Mexico that showed piece-wise regimes of activity (Mendoza-Rosas and De la Cruz Reyna 2009; 2010), and to model the time between dome emplacements of the ongoing lava dome eruption of Popocatépetl volcano (Mendoza Rosas *et al*., 2017). Similarly, Dzierma and Wehrmann (2010) and Wehrmann and Dzierma (2011) have used the MOED to describe the activity of the Chilean Southern Volcanic Zone.

The MOED was chosen for its mathematical simplicity involving a direct description of the different sub-populations or regimes, thus accommodating the non-stationary behavior. Mendoza-Rosas and De la Cruz Reyna (2009; 2010) obtained the parameters λ_j´s as the rates of the single exponential distributions, namely the number of events for the duration of each regime j. In dealing with the applications of the MOED to volcanic processes, the calculation of the weighting factors is very important, since the eruptive regimes often develop as a succession of relatively short high-rate regimes, followed by relatively long low-rate regimes in such a way that the regimes fluctuate around an approximately constant trend. We thus calculate the weighting factors w_j´s as the normalized complement of the corresponding proportions of the duration of regimes:

$$w_i = \frac{D_t - D_i}{\sum_{i=1}^{m}(D_t - D_i)}$$

Where D_t is the duration of the whole sampled interval, and D_i is the duration of each identified regime.

Here, we apply the MOED to the non-stationary eruptive column data for the period 1997 to 2003. The identification of regimes was done in two ways. First by eye, inspecting the cumulative curve for evident slope changes (red lines in Figure 2) and second, using a method based on statistical process control to discriminate between inherent variations of the observed repose times and significant variations that signals a change in the regimes (Ho, 1992) (green lines in Figure 7). Figures 2 and 7 show six distinct regimes divided by red and green lines respectively until 2003; after that the behavior is stationary. Considering the different identification methods of the regimes, we calculated MOED 1 and MOED 2 using the visual selection method (Figure 2) and the Ho method (Figure 7) respectively for the period 1997-2003 (table 1).

Considering that the second period of activity 2003-2016 behaves as a stationary process, we analyzed it using the exponential and the Weibull distributions (Table 2).

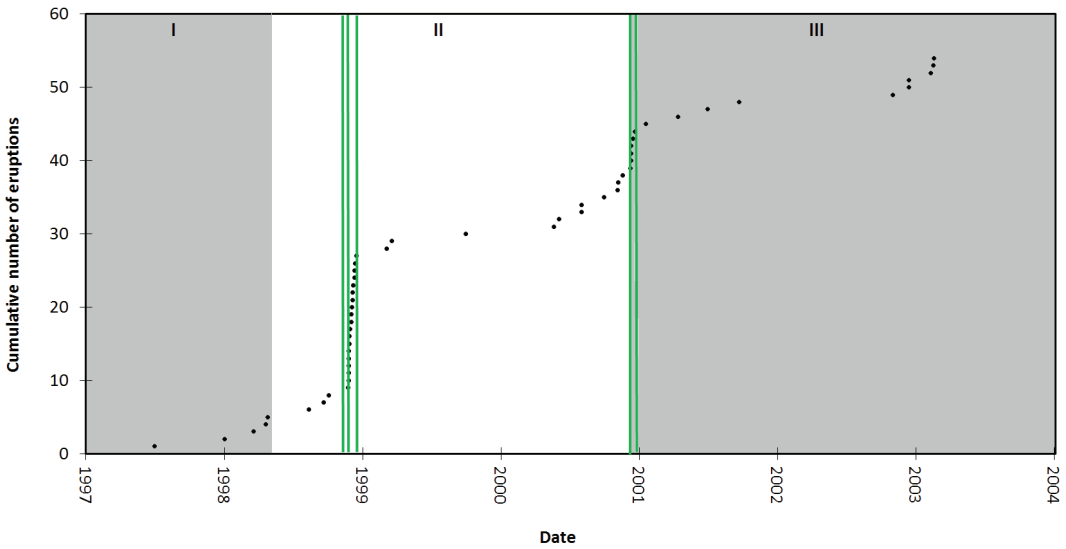

Figure 7. The vertical lines separate the regimes obtained with the statistical process control method developed by Ho (1992) at a 0.05 significance level for the non- stationary period Jun 30, 1997- February 2003. The alternated gray and white areas (Roman numerals) represent the regimes of lava dome emplacements described in Gómez-Vázquez *et al*. (2016) and Mendoza-Rosas *et al.* (2017).

Table 1. Parameters of different distributions for the non-stationary period 1997-2003.

Eruptive columns ≥ 4 km above the summit in period from Jun 30, 1997 to February 2003

Weibull		MOED 1			MOED 2			
Shape 0.59	Regimes identified "by eye"	Weighting factors (w_i)	Monthly rate (λ_i)	No. events	Regimes identified with the method of Ho (1992)	Weighting factors (w_i)	Monthly rate (λ_i)	No. events
Scale 25.82	I (30/06/1997--25/11/1998)	0.1503	0.5259	9	I (30/06/1997-25/11/1998)	0.1503	0.5259	9
	II (26/11/1998-18/12/1998)	0.1978	24.0564	18	II (26/11/1998-28/11/1998)	0.1997	33.9089	3
	III (19/12/1998-03/10/2000)	0.1365	0.3202	7	III (29/11/1998-18/12/1998)	0.1981	22.7352	15
	IV (04/10/2000-22/01/2001)	0.1892	2.6998	10	IV (19/12/1998-13/12/2000)	0.1296	0.4954	12
	V (23/01/2001-06/11/2002)	0.1367	0.1839	4	V (14/12/2000-24/12/2000)	0.1989	10.6502	4
	VI (07/11/2002-23/02/2003)	0.1894	1.3733	5	VI (25/12/2000-23/02/2003)	0.1234	0.3793	10

The resulting probabilities of occurrence of at least one eruptive activity generating eruptive columns ≥ 4 km above the summit for both periods are listed in Table 3, and depicted in Figure 8.

The goodness of fit of the probability distributions and the observed data were evaluated using Kolmogorov-Smirnov tests for both periods, listed in Table 4. For the 1997-2003 period the goodness of fit results for the MOED 1 and the Weibull distributions are similar. On the other hand, the MOED 2 distribution shows a poorer fit to the observed data indicated by the relatively high values of the K-S statistics.

For the period 2003-2016, the Weibull and the Exponential distributions are equally acceptable to model the process since both pass the fit tests to the 0.05 significance level.

Discussion and conclusions

We analyze the statistical features of the SE with column heights ≥4km of the ongoing lava dome eruption of Popocatépetl volcano for the period 1997-2016. The independence and stationarity tests for the whole series of significant explosions revealed the non-independence and non-stationary character of the sequence of time intervals between events, making it difficult to make a simple statistical description of the process. However, we found that the behavior of the SE sequence changed in 2003. We thus separated it in two periods or stages, both showing independence among the time intervals between events, but with the first period (1997-2003) presenting a non-stationary behavior, while the second period maintained a steady behavior. To describe the sequence of SE, we tested several distributions for each of those stages. For the first non-stationary

Table 2. Parameters of the exponential and Weibull distributions for the period with stationary behavior: 2003-2016

Eruptive columns ≥ 4 km above the summit from February-2003 to the last event in 2016

Exponential distribution	Weibull distribution
Monthly rate (eruptions/month): 0.072	Shape parameter: 1.30 Scale parameter: 370.47

Table 3. Probabilities of occurrence of at least an eruptive activity with column height ≥4km over the summit over different time intervals (T days). Probabilities were separately calculated for the periods from Jun 1997 to February, 2003 (non-stationary), and February, 2003 to the last event in 2016 (stationary).

Non-stationary period from Jun 30 , 1997 to February, 2003			
T (days)	Weibull	MOED 1	MOED 2
30	0.6649	0.6376	0.7478
60	0.8082	0.7679	0.8416
90	0.8777	0.8348	0.9001
180	0.9581	0.9282	0.9743
240	0.9769	0.9558	0.9894
360	0.9917	0.9817	0.9981
420	0.9948	0.9879	0.9992
Stationary period from February, 2003 to last eruptive activity in 2016			
T (days)	Weibull	Exponential	
30	0.0372	0.0691	
60	0.0892	0.1335	
90	0.1465	0.1934	
180	0.3234	0.3494	
240	0.4334	0.4363	
360	0.6184	0.5768	
420	0.6920	0.6333	
720	0.9071	0.8209	
1440	0.9971	0.9679	

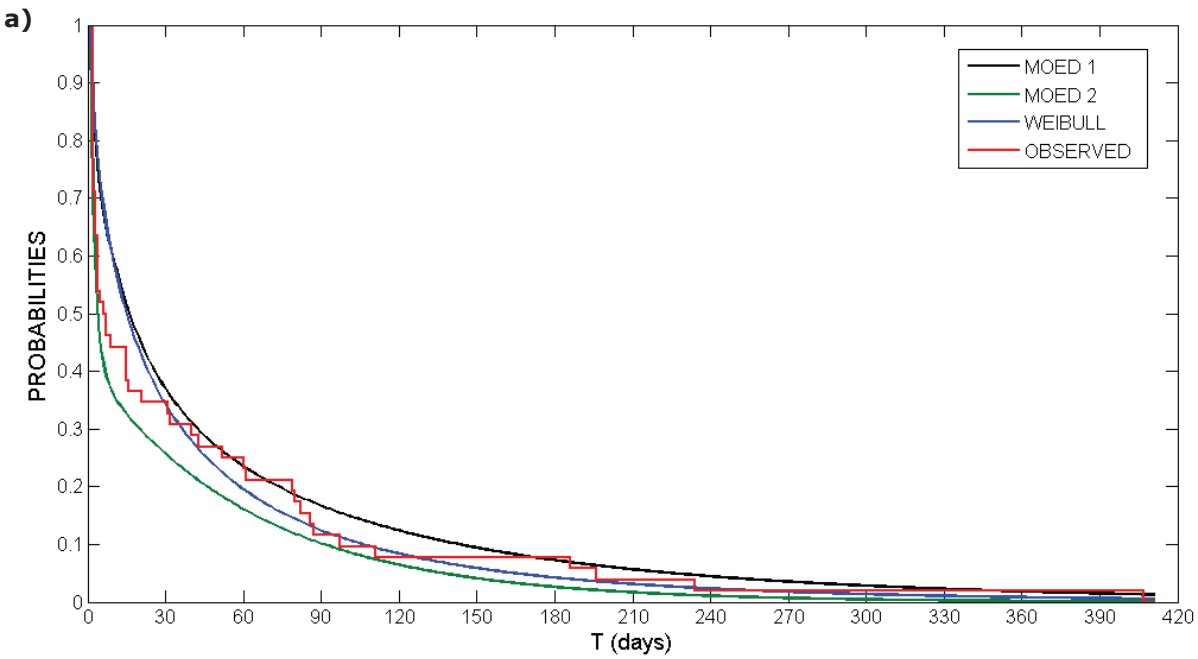

Figure 8. Probabilities of an eruptive activity with column height ≥4km above the summit exceeding an interval of t days calculated with different cumulative distribution functions from a) Jun, 1997 to February, 2003, and b) February, 2003 to the last event of 2016.

b)

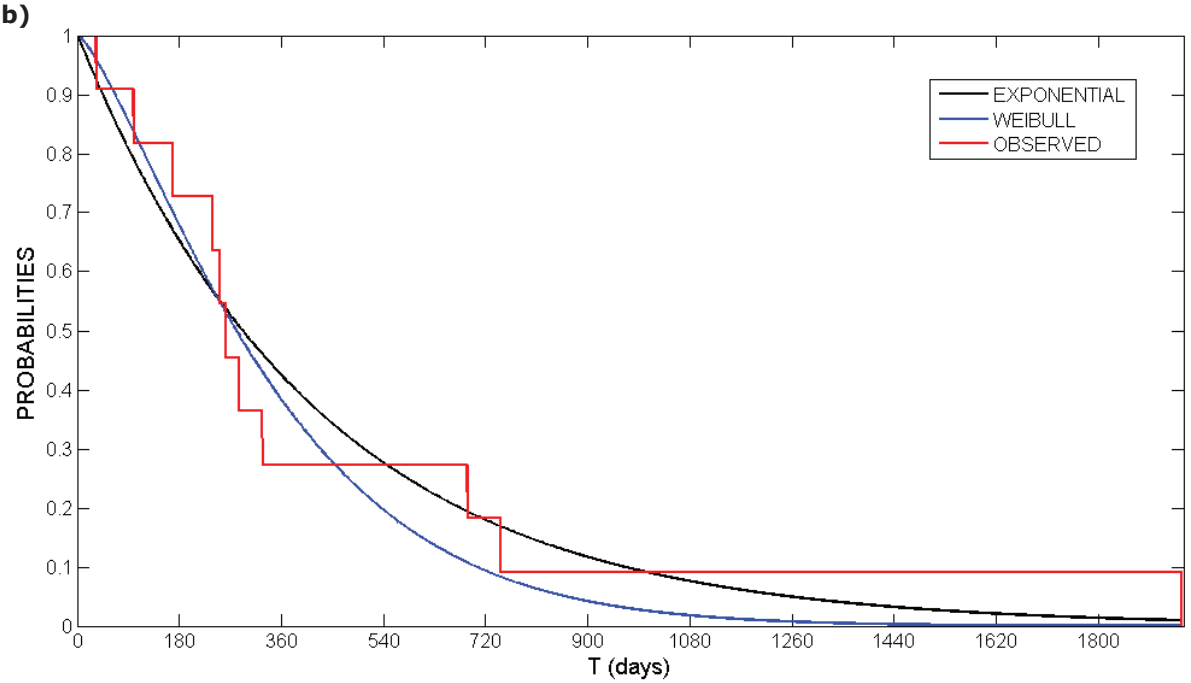

Figure 8. Continue.

Table 4. Kolmogorov-Smirnov statistics goodness of fit test for the different statistical distributions over two different periods of time. All distribution fits may be accepted at the 0.05 significance level.

Eruptive activity with column heights ≥4km in the period 1997 -2003

	Kolmogorov Smirnov Statistic	Pass K-S test?
MOED 1	0.0498	Yes (≤0.170)
MOED 2	0.0747	Yes (≤0.170)
Weibull	0.0351	Yes (≤0.170)

Eruptive activity with column heights ≥4km in the period from 2003 -2016

	Kolmogorov Smirnov Statistic	Pass K-S Test?
Exponential	0.2157	Yes (≤0.410)
Weibull	0.1951	Yes (≤0.410)

stage we tried the Weibull distribution and the Mixture-of-Exponentials Distribution (MOED), and for the second stationary stage, the Weibull and the Exponential distributions.

Fitting a MOED distribution requires a careful identification of the type of time dependence (non-stationarity) of the process. In the present case, we found that the time-dependence was characterized by a succession of alternate regimes with high and low rates of event occurrences. To identify the regimes, we first used a direct approach visually inspecting the curve of the cumulative number of explosions for significant slope changes separating high and low rates of occurrences as illustrated in Figure 2, and then a computational method based on statistical process control (Ho, 1992), depicted in Figure 7. The results are compared in Tables 1 and 3.

For the first, non-stationary stage, Weibull and MOED 1 provided the best results in the goodness of fit test, but we prefer MOED 1 since the distribution parameters are easier to calculate and depict a direct representation of physically meaningful features of the process, namely the rates of each of the identified regimes.

Table 5. Ratios of the probabilities calculated for the non-stationary (N-S) and stationary (S) stages for different waiting time intervals.

Days	(N-S stage Weibull)/(S-stage Weibull)	(N-S stage stage MOED1)/(S-stage Exponential)
30	17.89	9.221
60	9.06	5.751
90	5.99	4.316
120	4.46	3.521
240	2.25	2.191
360	1.60	1.702
420	1.44	1.560

For the second, stationary stage, the Weibull and the Exponential distributions yield similar results.

Table 3 and Figure 8 show a marked difference between the probabilities of occurrence of significant explosions for each stage. For comparative purposes we show in Table 5 the ratios of the probabilities calculated for the non-stationary (N-S) and stationary (S) stages for different time intervals.

During the time of study about 40 domes have been emplaced, but at least 138 moderately large explosions were recorded, either during the growth, or during the dome destruction episodes, with 64 of them exceeding an altitude of about 9.5 km a.s.l. Considering the fact that the highest rates of SE occurred during the relatively low lava dome emplacement rate regimes II and the initial part of IV defined in Gómez-Vazquez *et al*. (2016), it may be concluded that the lava dome emplacement and the SE sequences appear to be the result of different ways of interaction among some complex processes, mainly the magma ascent and crystallization rates and the intensity of degassing (Gómez-Vazquez *et al*., 2016; Mendoza-Rosas *et al*., 2017). Such factors seem to influence SE and lava dome emplacements in different ways, particularly during the SE non-stationary stage 1997-2003. In contrast, the SE stationary stage does not show a significant influence of the lava dome emplacement transitions between regimes IV and V.

Since the nature of the process may change from stationary to non-stationary without a clear or evident physical cause, and the probabilities are quite sensitive to such condition, the assessment of hazards requires a continuous testing of the independence and the stationarity of the ongoing process. The eruptive process apparently continues in a stationary stage, but a transition into a non-stationary stage may increase by an order of magnitude the probability of significant explosions in short time intervals, making it more likely the generation of "significant explosion swarms" as those shown in Figure 4. Since this indicates a much higher rate of thermal energy release, the hazard assessment must carefully evaluate the mass and energy balance of the volcano apparently reached around 2003 (Figure 12 in Gómez-Vazquez *et al*., 2016). This acquires particular relevance for the long-term development plans of the volcano surrounding area, considering that about 20% of the major explosive eruptions worldwide have occurred during andesitic or dacitic lava dome eruptions (Ogburn *et al*., 2015), and that the log-linear regression model for compositional dependence of the expected duration of ongoing lava dome eruptions of Wolpert *et al*. (2016), indicates that there is a 40% probability that the ongoing activity of Popocatépetl may last for another 30 to 35 years and 20% probability that it extends for over 100 y.

Acknowledgements

The authors are grateful to the Associate Editor, Dr. Roberto Carniel, and to both anonymous reviewers for their constructive and useful comments and suggestions. This research has been supported by DGAPA-PAPIIT, grant IN109616 for which we are thankful.

References

Álvarez-Ramírez J., Sosa E., Rodríguez E., 2009, Assessing Temporal-Dependent Correlations in the 2000-2008 Popocatépetl Exhalation Sequence by Using Detrended Fluctuation Analysis. J. Volcanol. Geotherm. Res., 186 (3–4): 426–31.

Bebbington M.S., 2007, Identifying Volcanic Regimes Using Hidden Markov Models. Geophys. J. Int., 171 (2): 921–942.

Bebbington M.S., Lai C.D., 1996, Statistical Analysis of New Zealand Volcanic Occurrence Data. J. Volcanol. Geotherm. Res., 74 (1–2): 101–110.

Berrettoni J.N., 1964, Practical applications of the Weibull distribution. Industrial Quality Control, 21(1): 71-79.

Boudal C., Robin C., 1989, Volcán Popocatépetl: recent eruptive history, and potential hazards and risks in future eruptions. In: Latter JH (ed) Volcanic hazards. IAVCEI proc. Volcanol., Springer, Berlin, 110–128.

Cox D.R., Lewis P.A.W., 1966, The statistical analysis of series of events. Methuen and Co., London. 285 pp.

Cox D.R., Miller H.D., 1965, The theory of stochastic processes. Methuen, London. 398 pp.

De la Cruz-Reyna S., 1991, Poisson-Distributed Patterns of Explosive Eruptive Activity. Bull. Volcanol., 54 (1): 57–67.

De la Cruz-Reyna S., 1993, Random Patterns of Occurrence of Explosive Eruptions at Colima Volcano, Mexico. J. Volcanol. Geotherm. Res., 55 (1–2): 51–68.

De la Cruz-Reyna S., 1996, Long-Term Probabilistic Analysis of Future Explosive Eruptions. In R. Scarpa and R.I Tilling, Eds, Monitoring and Mitigation of Volcano Hazards. Springer-Verlag, Berlin-Heidelberg. Doi:10.1007/978-3-642-80087-0.

De la Cruz-Reyna S., Siebe C., 1997, The giant Popocatépetl stirs. Nature, 388(6639):227.

De la Cruz-Reyna, S., Tilling R.I., 2008, Scientific and Public Responses to the Ongoing Volcanic Crisis at Popocatépetl Volcano, Mexico: Importance of an Effective Hazards-Warning System. J. Volcanol. Geotherm. Res., 170 (1–2): 121–134.

De la Cruz-Reyna S., Tilling R.I., Valdés-González C., 2017, Challenges in responding to a sustained and continuing volcanic crisis: The case of Popocatépetl volcano, Mexico, 1994-present. In: Observing The Volcano World: Volcano Crisis Communication. (Eds. C J Fearnley, B. McGuire, G. Jolly, D. Bird and K. Haynes). Springer-Verlag Advances In Volcanology series, DOI: 10.1007/11157_2016_37

Delgado-Granados H., Cárdenas González L., Piedad Sánchez N., 2001, Sulfur Dioxide Emissions from Popocatépetl Volcano (Mexico): Case Study of a High-Emission Rate, Passively Degassing Erupting Volcano. J. Volcanol. Geotherm. Res., 108 (1–4): 107–20.

Dzierma Y., Wehrmann H., 2010, Eruption Time Series Statistically Examined: Probabilities of Future Eruptions at Villarrica and Llaima Volcanoes, Southern Volcanic Zone, Chile. J. Volcanol. Geotherm. Res., 193 (1–2): 82–92.

Everitt B.S., Hand D.J., 1981, Finite mixture distributions. Monographs on Applied Probability and Statistics. Chapman and Hall, London. 143 pp.

Feldmann A., Whitt W., 1998, Fitting mixtures of exponentials to long-tail distributions to analyze network performance models. Perform. Evaluation., 31: 245-279.

Franck J. R., 1988, A simple explanation of the Weibull distribution and its applications, Reliability Review, 8, No. 3, 6-9.

Gómez-Vázquez A., De la Cruz-Reyna S., Mendoza-Rosas A.T., 2016, The ongoing dome emplacement and destruction cyclic process at Popocatépetl volcano, central Mexico. Bull. Volcanol., 78:58.

Grutter M., Basaldud R., Rivera C., Harig R., Junkerman W., Caetano E., Delgado-Granados H., 2008, SO 2 Emissions from Popocatépetl Volcano: Emission Rates and Plume Imaging Using Optical Remote Sensing Techniques. Atmos. Chem. Phys., 8: 6655–63.

Ho CH., 1992, Statistical control chart for regime identification in volcanic time series. Math Geol., 24: 775. https://doi.org/10.1007/BF00890701

Jaquet O., Carniel R., 2001, Stochastic modelling at Stromboli: a volcano with remarkable memory. J. Volcanol. Geotherm. Res., 105, 249–262.

Jaquet O., Carniel R., 2006, Estimation of volcanic hazard using geostatistical models, in: Statistics in Volcanology, edited by: Mader, H. M., Coles, S. G., Connor, C. B., and Connor, L. J., IAVCEI Publications n.1., Geological Society, London, UK, 89– 103.

Jaquet O., Sparks R.S.J., Carniel R. 2006, Magma memory recorded by statistics of volcanic explosions at the Soufrière Hills volcano, Montserrat . In: Mader, H. M., Coles, S. G., Connor, C. B., Connor, L. J. (eds) Statistics in Volcanology. Geological Society, London, Special Publications of IAVCEI, 1, 175–184.

Johnson N.L., Kotz S., 1953, Distributions in Statistics: Continuous Univariate Distributions. Houghton Mifflin Company, United States. 1. 300 pp

Kao J.H.K., 1958, Computer methods for estimating Weibull parameters in reliability studies. Transactions of IRE-Reliability and Quality Control, 13, 15-22.

Kao J.H.K., 1959, A graphical estimation of mixed Weibull parameters in life-testing electron tubes. Technometrics, 1, 389-407.

Klein F.W., 1982, Patterns of Historical Eruptions at Hawaiian Volcanoes. J. Volcanol. Geotherm. Res., 12 (1–2): 1–35.

Martin-Del Pozzo A.L, González-Morán T., Espinasa-Pereña R., Butrón M.A., Reyes M., 2008, Characterization of the recent ash emissions at Popocatepetl Volcano, Mexico. J. Volcanol. Geotherm. Res., 170: 61–75.

Martin-Del Pozzo A.L, 2012, Precursors to eruptions of Popocatépetl Volcano, Mexico. Geofis. Int., 51-1: 87-107.

Mendoza-Rosas A.T., De la Cruz-Reyna S., 2008, A Statistical Method Linking Geological and Historical Eruption Time Series for Volcanic Hazard Estimations: Applications to Active Polygenetic Volcanoes. J. Volcanol. Geotherm. Res., 176(2): 277–290.

Mendoza-Rosas, A.T., De la Cruz-Reyna S., 2009, A Mixture of Exponentials Distribution for a Simple and Precise Assessment of the Volcanic Hazard. Nat. Hazards. Earth. Syst. Sci., 9 (2): 425–431.

Mendoza-Rosas A.T., De La Cruz-Reyna S., 2010, Hazard Estimates for El Chichón Volcano, Chiapas, México: A Statistical Approach for Complex Eruptive Histories. Nat. Hazards. Earth. Syst. Sci., 10 (6): 1159–70.

Mendoza-Rosas A.T., Gómez-Vázquez A., De la Cruz-Reyna S., 2017, Statistical Analysis of the Sustained Lava Dome Emplacement and Destruction Processes at Popocatépetl Volcano, Central México. Bull. Volcanol., 79 (6).

Newhall C.G. and Self S., 1982, The Volcanic Explosivity Index (VEI): An estimate of explosive magnitude for historical volcanism. J. Geophys. Res., 87: 1231-1238. doi: 10.1029/JC087iC02p01231.

Ogburn S.E., Loughlin S.C., Calder E.S., 2015, The association of lava dome-growth with major explosive activity (VEI ≥ 4): DomeHaz, a global dataset, Bull. Volcanol., 77(40), doi:10.1007/s00445-015-0919-x.

Petigny B., 1966, Extension de la distribution de Schuhl. Annales des Ponts et Chaussies, 136, 77-84.

Ramos-Jimenez, 2017, This issue

Robin C., Boudal C., 1987, A Gigantic Bezymianny-Type Event at the Beginning of Modern Volcan Popocatepetl. J. Volcanol. Geotherm. Res., 31 (1–2): 115–30.

Siebe C., Abrams M., Macías J.L., 1995. Derrumbes gigantes, depósitos de avalancha de escombros y edad del actual cono del Volcán Popocatépetl. Volcán Popocatépetl, Estudios realizados durante la crisis de 1994–1995. In: Comité Científico Asesor UNAM-CENAPRED: Volcán Popocatépetl, estudios realizados durante la crisis de 1994–1995. Edición Especial, Secretaría de Gobernación, 195–220.

Siebe C., Abrams M., Macías J.L., Obenholzner J., 1996. Repeated Volcanic Disasters in Prehispanic Time at Popocatépetl, Central Mexico: Past Key to the Future?. Geology, 24 (5): 399–402.

Siebe C., Macías J., Abrams M., Rodríguez S., Castro R., 1997, Catastrophic prehistoric eruptions at Popocatépetl and Quaternary explosive volcanism in the Serdán-Oriental basin, east-central México. Pre-meeting excursion fieldtrip guidebook No 4, Jan 12–18: Puerto Vallarta, México, International Association of Volcanology and Chemistry of the Earth's Interior (IAVCEI) General Assembly, 88 pp.

Siebe C., Macías J.L., 2006, Volcanic hazards in the Mexico City metropolitan area from eruptions at Popocatépetl, Nevado de Toluca, and Jocotitlán stratovolcanoes and monogenetic scoria cones in the Sierra Chichinautzin Volcanic Field: Penrose Conference, Geol. Soc. Am., 1-77.

Siebe C., Salinas S., Arana-Salinas L, Macías JL, Gardner J, Bonasia R., 2017, The ~23,500

y 14^{C} BP White Pumice Plinian eruption and associated debris avalanche and Tochimilco lava flow of Popocatépetl volcano, México. J. Volcanol. Geotherm. Res., 55 (1–2): 51–68.

Sosa-Ceballos G., Gardner J.E., Siebe C., Macías J.L., 2012, A caldera-forming eruption~ 14,100 14^{C} yr BP at Popocatépetl volcano, México: Insights from eruption dynamics and magma mixing. J. Volcanol. Geotherm. Res., 213, 27-40.

Susarla V., Pathala K. S., 1965, A probability distribution for the time of first birth. Journal of Scientific Research, Banaras Hindu University, 16, 59-62.

Titterington D.M., Smith A.F.M., Makov U.E., 1985, Statistical Analysis of Finite Mixture Distributions, New York: Wiley. 243 pp.

Wehrmann H., Dzierma Y., 2011, Applicability of Statistical Eruption Analysis to the Geological Record of Villarrica and Lanín Volcanoes, Southern Volcanic Zone, Chile. J. Volcanol. Geotherm. Res., 200 (3–4): 99–115.

Weibull W., 1951, A statistical distribution of wide applicability. J. Appl. Mech., 18, 293-297.

Wolpert R.L., Ogburn S.E., Calder E. S., 2016, The longevity of lava dome eruptions. J. Geophys. Res. Solid Earth, 121(2), 676-686.

Geofísica Internacional (2019) 58-1: 49-72

Original paper

Fragmentation behavior of eruptive products of Popocatépetl volcano: an experimental contribution

Miguel Angel Alatorre-Ibargüengoitia, Alejandra Arciniega-Ceballos, Carlos Linares López, Donald B. Dingwell and Hugo Delgado-Granados

Received: January 16, 2018; accepted: September 25, 2018; published on line: January 18, 2019

Resumen

En este artículo se presenta un estudio experimental del comportamiento de fragmentación de muestras naturales del volcán Popocatépetl en un tubo de choque. Estos experimentos simulan explosiones Vulcanianas como las que han ocurrido en el volcán Popocatépetl desde su reactivación en 1994. Aquí detallamos el comportamiento de varios parámetros incluyendo la presión umbral de fragmentación, rapidez de fragmentación, velocidad de emisión y eficiencia de fragmentación. Nuestros resultados indican que la porosidad interconectada de la roca y la presión aplicada ejercen una fuerte influencia en el proceso de fragmentación. Los valores de la presión umbral de fragmentación que se presentan aquí proporcionan estimaciones cuantitativas de la sobrepresión requerida para generar una explosión en el volcán Popocatépetl. Así mismo, presentamos las primeras estimaciones de la rapidez de fragmentación a temperaturas magmáticas.
La eficiencia de fragmentación de los piroclastos generados experimentalmente es evaluada a través de la teoría fractal de fragmentación y observamos que su granulometría puede ser influenciada significativamente por la composición y la textura de la matriz. La granulometría de depósitos de caía asociados a diferentes eventos explosivos del volcán Popocatépetl también muestran un comportamiento fractal, pero con dimensiones fractales mayores a las correspondientes a las partículas generadas experimentalmente, lo cual es consistente con la ocurrencia de procesos de fragmentación secundarios durante las erupciones.
Finalmente, presentamos información extraída de señales elastoacústicas asociadas con los procesos de fragmentación. El análisis de los resultados experimentales que se presentan aquí son útiles para calibrar modelos eruptivos e interpretar datos de monitoreo de las erupciones de volcanes con composición intermedia y de este modo contribuyen al mejoramiento de la evaluación del peligro de estos riesgosos volcanes.

Palabras clave: Volcán Popocatépetl, erupciones volcánicas, erupciones Vulcanianas, peligros volcánicos, experimentos, fragmentación magmática, tubo de choque.

M. A. Alatorre-Ibargüengoitia*
Instituto de Investigación en Gestión de Riesgo
y Cambio Climático
Universidad de Ciencias y Artes de Chiapas
Libramiento Norte poniente 1150, Lajas Maciel
Tuxtla Gutiérrez, 29039
Chiapas, México
**Corresponding author: miguel.alatorre@unicach.mx*

A. Arciniega-Ceballos
C. Linares López
H. Delgado-Granados
Departamento de Vulcanología
Instituto de Geofísica
Universidad Nacional Autónoma de México
Ciudad Universitaria
Delegación Coyoacán 04510
México CDMX, México

M. A. Alatorre-Ibargüengoitia
D. B. Dingwell
Department of Earth and Environmental Sciences
Ludwig Maximilians University of Munich
Theresienstrasse 41, 80333
Munich, Germany

Abstract

The fragmentation behavior of eruptive products from Popocatépetl has been investigated experimentally in a shock-tube apparatus. Rapid decompression experiments have been performed that mimic Vulcanian explosions that have occurred at Popocatépetl since its reawakening in 1994. We detail the behavior of several fragmentation parameters including the fragmentation threshold, fragmentation speed, ejection velocity and fragmentation efficiency. Our results confirm that the connected porosity of the rock and the applied pressure are strong influences on the fragmentation process. The values of the fragmentation threshold presented here provide quantitative constraints on the overpressure required to generate an explosion at Popocatépetl. We also present the first experimental estimates of the fragmentation speed at magmatic temperatures.
We have further applied fractal fragmentation theory to the experimentally-generated pyroclasts to evaluate fragmentation efficiency and we observe thereby that groundmass texture and composition may play an important role in the grain-size distribution. The grain-size distributions of ash fall deposits from several explosive events of Popocatépetl exhibit a fractal dimension higher than the experimentally-generated particles, consistent with the occurrence of secondary fragmentation processes at Popocatépetl.
Finally, we analyzed and discussed the information extracted from elasto-acoustic signals associated with the dynamic behavior of the fragmentation process triggered by rapid decompression. The analysis of the experimental results provided in this work are useful for the calibration of eruptive models, the interpretation of the data obtained from monitoring techniques of intermediate composition volcanoes that produce Vulcanian eruptions and may thereby contribute to the improvement of hazard assessment at high risk volcanoes.

Keywords: Popocatépetl Volcano, volcanic eruptions, Vulcanian eruptions, experiments, magmatic fragmentation, shock-tube.

Introduction

Popocatépetl volcano (19.02° N, 98.62° W, with an altitude of 5,452 m above sea level) is located just 70 km from downtown Mexico City within a densely populated region (~500,000 people living within 30 km from the crater, De la Cruz-Reyna and Tilling 2008). The ongoing eruptive activity of Popocatépetl volcano, which began in December 1994, has been characterized by a succession of emplacements and destructions of lava domes. Up to 2016, at least 38 episodes of lava dome formation and destruction by Vulcanian explosions have been identified (Gomez *et al*., 2016; Mendoza-Rosas *et al*., 2017). These explosions have resulted in 1) ash fall on the population around the volcano (up to and including Mexico City and Puebla); 2) volcanic ballistic projectiles, ejected at distances up to 4 km (Alatorre-Ibargüengoitia *et al*., 2012); and 3) pyroclastic flow deposits some of which have triggered lahars on the flanks of the volcano (Capra *et al*., 2004; Macías and Siebe, 2005; Julio-Miranda *et al*., 2005, 2008). This ongoing eruption has understandably generated great concern in the population surrounding the volcano and has attracted the attention of volcanologists worldwide (De la Cruz-Reyna *et al*., 2017).

A number of studies about Popocatépetl have been published including its past eruptive activity (e.g. Boudal and Robin, 1989; Siebe *et al*., 1996; Capra *et al*., 2004; Siebe and Macias, 2006; Mendoza-Rosas and De la Cruz-Reyna, 2008; Arana-Salinas *et al*., 2010; Sosa-Ceballos *et al*., 2012; Martin Del Pozzo *et al*., 2016; Siebe *et al*., 2017), the monitoring of the current eruption (e.g. Arciniega-Ceballos *et al*., 2000, 2008; Delgado-Granado *et al*., 2001; Martin Del Pozzo *et al*., 2008, 2012; Armienta *et al*., 2002, 2008, 2010; Wright *et al*., 2002; Espíndola *et al*., 2004; Cabral *et al*., 2008; Novelo-Casanova and Valdes-González, 2008; Arámbula-Mendoza *et al*., 2010), hazard maps (Macías *et al*., 1995; CENAPRED, 2012) and scientific and public responses to the ongoing volcanic crisis (e.g. De la Cruz-Reyna and Tilling, 2008; De la Cruz-Reyna *et al*., 2017).

A comprehensive understanding of pre- and syn-eruptive processes is, however, still required in order to interpret and evaluate adequately the data from volcanic monitoring. For this, we propose that the scientific investigation of volcanic eruptions no longer depends solely on field data, as direct field observations of eruptive processes are, and likely will always be, restricted in terms of accessibility and safety. Instead, laboratory experiments and theoretical models derived from them are essential assets for our understanding of volcanic processes (Kavanagh *et al*., 2018). For these reasons, laboratory experiments are becoming important in volcanic research and are increasingly used for the

following primary purposes: 1) to explore novel or inaccessible phenomena; 2) to provide systematic observations of the dynamics of volcanic processes; 3) to determine the values of key input parameters for numerical models; and 4) to test hypothesis and validate theoretical and numerical models (Mader *et al*., 2004). For a better understanding of volcanic eruptions and their forecasting, such results of experimental studies must then be integrated into a complete analysis of information sources concerning the eruptive system including field observations, and eruptive models such that all available information is used.

Here, we performed experiments in a so-called "fragmentation bomb", a shock-tube apparatus originally designed by Alidibirov and Dingwell (1996a,b) and subsequently modified to investigate different aspects of magmatic fragmentation of natural samples upon rapid decompression under controlled conditions (e.g. Spieler *et al*., 2004; Mueller *et al*., 2005; Kueppers *et al*., 2006a; Scheu *et al*., 2006; Alatorre-Ibargüengoitia *et al*., 2011; Kremers *et al*., 2010; Richard *et al*., 2013; Cigala *et al*., 2017). This setup mimics Vulcanian eruptions and provides a unique opportunity for the investigation of the fragmentation process, its elasto-accoustic behavior and the dynamics of fragmentation process and the resulting pyroclasts. Below, we present fragmentation experiments using samples from Popocatépetl and provide quantitative data on fragmentation threshold, fragmentation and ejection speeds, and fragmentation efficiency. In addition, we analyze, in time and frequency domains, the microsignals associated with the elasto-acoustic response of the overall fragmentation processes. Thereby, this experimental approach contributes to the understanding of volcanic conduit conditions during fragmentation process as well as the interpretation of field-based seismograms.

Method

Here, the rapid decompression experiments with samples from Popocatépetl were performed using a shock-tube apparatus consisting of two main parts (Figure 1): 1) an autoclave (corresponding to a volcanic conduit), into which cylindrical samples drilled from volcanic rocks were loaded; and 2) a large volume (collection) tank at atmospheric conditions, in which the fragmented sample was contained. Pressurization of the autoclave and subsequent depressurization was regulated by a system of up to three scored diaphragms that open at a precisely defined pressure differential. The sample and autoclave were slowly pressurized with argon gas to the desired experimental pressure. Depressurization of the autoclave is triggered by controlled failure of the uppermost diaphragm, followed by the immediate failure of the other diaphragms, which induces a rarefaction wave that travels through the sample. If the resulting pressure differential is sufficient, the sample fragments brittlely layer-by-layer (Alidibirov and Dingwell, 2000; Scheu *et al*., 2008; Fowler *et al*., 2010; Fowler and Scheu, 2016) and the particles are ejected into the collection tank. We performed fragmentation experiments both at magmatic temperature (heated with an external furnace up to 850 °C) and at room temperature (~ 22 °C) using different autoclaves and piezoelectric sensors to record the elastic response of the system, across the full range of experimental conditions (Figure 1). In order to prevent the sample from being ejected like a projectile, it was attached to a sample holder and tightly inserted in the autoclave.

Where the applied pressure differential was not high enough to fragment the sample entirely, the experiment was successively repeated at a higher pressure using cylinders drilled from the same rock sample, until complete fragmentation was achieved. The minimum pressure differential leading to complete fragmentation is defined as the fragmentation threshold. This threshold was investigated for samples with different porosities (at 850 °C and 22 °C).

In order to investigate the fragmentation efficiency, we waited at least 2 hours after performing each experiment to allow fine ash particle settling according to Stokes' Law (Kueppers *et al*., 2006a). Then we rinsed the collection tank with desalinated water to recover the particles. Applying this technique, we were able to recover more than 99% of the initial sample mass. Dry sieving and weighing was performed at half-ϕ steps ($\phi = \log_2 d$, with d =particle diameter in mm).

A high-speed camera (Phantom V710 and Photron SA-5) at 10,000- 20,000 frames per second was used to film the process and measure the ejection velocities of the gas–particle mixture. In experiments at room temperature, two dynamic pressure transducers (601H, Kistler Instrumente AG, Switzerland), located directly above and below the sample, were used to measure the speed of the fragmentation front traveling into the sample by comparing the corresponding pressure curves recorded during the fragmentation process (Scheu *et al*., 2006).

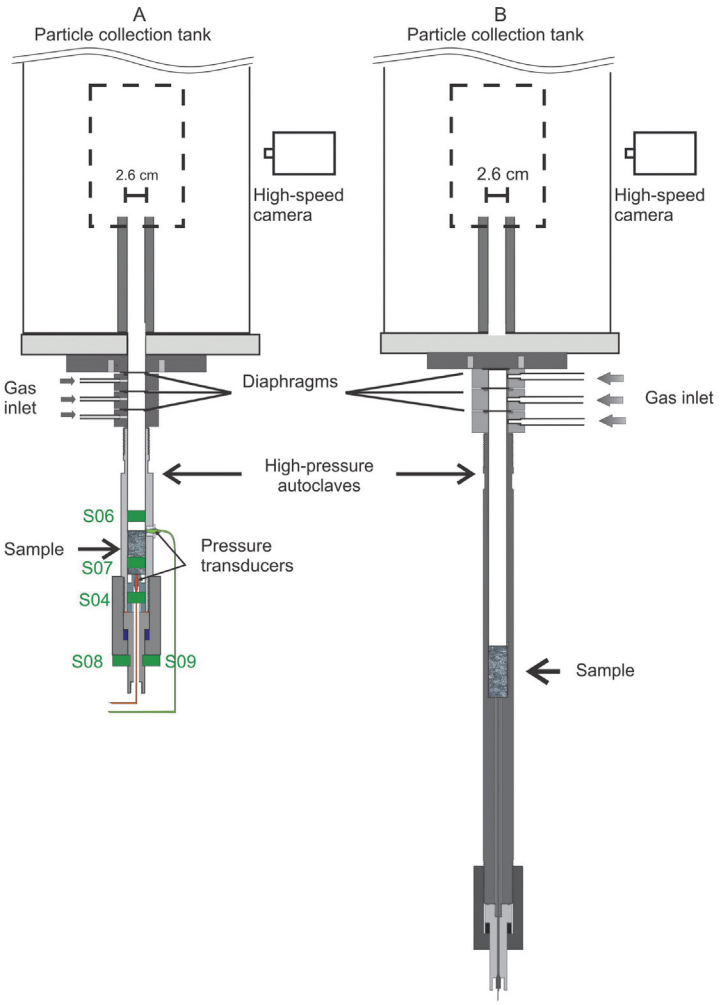

Figure 1. The experimental setup of the fragmentation apparatus. The sample (6 cm length, 2.5 cm diameter) is placed in the high-pressure autoclave. A set of diaphragms allows pressurization of the sample using argon gas. After the disruption of the diaphragms, the particles are ejected into the collection tank at atmospheric conditions. The dashed box indicates the area observed with the high-speed camera (ca. 14 cm high). In the experiments at room temperature (left) two dynamic pressure transducers located directly above and below the sample record the pressure drop during fragmentation. S05, S06 and S07 indicate the position of piezoelectric sensors. In the experiments at 850 °C the autoclave (right) is heated with an external furnace.

The elastic behavior related to the fragmentation experiments was recorded using five high-dynamic piezoelectric sensors (Arciniega-Ceballos *et al*., 2014, 2015), cou-pled on the outer surface of the steel walls and bottom of the autoclave (Figure 1A). These sensors produce an output voltage proportional to the applied compressive or tensile stress or vibration induced by an excitation mechanism. In our experiments, decompression is the excitation mechanism and the sensors capture the direction of motion and the stresses exerted on the system during the fragmentation process. The sensors frequency response covers the entire frequency range of the apparatus at the pressure applied (Arciniega-Ceballos *et al*., 2014).

Samples

We collected several samples from explosive events of Popocatépetl during the 1994-present (2017) eruptive activity. In particular, we selected pumice fragments from the pyroclastic flow deposit produced on January 22, 2001 collected at 2.4-2.7 km from the crater (Smithsonian Institution, 2000) and dense ballistic blocks from a crater dome, which were ejected ballistically during the explosive events of February 2003 that reached a maximum distance of 2.6 km from the crater (Smithsonian Institution, 2003). We measured the density and porosity of all the samples by helium pycnometry (Accupyc 1330, Micrometrics, USA). The porosity distributions of the collected

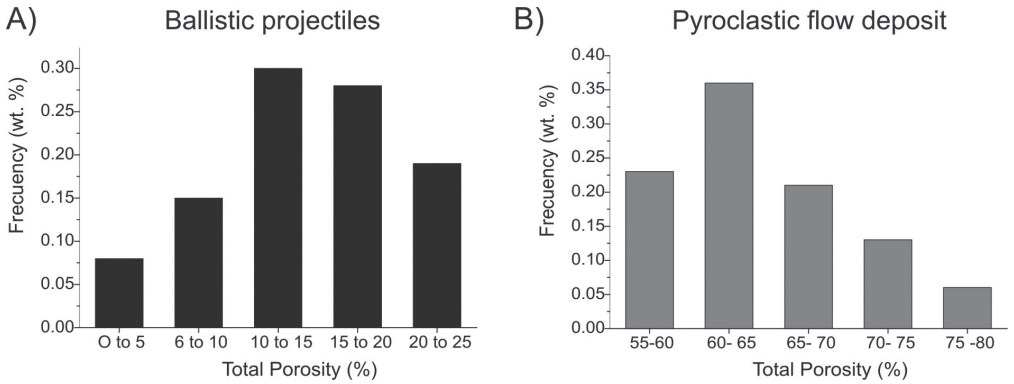

Figure 2. Porosity distribution of the collected samples corresponding to: A) volcanic dense blocks ejected as ballistic projectiles in February 2003; and B) pumice fragments in the pyroclastic flow deposit 2001.

pumice and ballistic blocks corresponding to these events are presented in Figure 2. The bulk rock composition measured by X-ray fluorescence spectroscopy of both kinds of samples, the 2001 pumice and 2003 ballistic blocks, ranges from andesite to dacite (SiO_2 of 61–65%), similar to the compositions reported for other explosive events of Popocatépetl during the 1994-present eruption (Straub and Martin-Del Pozzo, 2001; Martín del Pozzo *et al*., 2003; Witter *et al*., 2005).

Additionally, we also used samples consisting of andesitic pink pumice fragments corresponding to the Plinian eruption ca. 1200 yr. B.P. (Siebe and Macías, 2006) and dense andesitic samples from the Nealticán lava flow from a fissure eruption ca. 2100 yr. B.P. (Siebe and Macías, 2006). The characteristics of all the samples used in the fragmentation experiments are presented in Table 1. In general, phenocrysts are often in contact with the vesicles and neither phenocrysts nor microlites within the groundmass show a clear preferred orientation in the samples. Only the lava samples present relatively spherical vesicles. We did not observe a preferred orientation of bubbles in the others. Thin sections reveal textural differences in the groundmass of the dense ballistic blocks between the andesitic rocks with microcrystalline groundmass and the dacitic rocks with glassy groundmass (Figure 3).

Experimental results and analysis

Fragmentation threshold

The measured fragmentation threshold corresponding to all samples from Popocatépetl considered in this study is presented in Figure 4 including experiments at 850 °C and 22 °C. This Figure shows that the threshold values obtained for Popocatépetl follow a very similar trend as a function of the connected porosity as the values reported for samples corresponding to different volcanoes with a great range of chemical composition, crystallinity and bubble size distribution that were generated during different types of eruptions (Spieler *et al*., 2004). It is worth noting that isolated pores are not pressurized during the experiments, and therefore, their contribution to the energy from gas expansion is negligible.

A comparison of our threshold data measured at room temperature versus the threshold values determined at 850 °C re-vealed that the fragmentation threshold at low and high temperature is similar. For this reason, the results are believed to be applicable to fragmentation over a wide range of temperatures from room temperature up to eruptive temperature, as long as the fragmentation remains in the brittle domain.

Our threshold data can be approximated with the theoretical fragmentation criterion of Koyaguchi *et al*. (2008) which can be expressed as follows:

$$P_{th} = \frac{2S_3(1-\phi)}{3\phi\sqrt{\phi^{-1/3}-1}} \qquad (1)$$

where P_{th} is the fragmentation threshold, ϕ the porosity and S_3 is the effective strength. We found that an effective tensile strength of S_3= 1.5 MPa in Eq. (1) minimize the mean square error (0.89) for the data corresponding to Popocatépetl samples at 850°C (Figure 4). The higher porosity samples of Popocatépetl cannot be adequately fitted by this criterion probably because of their relatively high permeability which significantly reduces the pressure

Table 1. Characteristics of the rock samples considered in this study that where generated during different eruptive events of Popocatépetl and the experiments in which they were used.

Name	**DBm**	**DBg**	**Pu**	**La**	**PP**
Rock type	Dense ballistic blocks	Dense ballistic blocks	Pumice	Lava	Pink Pumice
Eruption	February 2003	February 2003	January 22, 2001	Nealticán lava flow ca. 2100 yr. B.P.	Plinian eruption ca. 1200 yr. B.P.
SiO_2 (%)	61-62	65	61-63	61- 62	61-62
Connected porosity (%)	3-21	14-15	56-73	14-18	42-64
Isolated porosity (%)	1.0-1.5	1.0-1.5	1.5-3.0	1.0	2.5-3.5
Matrix density (kg/m^3)	2670-2680	2600	2400-2500	2700	2330-2490
Phenocryst content (vol. %, vesicle-free basis) and size (mm)	25-45 (<4 mm)	20-40 (<4 mm)	30-50 (<4 mm)	10-20 (< 3mm)	20-30 (< 3mm)
Phenocrysts	Plagioclase, pyroxene, olivine, amphibole, Fe–Ti oxides	Plagioclase, pyroxene, amphibole, and Fe–Ti oxides	Plagioclase, pyroxene, olivine, Fe–Ti oxides	Plagioclase, pyroxene, and olivine	Plagioclase, pyroxene and Fe–Ti oxides
Groundmass	Microcrystalline	Glassy	Glassy	Glassy	Glassy
Experiments used	Threshold, Efficiency	Threshold, Efficiency	Threshold fragmentation and ejection speed	Threshold, fragmentation	Threshold, and ejection speed, Efficiency

differential in and below a fragmentation layer as shown by Mueller *et al*. (2005, 2008). These authors found that the fragmentation behavior is influenced by permeability if this parameter lies above a critical value (~10^{-12} m^2).

Fragmentation and ejection speeds

We performed experiments with three set of samples with different porosities (La with ϕ = 17%, PP with ϕ = 43 % and 61 %). In each experiment performed at room temperature, the fragmentation speed was calculated from the distance between the dynamic pressure transducers and the time delay between the pressure drops of the signals (Scheu *et al*., 2006). The results are presented in Figure 5A relative to the applied pressure (P_o). The relationship between the fragmentation speed and the applied pressure can be fitted empirically using a logarithmic expression (Scheu *et al*., 2006) that can be defined as follows (Alatorre-Ibargüengoitia *et al*., 2011):

$$U = k_p \ln(P_o/P_{th}) \quad (2)$$

where k_p is a constant with velocity units that depends on the porosity of the sample. The fragmentation speed measured from Popocatépetl´s samples are comparable with the values measured from samples of other volcanoes (Scheu *et al*., 2006; Richard *et al*., 2013).

The velocity of the front of the gas–particle mixture was measured via high-speed videography by considering the average of the velocities of several particles traveling at this

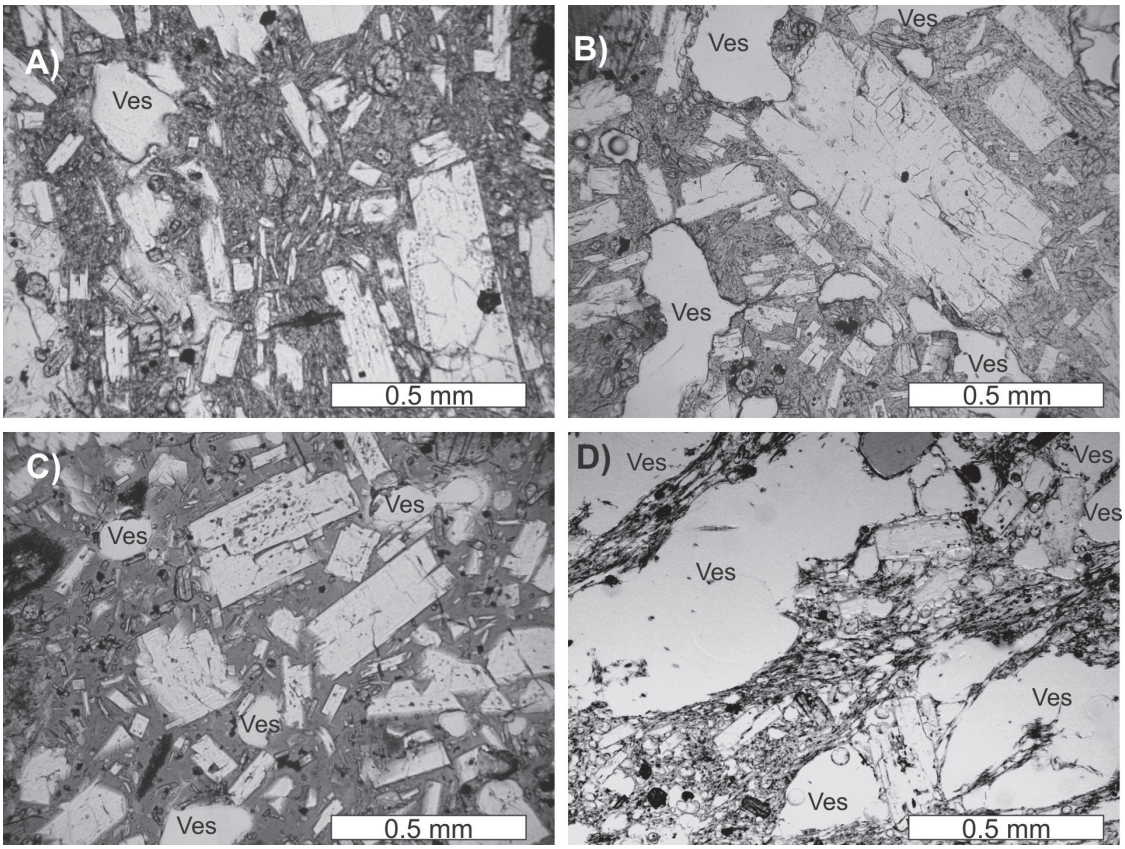

Figure 3. Photomicrographs of petrographic thin sections of Popocatépetl samples generated during the present eruptive period used in this study. A) and B) Dense andesite with microcrystalline groundmass (DBg) and connected porosity of 14% and 20%, respectively; C) Dense dacite with glassy groundmass (DBm) and connected porosity of 14%; D) Pumice fragment (Pu) with connected porosity of 60% corresponding to the 2001 pyroclastic flow deposit.

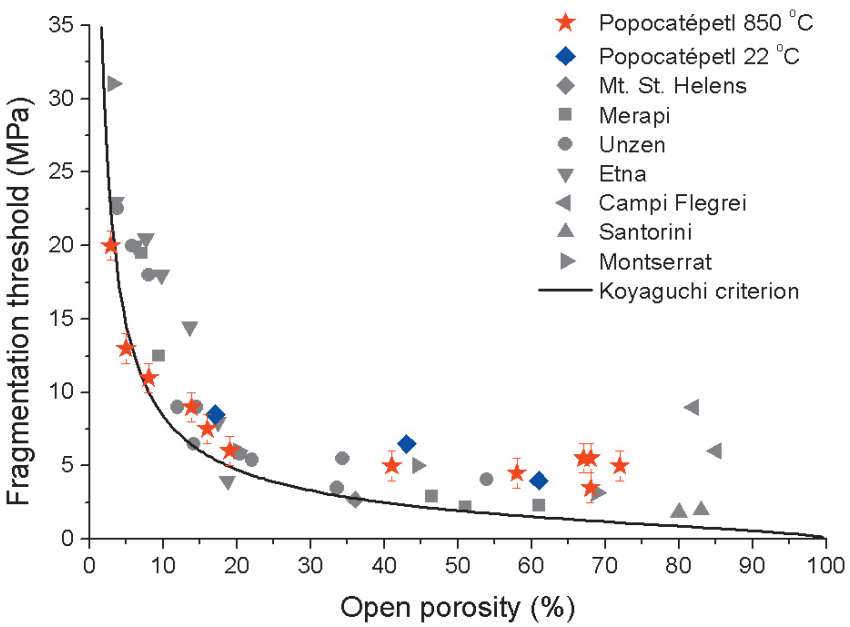

Figure 4. Fragmentation threshold measured for the different types of samples from Popocatépetl volcano at 850 °C and room temperature during rapid decompression experiments. The line corresponds to the fragmentation criterion (Eq. 1) proposed by Koyaguchi *et al*. (2008), assuming that the effective tensile strength of the material is 1.5 MPa. The data at 850 °C for DBm, DBg and Pu samples correspond to the data presented by Alatorre-Ibargüengoitia *et al*. (2010). Experimental data corresponding to samples from a variety of volcanoes from Spieler *et al*. (2004) are also shown.

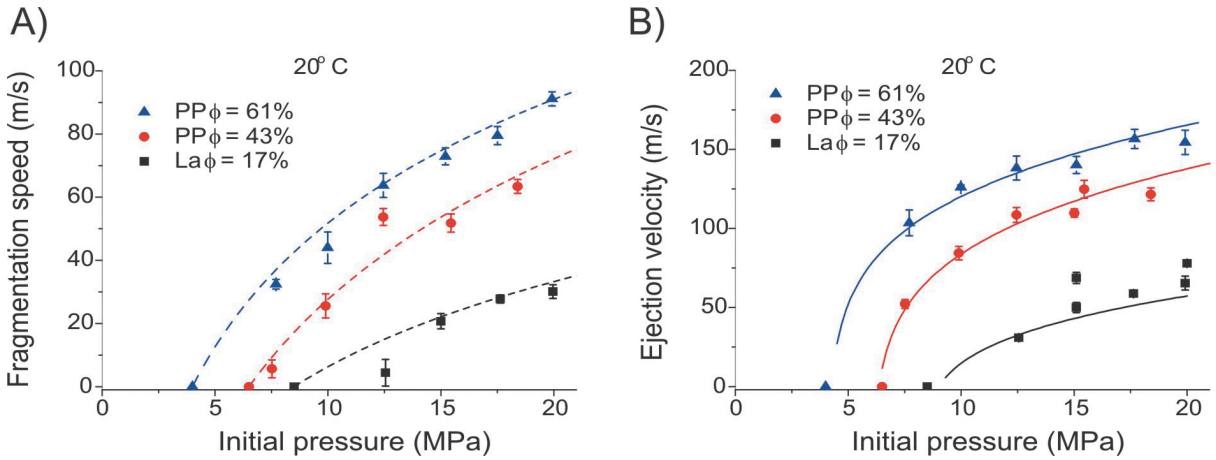

Figure 5. A) Fragmentation speed vs pressure at room temperature with Popocatépetl samples. Dashed lines represent the empirical fitting with eq. (2) considering kp= 38.9 m/s, kp = 64.2 m/s and kp = 56.5 m/s for samples with 17%, 43% and 61% porosity, respectively. Error bars of U data indicate the uncertainties in the determination of the fragmentation onset at the pressure drop curves. B) Ejection velocity of the front of the gas-particle mixture, calculated as the average of the velocities of several particles traveling at the front. Error bars represent the standard deviations. The velocities at 0 m/s indicate the fragmentation threshold of the samples at room temperature. The data in both plots for samples with 17% and 61% porosity correspond to the data presented by Alatorre-Ibargüengoitia et al. (2011). Solid lines correspond to the theoretical calculations for v_f using Eq. (3). For the calculations, we considered R =207.8 $JKg^{-1}K^{-1}$ and Cv =312 $JKg^{-1}K^{-1}$ for argon gas and Cs =1400 $JKg^{-1}K^{-1}$ (calculated with CONFLOW, Mastin and Ghiorso, 2000). The final pressure (P_{fi}) was estimated in the experiments according to the method described by Alatorre-Ibargüengoitia *et al*. (2010).

front (Alatorre-Ibargüengoitia *et al*., 2011). We observed that the ejection velocity of the gas–particle mixture increases non-linearly with applied pressure and it is higher than the fragmentation speed, as can be observed in Figure 5B. This figure also illustrates that the measured ejection velocities of the front of the gas-particle mixture is consistent with the theoretical model proposed by Alatorre-Ibargüengoitia *et al*. (2011) based on a 1-D shock-tube theory considering the conservation laws across the fragmentation front.

That model states that the fragmentation speed determines the initial conditions for the expansion of the gas-particle mixture considering the following assumptions (Koyaguchi and Mitani, 2005; Koyaguchi *et al*., 2008): (1) mass, momentum and energy are conserved across the fragmentation front; (2) the fragmentation front propagates at a constant speed; (3) the dynamics of the gas-particle mixture is described by the shock-tube theory for inviscid flow; (4) the gas-particle mixture behaves as a "pseudo-gas"; and (5) only particles smaller than a certain size (depending on the expansion time) remain in thermal equilibrium with the gas (Woods, 1995). From these assumptions, the ejection velocity of the front of the gas-particle mixture (v_f) can be expressed as follows (Alatorre-Ibargüengoitia *et al*., 2011):

$$v_f = a_{\_} - U + \frac{2\sqrt{n\gamma RT_o}}{\gamma - 1}\left(\frac{P_{\_}}{P_o}\right)^{\frac{\gamma-1}{2\gamma}}\left[1-\left(\frac{P_{fi}}{P_{\_}}\right)^{\frac{\gamma-1}{2\gamma}}\right] \quad (3)$$

where the subscripts "o" and "_" refer to parameters at the initial conditions and at the gas-particle mixture region just after fragmentation, respectively. T is temperature, R is the specific gas constant, P is pressure, n is the mass fraction of gas, γ is the specific heat capacity ratio of the mixture considering only the fraction of particles in thermal equilibrium with gas, $a_{\_}$ is the sound speed in the mixture after fragmentation and P_{fi} is the final pressure. These parameters can be calculated according to the following expressions (Alatorre-Ibargüengoitia *et al*., 2011):

$$n = \frac{1}{1 + \frac{RT\rho_p(1-\phi)}{P\phi}} \quad (4)$$

$$\gamma = 1 + \frac{nR}{C_v n + C_S (1-n) f} \quad (5)$$

$$P\_ = P_o \left(\frac{U}{a_o} \right)^{\frac{2\gamma}{\gamma+1}} \quad (6)$$

$$a\_ = \sqrt{\frac{\gamma}{nRT\_}} \frac{P\_}{\rho\_} \quad (7)$$

where ρ_p and $\rho\_$ are the density of the particles and the mixture after fragmentation, respectively, C_v is the specific heat capacity of the gas at constant volume, c_s is the magma specific heat capacity and f is the particles remain in thermal equilibrium with the gas during the expansion phase.

The time for thermal equilibrium between particles and gas scales as $\pi d^2/k_d$ where d is the diameter of the particles and k_d is the thermal diffusion coefficient, with typical value 10^{-6} m^2/s for magma (Woods, 1995). In our experiments, the duration of fragmentation and ejection of the gas–particle mixture up to the position observed with the high-speed camera is in the order of 5 ms, 10 ms and 20 ms for the experiments with 61%, 43% and 17% porosity, respectively. Accordingly, the fraction f of particles in thermal equilibrium with the gas was estimated by the fraction of particles smaller than ~0.09 mm, ~0.125 mm and ~0.18 mm, respectively. By sieving the collected particles, we obtained the f values of 2 ± 0.5 %, 3 ± 0.5 % and 5 ± 0.5 % respectively.

Due to experimental constraints and the dynamic pressure transducer´s temperature range, it is not possible to measure directly the fragmentation speed at magmatic temperatures using the same procedure as in the experiments up to moderate temperature. For this reason, the influence of the temperature on the fragmentation speed had not been investigated systematically. However, using the model of Alatorre-Ibargüengoitia *et al*. (2011) it is possible to estimate fragmentation speed values from the ejection velocity of the gas-particle mixture in experiments performed at magmatic temperatures. Figure 6a shows the measured ejection velocity of the front of the gas-particle mixture in experiments performed at 850°C with the same sets of samples as the experiments at room temperature (La with ϕ=16%, and PP with ϕ=41% and 58%). The corresponding fragmentation speed values estimated from the measured ejection velocities with the model of Alatorre-Ibargüengoitia *et al*. (2011) are presented in figure 6b. There is also a logarithmic relationship between the estimated fragmentation speed and the applied pressure (Eq. 2). The values estimated for the PP samples with ϕ=41% and 58% are similar at 850°C and at room temperature, whereas

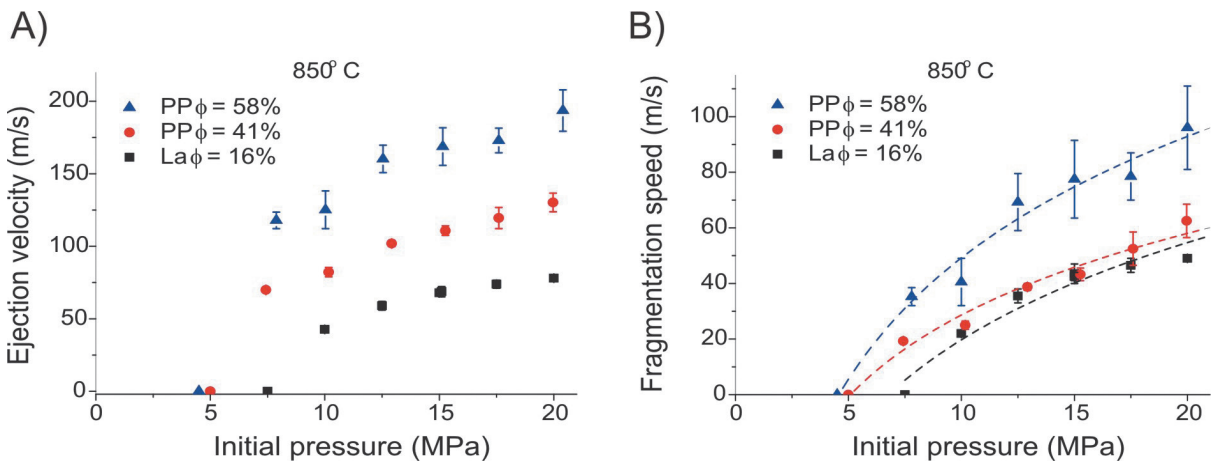

Figure 6. A) Ejection velocity of the front of the gas-particle mixture at 850°C, calculated as the average of the velocities of several particles traveling at the front. The error bars represent the standard deviations. The velocities at 0 m/s indicate the fragmentation threshold of the samples at 850°C. B) Fragmentation speed at 850°C estimated from the ejection velocity data using the model of Alatorre-Ibargüengoitia *et al*. (2011) considering the values mentioned in the caption of figure 5. The error bars indicate the uncertainties in the determination of the fragmentation speed due to the uncertainties associated with the ejection velocities. Dashed lines represent the empirical fitting with eq. (2) considering kp= 50.5 m/s, kp = 42.4 m/s and kp = 63.0 m/s for samples with 17%, 43% and 61% porosity, respectively.

the estimated values at 850°C corresponding to the La samples are considerable higher with respect to the measure data at room temperature (see Figure 5a).

It should be noted that the estimated values presented in Figure 6b depend on the fraction f of particles in thermal equilibrium with the gas. For the hot experiments, we made the same thermal consideration as for the cold experiments, and estimated f by the fraction of particles smaller than ~0.09 mm, ~0.125 mm and ~0.18 mm, respectively. By sieving the collected particles, we obtained that the corresponding f values are 1 ± 1 %, 1 ± 0.5 % and 5 ± 0.5 % for the experiments with 61%, 43% and 17% porosity, respectively. This topic, however, is still poorly understood. The estimated fragmentation speeds could change up to 30% depending on the considered value of f in Eq. (5). If a higher value of f is considered, the estimated fragmentation speed could be reduced and vice versa. Considering the limitations, the data presented in figure 6b represent, to our knowledge, the first experimental estimation of fragmentation speed values at magmatic temperatures.

Fragmentation efficiency

We analyzed the grain size distribution of the particles produced in experiments at 850°C with four sets of samples with different porosities from Popocatépetl (DBm with ϕ=14% and 20%; DBg with ϕ=14%; and PP with ϕ=58%) and at different applied pressures. In general, we observed: 1) unimodal non-Gaussian particle size distribution; 2) decreasing grain-size with increasing applied pressure; and 3) finer particles in the experiments with more porous samples (Figure 7).

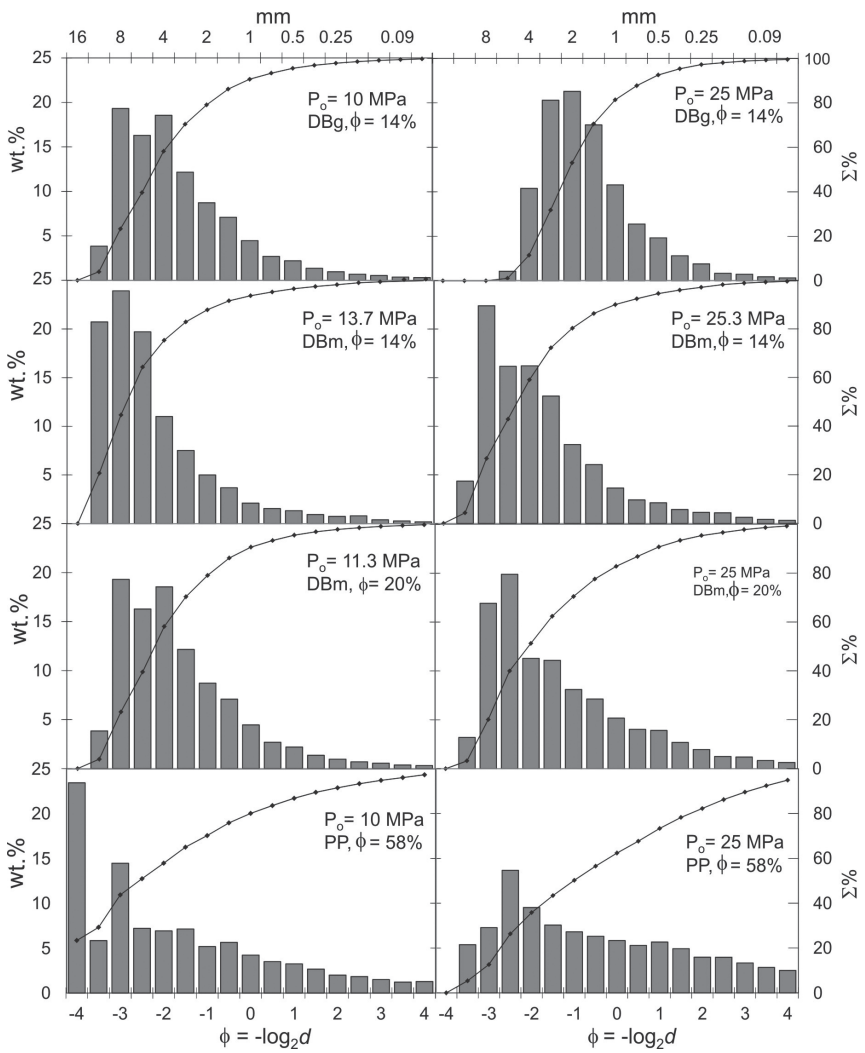

Figure 7. Examples of grain-size distribution plots showing the relation of wt.% and particle size of fragmentation experiments at 850 °C for the four different sets of samples (DBg with ϕ=14%; DBm with ϕ=14% and 20%; PP with ϕ=58%) at two different pressures. The grain size decreases to the right in each plot. The solid line with points shows the cumulative curve of the weight fractions (right axis). The plots in the right column represent experiments at higher pressures and clearly show a reduction of the grain-size of the particles with respect to the plots in the left column in all the cases.

Fractal fragmentation theory can be used to quantify the grain-size distribution of the experimentally generated particles (e.g. Korvin, 1992; Turcotte, 1997; Kueppers *et al*., 2006b; Perugini and Kueppers, 2012). According to this theory, the total number of particles with linear dimension greater than a given size *d* can be expressed as:

$$N(>d) = Cd^{-Df} \quad (8)$$

where D_f is the fragmentation fractal dimension and C is a constant. A similar rela-tionship relating mass measurements and sieve diameters can be expressed as follows (Turcotte, 1997):

$$M(<d) = M_t d_S^{-v} \quad (9)$$

where $M\ (<d_s)$ is the cumulative mass of particles smaller than the sieve size d_s, M_t is the total mass of particles and ν is a scaling exponent. It can be shown that (Turcotte, 1997):

$$D_f = 3 - v \quad (10)$$

This equation indicates that the fractal dimension of fragmentation (D_f) can be calculated using the exponent *v* from the mass-based approach, which is directly applicable to sieving data. Taking the logarithm of both sides of Eq. (8) and Eq. (10) yield linear relationships between Log [N (>*d*)] and Log (*d*), and between Log [$M\ (<d_s)$] and Log (d_s), where D_f and *v* are the slopes of the respective plots. Figure 8 shows some representative examples that clearly display a power-law behavior indicated by a very good linear trend (R^2> 0.99 for all cases) in the Log [$M\ (<d_s)$] vs. Log (d_s) plots. These linear trends extend over more than one order of magnitude showing that the fragmentation process can be analyzed in terms of the fractal fragmentation theory. The scaling exponent *v* was estimated for all the experiments from the slope of the linear fitting of these plots.

The values of D_f (and v) depend on the energy of the compressed gas stored in the pores at the moment of fragmentation in a unit volume of the sample (ρ_E). This energy density corresponds to the adiabatic work that

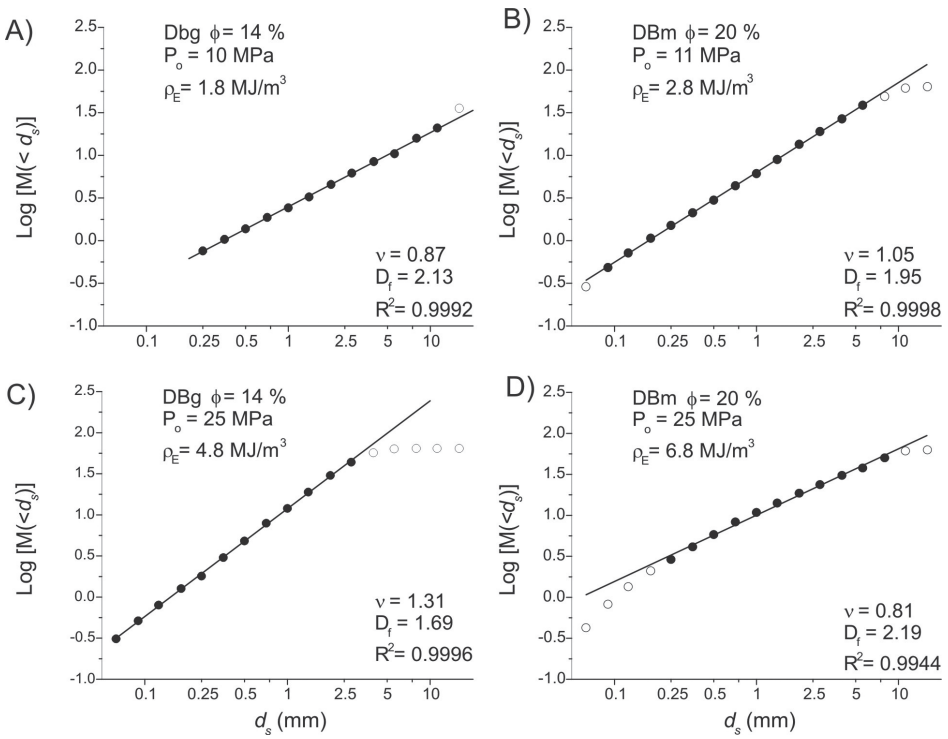

Figure 8. Representative log-log plots of particle size for Popocatépetl sample DBg with ϕ=14% (A-C, left column) and DBm with ϕ=20% (B-D, right column). Filled circles denote the data used for the linear fitting, whereas the open circles indicate the data that were not considered. The value of ν in each plot correspond to the slope of the linear fitting, whereas Df was calculated with Eq. (10). The experimental pressure (and the corresponding energy density) is higher in the plots at the bottom. Note logarithmic scale in the horizontal axis and that the scale is the same in all the plots.

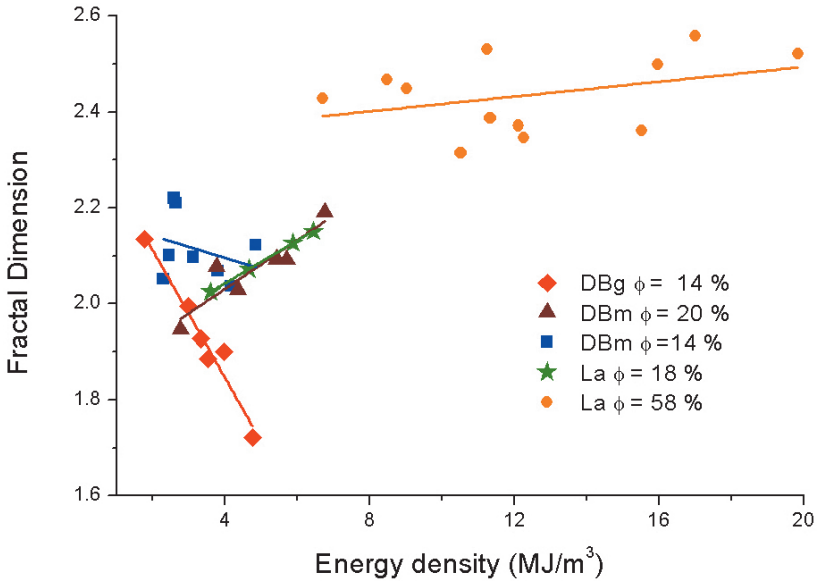

Figure 9. Fractal dimension as a function of energy density (Eq. 11) in fragmentation experiments with Popocatépetl samples. Some sets of samples show an increase in the fractal dimension with the energy density (DBm with ϕ=20%, PP with ϕ=58% and lava samples with ϕ=18%), whereas DBm with ϕ=14% show no clear trend and DBg with ϕ=14% show that Df decreases linearly as ρE increases. Data corresponding to lava samples are from Perugini and Kueppers (2012).

is done by the gas when the initial pressure P_o decreases to the ambient pressure P_a and it is given by (Alidibirov, 1994; Alatorre-Ibargüengoitia *et al*., 2010):

$$\rho_E = \frac{P_o \phi}{\gamma - 1}\left[1 - \left(\frac{P_a}{P_o}\right)^{\frac{\gamma-1}{\gamma}}\right] \qquad (11)$$

Figure 9 shows that the fractal dimension D_f varies with the energy density ρ_E in different ways depending on the rock sample: dense blocks DBm with ϕ=20% (Figure 3B) and pumice fragments PP with ϕ=58% (Figure 3D) show a linear increase of D_f as a function of ρ_E. This trend was also observed by Perugini and Kueppers (2012) with Popocatépetl lava samples with ϕ=20%. In the experiments performed with dense blocks DBm with ϕ=14% and with a microcrystalline matrix (Figure 3A) a clear trend is not produced, whereas the samples with a glassy matrix DBg with ϕ=14% (Figure 3C) show that D_f decreases linearly as ρ_E increases. It is worth noting that in the four sets of samples the same trend showed in figure 9 is observed if the fractal dimension is plotted against the PEF= $P_o \phi V_{cyl}$ (here V_{cyl} is the volume of the sample) as defined by Perugini and Kueppers (2012) instead of the energy density given by Eq. (11).

The trend observed with the samples DBg with ϕ=14% is interesting. As observed in figure 7, the grain size of the particles does decrease with increasing pressure, for instance the cumulative fraction of particles > 4 mm is significantly reduced at 25 MPa with respect to the experiment performed at 10 MPa. However, the range of sizes at which the fractal behavior applies decreases systematically: from d_s < 11.2 mm in the experiment at 10 MPa, to only particles with d_s < 2.8 mm in the experiment at 25 MPa (Figure 8). The difference between the trend observed for DBg and DBm samples can be related to the groundmass texture, which is glassy in the first case and microcrystalline in the second case. Further systematic experiments and analysis will be necessary to investigate the influence of both the groundmass texture and composition on the fractal behavior of the experimentally generated particles.

We further investigated the influence of secondary processes on the fractal dimension by using the products of the same sample at 850 °C in the following order: First, we performed fragmentation experiments with three cylindrical core samples with different porosity. Second, we performed rapid decompression experiments on the collected particles of each sample from the fragmentation experiments (without mixing them). Third, we repeated the decompression experiments with the collected

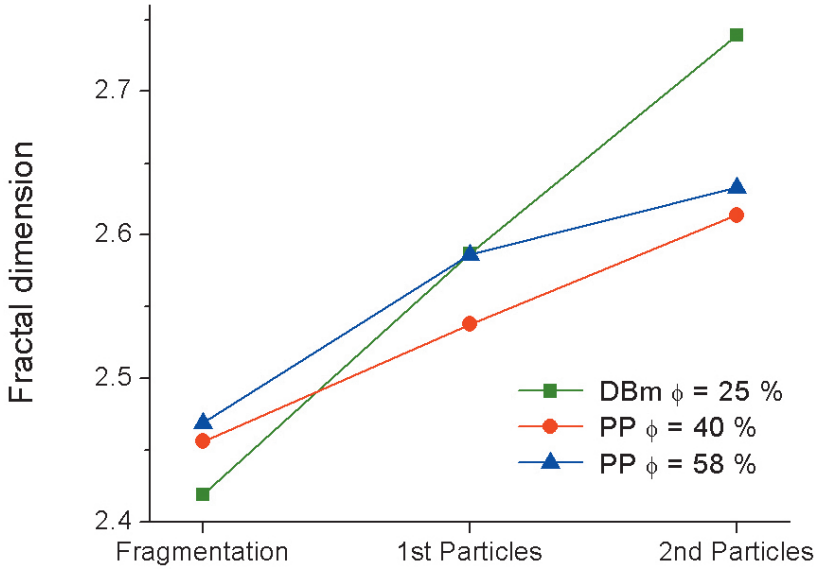

Figure 10. Fractal dimension of the grain-size distribution observed in the fragmentation of cylindrical core samples and rapid decompression experiments at 850 °C with the resulting particles with samples with three different porosities. The fractal dimension increase after a repeated experiment, reflecting possible secondary fragmentation of the particles after each experiment.

particles from the previous decompression step. We analyzed the resulting grain-size distribution after each experiment and observed than all the cases display a power-law behavior (i.e. a very good linear fit in the Log $[M(<d_s)]$ vs. Log(d_s) plot). Figure 10 shows that the fractal dimension D_f increases systematic after each step for the three samples, which may reflect secondary fragmentation processes of the particles in the repeated experiments.

Microsignals

In this section, we analyze the microsignals resulting from the elastic energy released during decompression and fragmentation, which travels through the sample and throughout the steel autoclave. From these signals, some information of the medium and of the behavior of the system can be deduced considering the distinct phases of the experiments, including pressurization, decompression, fragmentation and ejection of the gas-particle mixture (Arciniega-Ceballos *et al*., 2014; 2015). In previous studies, we analyzed the resonance characteristics of the fragmentation bomb and we showed that the resonance modes of the collection tank do not affect the signals of the high pressure autoclave (Arciniega-Ceballos *et al*., 2014). The core samples used in these experiments were from La with ϕ=15 % and PP with ϕ between 40 and 51% (table 1), all performed at room temperature and pressures between 8 and 13 MPa, using one and two diaphragms. The signals recorded with sensors named S4, S6 and S7 correspond with the radial component of motion: S7 coincides with the position of the sample in the autoclave, S4 is below the sample and S6 covers the cavity above the sample. The sensors S8 and S9 located at the bottom of the autoclave correspond to the vertical component of motion (Figure 1A).

Figures 11A and 11B show the superposition of raw signals recorded at sensors S8 and S7, respectively, for three experiments with only one diaphragm (which produces a simpler signal than with two diaphragms), pressures between 8 and 9 MPa and samples with porosities between 39 and 45%. Observe that the signals are coherent (marked with light blue in figures 11A and 11B), especially at low frequencies and in the vertical component (Figure 11B). This is clearer comparing the amplitude spectra of different experiments (shown in figures 12A and 12B). Note that the dominant frequencies are below 300 Hz; many spectral picks and maximum amplitudes coincide, even for experiments performed with two diaphragms. On the other hand, spectral pick coincidences for frequencies above 400 Hz are random (figures 12A and 12B). These spectral amplitudes are at least one half smaller than the amplitudes of lower frequencies amplitudes. The similarities between the signals and their spectra at low frequencies indicate that these experiments

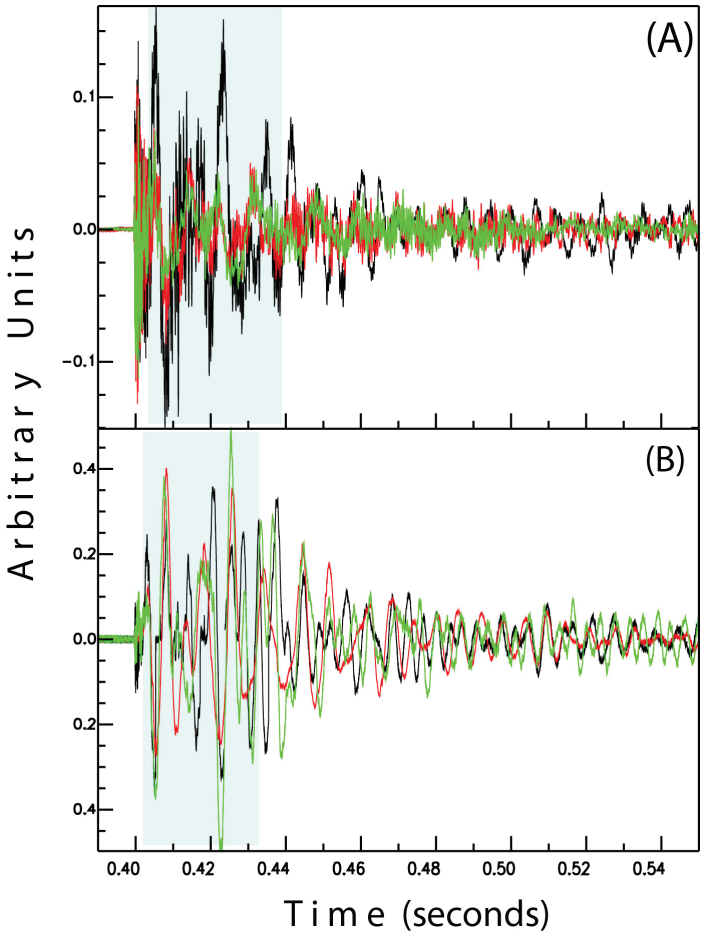

Figure 11. Superimposed time series of three different fragmentation experiments performed at 9, 8, and 8.2 MPa, indicated in black, red and green, respectively. A) Radial sensor S7. B) Vertical sensor S8. These experiments were performed using PP samples and only one diaphragm. Shadow blue areas indicate sections with waveforms coincidence. For better comparison, plots are at their original scale; x-axis is in seconds and y-axis in arbitrary units.

share a common mechanism, which indeed they do. Thereby, the processes triggered by decompression causing the fragmentation of the samples might be correlated with the high frequency content.

To differentiate the distribution of the elastic energy, in frequency and time, and correlated it with the occurrence of the physical processes inside the autoclave, we filtered the records conserving their waveform characteristics (Figures 13A and 13B) and calculate spectrograms for different samples (Figures 14A and 14B). Figures 13A and 13B display vertical and radial signals filtered in three frequency bands: low frequencies (< 800 Hz), middle frequencies (between 800 and 2000 Hz) and high frequencies (> 2000 Hz). Different events might be extracted from each frequency band: diaphragm(s) aperture, gas expansion, layer by layer fragmentation of the sample, and ejecta of the gas-particles mixture, including particle interaction. However, in order to validate our interpretation we need to demonstrate it using transparent autoclaves.

From the spectral characteristics, we can distinguish the response of the system comparing the spectrograms of two experiments: one performed only with gas at 8.1 MPa (no fragmentation) and the second corresponding to the fragmentation of a core sample at 8.9 MPa (Figures 14A and 14B). Note that both spectrograms present similar structures, with variations in the excitation modes along the spectrum and different breaking process of the diaphragm(s). The later can be identified at the beginning of the record due to their high frequency content (Figures 14A and 14B). These observations are in agreement with the distribution of the elastic energy in terms of frequency, waveform expressions and the occurrence of the physical processes inside the autoclave.

Maximum amplitudes were consistently recorded at the vertical component (e.g. Figures 13A and 13B). The sensor S8 captured the counterforce related to the decompression of the sample and the force at the base of the diaphragm at the time when it opens, as well as with the driving force associated with

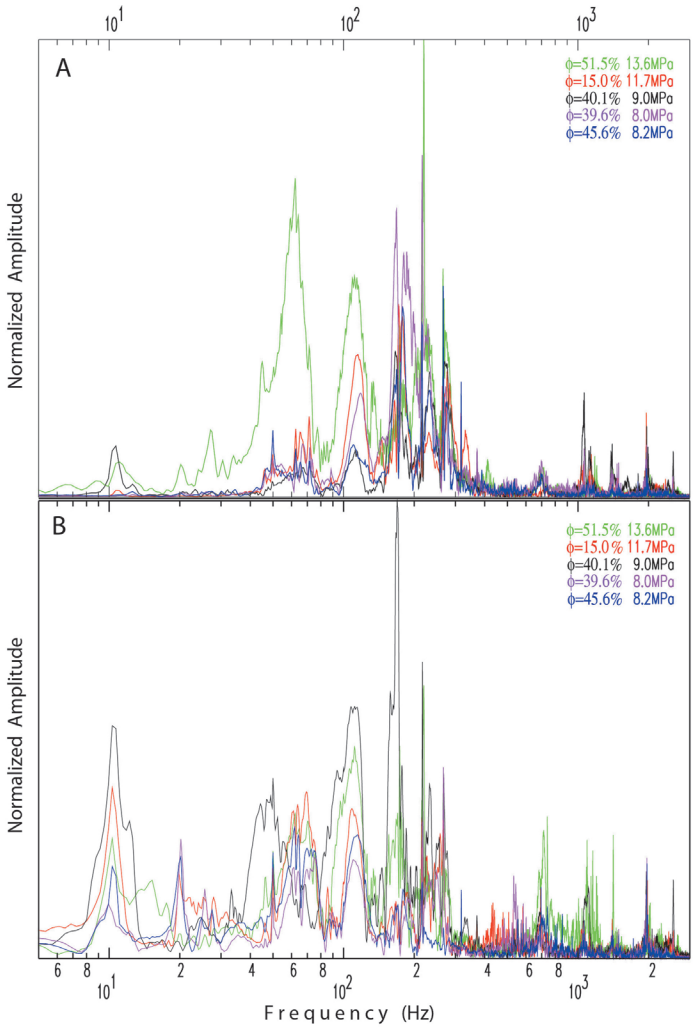

Figure 12. Amplitude spectra of five fragmentation experiments; (A) signals recorded at the bottom of the autoclave, sensor S8. B) Signals recorded at the wall of the autoclave, sensor S7. Porosity and pressure are indicated at the right upper corner of each panel with the same color as the corresponding spectrum. For comparison, each spectrum is normalized with respect to its maximum and plotted vs frequency in logarithm scale. Spectra in red and green correspond to experiments performed with two diaphragms, whereas the rest of the colors indicate only one diaphragm. For details about the samples see Table 1. Common picks at frequencies < 300 Hz reflect the common mechanism, while higher frequencies are associated with sample characteristics and fragmentation process.

the ejection of the bulk mass. Comparing the amplitudes, we observe that the vertical component S8 is about twice the amplitudes in the radial sensor S7, which is in agreement with the cylindrical geometry (Arciniega-Ceballos *et al*., 2014; 2015). Although intuitively higher amplitudes at higher pressures are expected, the maximum amplitudes are, however, also a function of the porosity and permeability of the sample, and they depend also on the fragmentation dynamics (at the time of these experiments we could not see inside the autoclave to evaluate this effect). Even when it is difficult to deduce how the rock was fragmented, we observe that maximum amplitudes do not necessarily coincide with maximum pressure. We also calculate the vertical and radial forces associated with each sample following Arciniega-Ceballos *et al*. (2014). We found that there is a trend of the force with respect to the sample porosity (Figure 15A). Figure 15B shows that the forces are distributed along the autoclave increasing from top (sensor 6) to bottom (sensor 8). The sample and autoclave are subjected to the major stresses at the bottom. The trend indicates that porosity and density of the sample affect the maximum force involved in the fragmentation of the sample more than the applied pressure.

The observed characteristics in time and frequency indicate that more energy is released in the low frequency band (below 300 Hz) and the spectral similarities among different experiments confirm common mechanisms such as the gas expansion and the response of the autoclave. Higher frequencies might be associated with the particularities of each experiment, like the manner of how each sample is fragmented as well as the particle interaction involved (see Figures 13A and 13B). For future experiments, we shall consider the use of transparent autoclaves where the evolution of the fragmentation process inside

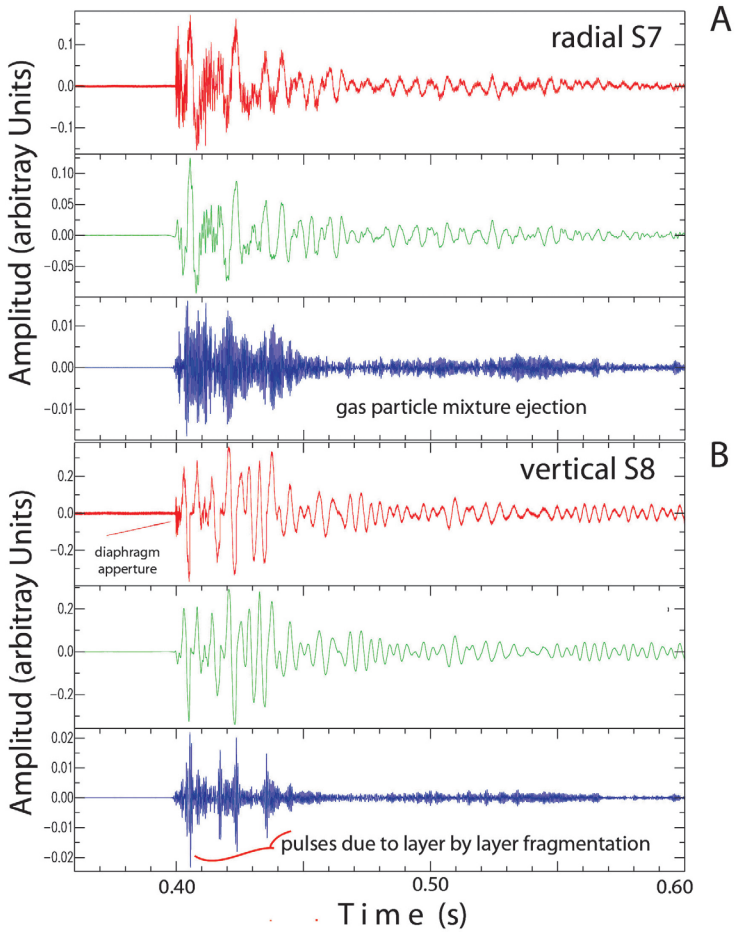

Figure 13. Waveform signals from: A) radial (S7); and B) vertical (S8) sensors. These signals were filtered in three frequencies bands: in red low frequencies < 800 Hz; in green frequencies between 800 and 2000 Hz; and in blue high frequencies > 2000 Hz. For better comparison, plots are at their original scale; x-axis is in seconds and y-axis in arbitrary units. Data are from an experiment at 9.0 MPa, using a PP sample with ϕ=40% and one diaphragm. For interpretation some events are indicated on the plots, see text for major details.

the conduit can be filmed in order to correlate directly the processes that occur before and during the ejection with their associated elasto-acoustic signatures (Arciniega-Ceballos *et al*., 2015; 2016).

Discussion

The applicability of shock-tube experiments to volcanic eruptions has been discussed by Koyaguchi and Mitani (2005). They suggested that the results of shock-tube experiments can be applied to natural volcanic systems for magmas with viscosities higher than 10^7 Pa s, in which case bubble expansion is negligible and brittle fragmentation occurs. It is worth noting that our experiments correspond solely to magmatic fragmentation, i.e. that fragmentation does not occur as a result of the interaction of magma with external water.

Our results may have important implications for understanding the mechanism of initiation and cessation of volcanic eruptions at Popocatépetl. The threshold data can be used to estimate how much overpressure is required to initiate explosive fragmentation of magma with a given porosity (Spieler *et al*., 2004). The porosity of dense ballistic blocks collected in the field range from 3-25 % and their corresponding fragmentation threshold determined experimentally are between 20 and 6 MPa, respectively. Pumice fragments corresponding to the 2001 pyroclastic flow deposit have porosities between 55 and 80 %, and their corresponding fragmentation threshold is between 3.5 and 5.5 MPa. Overall, the fragmentation threshold measured for the different types of samples from Popocatépetl is inversely related to the porosity and can be modeled with the fragmentation criterion proposed by Koyaguchi *et al*. (2008), with an effective tensile strength of 1.5 MPa. Considering Vulcanian eruptions, our threshold data can be used to estimate the amount of decompression needed to trigger magma fragmentation and produce an explosive eruption.

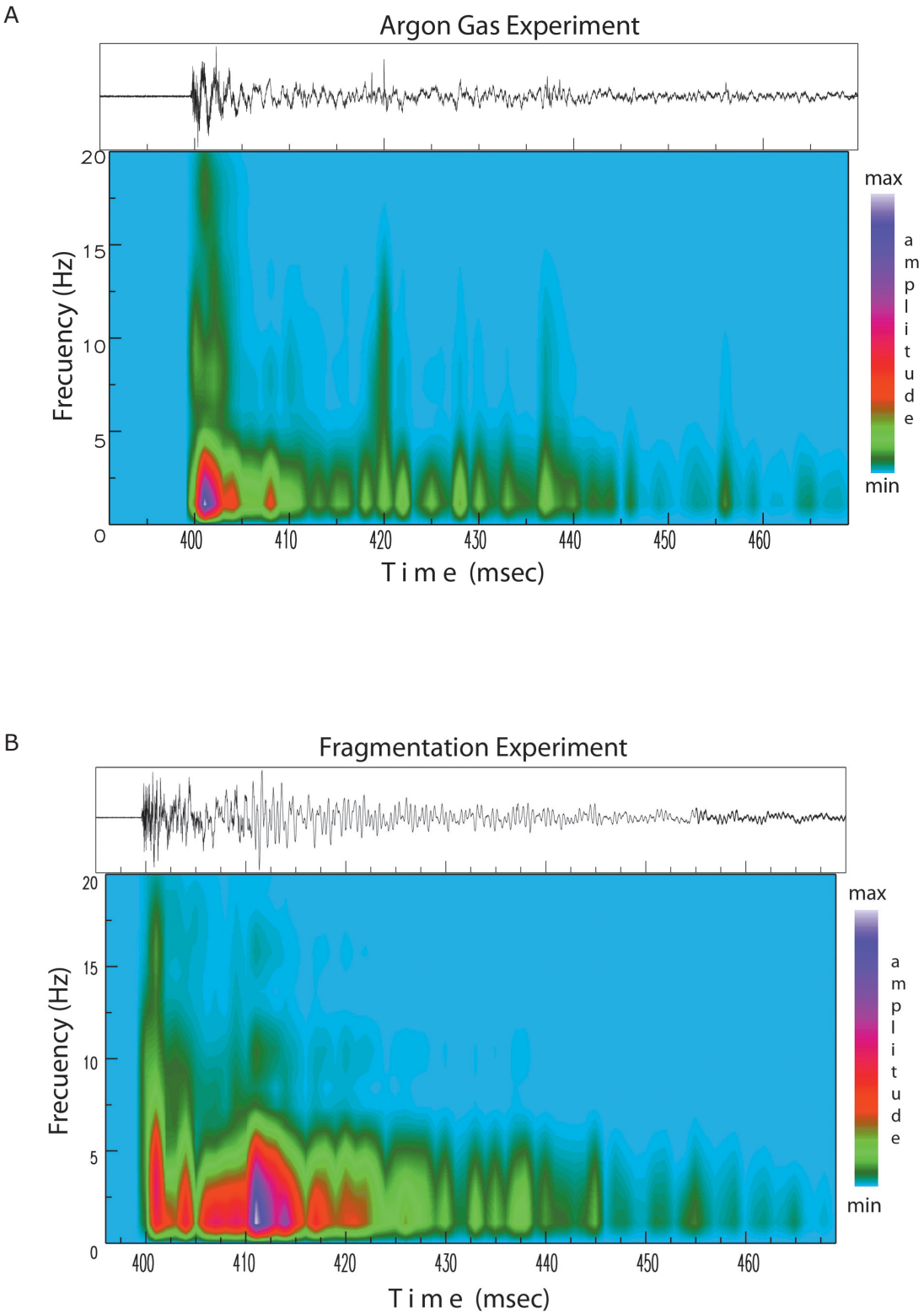

Figure 14. A) Spectrogram of the signal corresponding to the experiment performed at 8.1 MPa using only argon with one diaphragm. B) Spectrogram of the signal of the fragmentation experiment showed in figure 13A. The top panel of each spectrogram shows the corresponding time series recorded at sensor S7. Color bar indicates amplitude intensity at relative scale in arbitrary units; x-axis is in milliseconds and y-axis is in Hz.

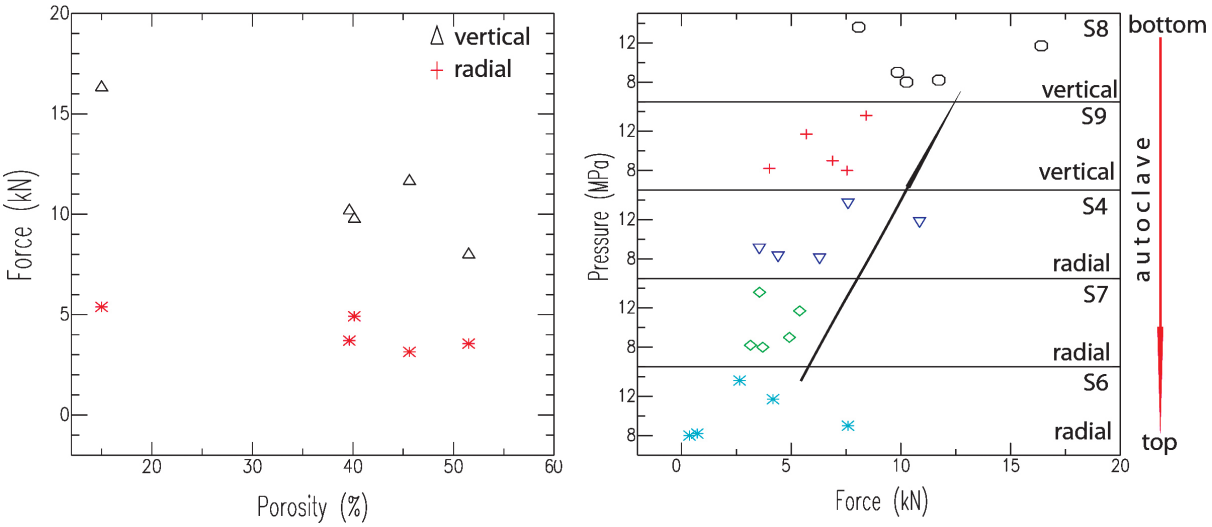

Figure 15. A) Vertical force from sensor S8 (black triangles) and radial force from sensor S7 (red asterisks) vs porosity. B) The force distribution along the mechanism of the autoclave is shown considering the sensors' location; from the top of the sample to the bottom of the autoclave (red arrow) (see Fig. 1). The forces of each experiment are plotted by sensor vs pressure; radial sensors S6, S7, S4, are in cyan, green and blue, respectively. Vertical sensors S8 and S9 are in black and red, respectively. Note in A) that the force decreases as porosity increases, whereas in B) the force increases from top to bottom (indicated by the black arrow). Vertical forces are about twice the radial forces as in Arciniega-Ceballos *et al*. (2015).

Moreover, the fragmentation threshold data can be used to estimate the energy consumed by the fragmentation process and calculate the effective pressure available to eject the ballistic projectiles (Alatorre-Ibargüengoitia *et al*., 2010). This pressure serves as an input parameter for eruptive models, which in concert with ballistic models, can correlate the ballistic range with gas content and initial gas pressure. With this approach, the probability that certain areas can be affected by volcanic ballistic projectiles during Vulcanian eruptions will be linked with data from volcano monitoring, providing the basis for short-term hazard assessment (Alatorre-Ibargüengoitia *et al*., 2012).

The fragmentation speed is also a controlling factor for explosive scenarios. If the fragmentation speed is comparable to the ascent rate of the magma, a stable fragmentation front may be established leading to sustained Plinian eruption. However, if the fragmentation front travels through magma with decreasing porosity, the fragmentation speed will diminish and the fragmentation level will rise (Scheu *et al*., 2006). The magma will cease to erupt if the pressure differential falls below the fragmentation threshold, either because the fragmentation front reaches low porosity magma, or the pressure differential decreases during the eruption (Spieler *et al*., 2004). Furthermore, Alatorre-Ibargüengoitia *et al*. (2011) proposed that the fragmentation speed determines the initial conditions of the expansion of the gas–particle mixture and it is a controlling factor on the velocity, density and mass discharge rate of the gas–particle mixture. All these factors can affect the eruption dynamics significantly. The data presented here represent, to our knowledge, the first experimental estimates of the fragmentation speed at magmatic temperatures (850 °C) and can be used as input parameters for eruptive models.

Fractal fragmentation theory provides the basis for comparing the grain-size distribution generated in the fragmentation experiments with the grain-size distribution of natural deposits. Linares (2001) collected a total of sixty ash fall samples corresponding to several eruptive events of Popocatépetl between 1995 and 1998 in areas of 1 m^2 at several locations at distances between 1 and 56.6 km from the crater. He analyzed by sieving the grain-size distribution of each sample with sizes between 0.063 mm and 1 mm. Notably, we found that most of the collected samples follow a fractal distribution (Figure 16). The fragmentation fractal dimension (D_f) for each sample was calculated with Eq. (10) from the slope of the linear fitting v in each plot. Figure 17A shows the histogram of the D_f corresponding to the

ash fall deposits, which ranges from 1.4 to 3.0, with mode 2.7 and median 2.4. There is no correlation between the fragmentation fractal dimension with crater distance in the analyzed events (Figure 17B).

In our fragmentation experiments, the fractal distribution ranges between 1.7 and 2.5 at pressures up to 20 MPa and the observed trends suggest that very high pressures would be required to produce fractal dimensions higher than 2.6. Therefore, it is likely that the higher fractal dimensions observed for some of the ash samples may reflect selective secondary fragmentation processes that tend to reduce the grain-size of the pyroclasts and increase the fractal dimension. In fact, our decompression experiments with fragmented particles show that the fractal dimension increases after each new experiment. Kaminski and Jaupart (1998) showed that, at fragmentation, the amount of continuous gas phase is an increasing function of the D_f value because the smaller the particles, more bubbles are disrupted and

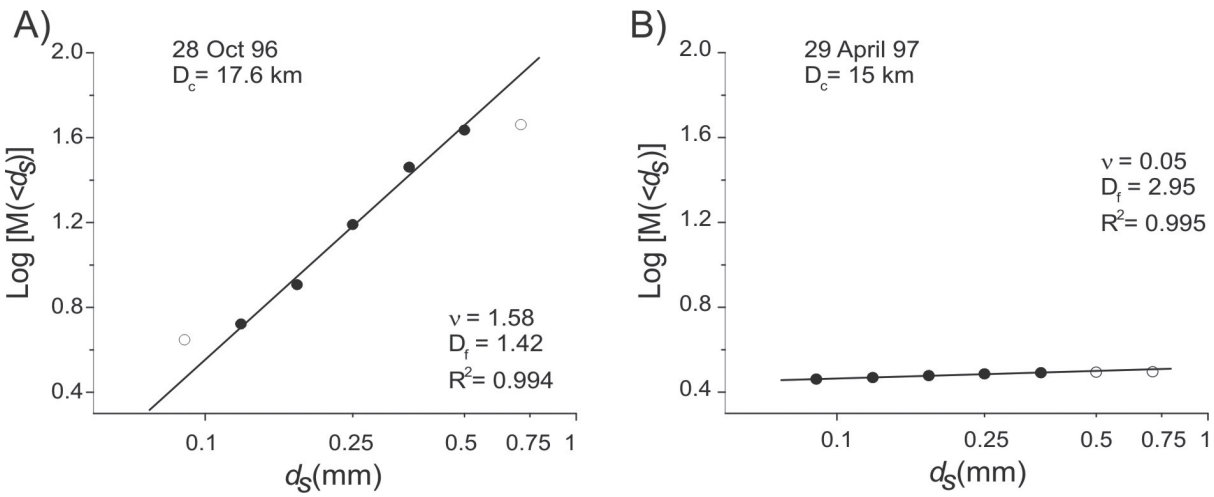

Figure 16. Representative log-log plots of particle size for ash samples ejected during two different events of Popocatépetl. Note logarithmic scale in the horizontal axis and that the scale is the same in both the plots. D_c represents the distance to the crater of the sampling site. Filled circles denote the data used for the linear fitting, whereas the open circles indicate the data that were not considered. The value of ν in each plot correspond to the slope of the linear fitting, whereas D_f was calculated with Eq. (10).

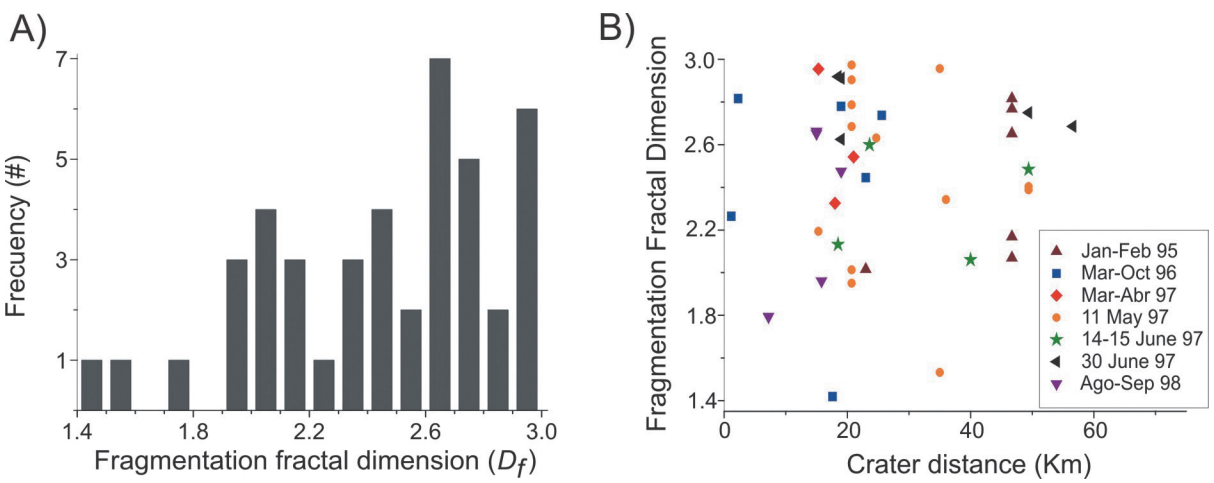

Figure 17. A) Histogram of the fragmentation fractal dimension (D_f) corresponding to 60 ash fall deposits from several eruptive events of Popocatépetl between 1995 and 1998. B) D_f from these ash fall deposits as a function of crater distance.

therefore the gas release is enhanced. This effect can considerably influence eruptive behavior above the vent.

The experiments of rock fragmentation provide a unique approach to distinguish the processes involved in the generation of seismic signals. The experiments performed at controlled conditions in the shock-tube apparatus with a well-known geometry provide information about the distribution of energy during fast decompression. Important information about the processes involved are retrieved from the distinct waveform signals of the time series recorded with the set of piezoelectric sensors (Arciniega *et al.,* 2015). Our experiments show that there are important differences in the spectral characteristics between the decompression of just pressurized gas with respect to the fragmentation of the samples. We noticed that the fragmentation process controls the frequency content of the records. The sample porosity affects the maximum amplitudes of the recorded signals and the maximum force involved in the fragmentation of the sample more than the applied pressure. The coherence observed in the elasto-acoustic signals at lower frequencies suggests bulk mass motion due to the gas expansion, the fragmentation of the sample and the ejection of the particles. The frequency and time characteristics observed in the elasto-acoustic signals associated with the different processes of the experimental explosions may contribute to the interpretation of seismograms related to Vulcanian eruptions (Arciniega-Ceballos *et al*., 2014; 2015). Future investigations would benefit from an increased coupling of experimental results with geophysical data (seismic, infrasound and ground deformation), Doppler radar measurements during Vulcanian eruptions (e.g. Scharff *et al*., 2015), high-speed observations (e.g. Taddeucci *et al*., 2017) and with numerical simulations considering unsteady vent conditions (e.g. Ogden, 2011; Carcano *et al*., 2013; Clarke, 2013; Chojnicki *et al*., 2015).

Summary and conclusions

This study comprises experimental data of several parameters (threshold, fragmentation speed, efficiency, elastic signals) associated with the fragmentation behavior of different sets of samples from Popocatépetl, Mexico. Our results show a strong influence of the connected porosity of the rock and the applied pressure on the fragmentation process. The measured data of the fragmentation threshold are important because they provide a quantitative constraint on the overpressure required to generate an explosive event.

We also investigated quantitatively the fragmentation speed corresponding to the different sets of samples. We present the first experimental estimate of the fragmentation speed at magmatic temperatures (850 °C) calculated from the ejection velocities of the front of the gas-particle mixture after fragmentation using the model of Alatorre-Ibargüengoitia *et al*. (2011). According to this model, the fragmentation speed determines the initial conditions for the expansion of the gas–particle mixture, which in turn controls the velocity, density and mass discharge rate of the gas–particle mixture. These factors can affect the eruption dynamics significantly.

We observed that the grain-size distribution of experimentally generated pyroclasts is consistent with fractal fragmentation theory. We found that the fractal dimension of fragmentation shows a positive linear correlation with the energy (applied pressure) for two sets of samples, no clear trend in one different set of sample and a negative correlation in another set of samples with different groundmass texture. These results indicate that not only the rock porosity and the applied pressure control the fractal dimension, but also the groundmass texture and composition may play an important role in the grain-size distribution. Ash samples collected for several Vulcanian eruptions of Popocatépetl also present a fractal behavior, but in general with higher D_f values, which suggest the occurrence of secondary fragmentation processes that increase the fractal dimension.

Our results shown that the waveforms and the spectral characteristics depend on the experiment type (decompression of pure gas vs fragmentation of a rock sample) revealing the influence of the fragmentation processes. In fact, our experiments suggest that the fragmentation process affects the frequency content. We also observed that the sample porosity has an effect on the maximum amplitudes of the signals and their associated maximum force. The experimental data and observations presented here contribute to a better understanding of magmatic fragmentation of rocks from Popocatépetl and thereby improve the interpretation of monitoring data and calibration of eruptive models for Vulcanian eruptions at intermediate composition volcanoes.

Acknowledgments

The authors wish to express their gratitude to (in alphabetic order) Jerónimo Alatorre, Miguel Alatorre-Mendieta, Corrado Cimarelli, Isaac Farraz-Montes, Carlos Fernández, Patricia

Jácome-Paz, Patricia Julio-Miranda, Ulrich Kueppers, Yan Lavallée, and Eric Téllez for field assistance. Financial support to the first author was provided by the IDK 31 THESIS program funded by the Elite Network of Bavaria (ENB). A Arciniega thanks Alexander von Humboldt Foundation and Mexican projects UNAM-DGAPA-PAPIIT IN106111 and IN105716. D. B. Dingwell acknowledges the support of a Research Professorship (LMUexcellent) of the Bundesexzellenzinitiative and the European Research Council (ERC) Advanced Grant EVOKES (247076). This study was partially funded by the FONCICYT program (Mexican Government-European Union), grant 93645 (FIEL-VOLCAN). Constructive reviews by two anonymous colleagues contributed to improve the manuscript.

References

Alatorre-Ibargüengoitia M.A., Scheu B., Dingwell D.B., Delgado-Granados H., and Taddeucci J., 2010, Energy consumption by magmatic fragmentation and pyroclast ejection during Vulcanian eruptions. *Earth Planet. Sci. Lett.,* 291, 60-69. doi:10.1016/j.epsl.2009.12.051

Alatorre-Ibargüengoitia M.A., Scheu B., Dingwell D.B., 2011, Influence of the fragmentation process on the dynamics of Vulcanian eruptions: An experimental approach. *Earth Planet. Sci. Lett.*, 302, 51-59. doi:10.1016/j.epsl.2010.11.045

Alatorre-Ibargüengoitia M.A., Delgado-Granados H., Dingwell D.B., 2012, Hazard map for volcanic ballistic impacts at Popocatépetl volcano (Mexico). *Bull. Volcanol.,* 74, 2155–2169. http://dx.doi.org/10.1007/s00445-012-0657-2.

Alidibirov M., 1994, A model for viscous magma fragmentation during volcanic blast. *Bull. Volcanol*., 56, 459-465.

Alidibirov M. and Dingwell D.B., 1996a, Magma fragmentation by rapid decompression. *Nature*, 380, 146-148.

Alidibirov M. and Dingwell D.B., 1996b, An experimental facility for the investigation of magma fragmentation by rapid decompression. *Bull. Volcanol.,* 58, 411-416.

Alidibirov M., and Dingwell D.B., 2000, Three fragmentation mechanism for highly viscous magma under rapid decompression. *J. Volcanol. Geotherm. Res*., 100, 413-421.

Arámbula-Mendoza R., Valdés-González C., Martínez Bringas A., 2010, Temporal and spatial variation of the stress state of Popocatépetl Volcano, Mexico. *J. Volcanol. Geotherm. Res.,* 196, 156-168.

Arana-Salinas L., Siebe C., Macías J.L., 2010, Dynamics of the ca. 4,965 yr. B.P. "Ochre Pumice" Plinian eruption of Popocatépetl Volcano, México. *J. Volcanol. Geotherm. Res.*, 192, 212–231. doi.org/10.1016/j.jvolgeores.2010.02.022.

Arciniega-Ceballos A., Valdés-González C., Dawson P., 2000, Temporal and spectral characteristics of seismicity observed at Popocatépetl Volcano, central Mexico. *J. Volcanol. Geotherm. Res.*, 102, 207-216.

Arciniega-Ceballos A., Chouet B., Dawson P., Asch G., 2008, Broadband seismic measurements of degassing activity associated with lava effusion at Popocatépetl Volcano, Mexico. *J. Volcanol. Geotherm. Res*., 170, 12-23.

Arciniega-Ceballos A., Alatorre-Ibargüengoitia M., Scheu B., Dingwell D.B. and Delgado-Granados H., 2014, Seismological analysis of conduit dynamics in fragmentation experiments. *J. Geophys. Res. Solid Earth*, 119, 2215-2229. doi:10.1002/2013JB010646.

Arciniega−Ceballos A., Alatorre−Ibargüengoitia M., Scheu B., and Dingwell D., 2015, Analysis of source characteristics of experimental gas burst and fragmentation explosions generated by rapid decompression of volcanic rocks. *J. Geophys. Res. Solid Earth*, 120, 5104–5116. doi: 10.1002/2014jb011810.

Arciniega-Ceballos A., Spina L., Scheu B., and Dingwell D.B., 2016, Multiscale Behavior of Viscous Fluids Dynamics: Experimental Observations. *Geophysical Research Abstracts*, 18, Vol. 18, EGU2016-10344.

Armienta M.A., Varley N., Ramos E., 2002, Radon and chemical monitoring at Popocatépetl volcano. *Geofísica Internacional*, 41, 271-276.

Armienta M.A., De la Cruz-Reyna S., Gómez A., Ramos E., Ceniceros N., Cruz O., Aguayo A., Martínez A., 2008, Hydrogeochemical indicators of the Popocatépetl Volcano activity. J. Volcanol. Geotherm. Res., 170, 35-50.

Armienta M.A., De la Cruz-Reyna S., Soler A., Cruz O., Ceniceros N., Aguayo A., 2010, Chemistry of Ash-Leachates to Monitor Volcanic Activity: An application to Popocatépetl Volcano, central Mexico. *Applied Geochemistry*, 25, 1198-1205.

Boudal C., Robin C., 1989, Volcán Popocatépetl: recent eruptive history, and potential hazards and risks in future eruptions. In: Latter J.H. (ed.) Volcanic hazards. IAVCEI Proc. Volcanol., Springer, Berlin, p. 110– 128.

Cabral-Cano E., Correa-Mora F., Meertens C., 2008, Deformation of Popocatépetl Volcano using GPS: Regional geodynamic context and constraints on its magma chamber. *J. Volcanol. Geotherm. Res.*, 170, 24–34.

Capra L., Poblete M.A., Alvarado R., 2004, The 1997 and 2001 lahars of Popocatépetl volcano (Central Mexico), textural and sedimentological constraints on their origin and hazards. *J. Volcanol. Geotherm. Res*. 131, 351-369.

Carcano S., Bonaventura L., Esposti Ongaro T., and Neri A., 2013, A semi-implicit, second order accurate numerical model for multiphase underexpanded volcanic jets. *Geosci. Model Dev. Discuss.*, 6(1), 399–452. doi:10.5194/gmdd-6-399-2013.

CENAPRED, 2016. http://www.cenapred.gob.mx/es/Publicaciones/archivos/357-CARTELMAPASDEPELIGROSDELVOLCNPOPOCATPETL.PDF.

Chojnicki K.N., Clarke A.B., Phillips J.C., and Adrian R.J., 2015, The evolution of volcanic plume morphology in short-lived eruptions, Geology, 43(8), 707–710. doi:10.1130/G36642.1.

Cigala V., Kueppers U., Peña Fernández J. J., Taddeucci J., Sesterhenn J. and Dingwell D. B., 2017, The dynamics of volcanic jets: Temporal evolution of particles exit velocity from shock-tube experiments. *J. Geophys. Res. Solid Earth*, 122, doi:10.1002/2017JB014149.

Clarke A.B., 2013, Unsteady explosive activity: Vulcanian eruptions. In: Fagents, S.A. *et al*. (eds.) Modeling Volcanic Processes, the Physics and Mathematics of Volcanism, Cambridge Univ. Press, Cambridge, U. K., p. 129–152.

De la Cruz-Reyna S. and Tilling R., 2008, Scientific and public responses to the ongoing volcanic crisis at Popocatépetl Volcano, México: importance of an effective hazards warning system. *J. Volcanol. Geotherm. Res*., 170, 121–134.

De la Cruz-Reyna S., Yokoyama I., Martínez Bringas A., Ramos E., 2008, Precursory seismicity of the 1994 eruption of Popocatépetl Volcano, Central Mexico. *Bull. Volcanol.,* 70, 753–767.

De la Cruz-Reyna S., Tilling R., Valdés-González C., 2017, Challenges in responding to a sustained, continuing volcanic crisis: the case of Popocatepétl volcano, Mexico, 1994-present. In: Bird D., Jolly G., Haynes K., McGuire B., Fearnley C (Eds.) Volcanic crisis communication - observing the volcano world. *Advances in Volcanology series*, Springer-Verlag. doi:10.1007/11157_2016_37.

Delgado-Granados H., Cárdenas González L. and Piedad Sánchez N., 2001. Sulfur dioxide emissions from Popocatépetl volcano (Mexico), case study of a high-emission rate, passively degassing erupting volcano. *J. Volcanol. Geotherm. Res.,* 108, 107-120.

Espíndola J.M., Godinez M.L., Espíndola V.H., 2004, Models of Ground Deformation and Eruption Magnitude from a Deep Source at Popocatépetl Volcano, Central Mexico. *Natural Hazards*, 31, 191–207.

Fowler A.C., Scheu B., Lee W.T. and McGuinness, M.J., 2010, A theoretical model of the explosive fragmentation of vesicular magma. *Proc. R. Soc. A.*, 466 (2115) 731-752. doi:10.1098/rspa.2009.0382.

Fowler A.C. and Scheu B. 2016. A theoretical explanation of grain size distributions in explosive rock fragmentation. *Proc. R. Soc. A.*, 472 *(*2190*) 20150843.* doi: 10.1098/rspa.2015.0843.

Gómez-Vazquez A., De la Cruz-Reyna S. and Mendoza-Rosas A.T., 2016, The ongoing dome emplacement and destruction cyclic process at Popocatépetl volcano, Central Mexico. *Bull. Volcanol.* 78, 58. DOI 10.1007/s00445-016-1054-z

Julio-Miranda P., González-Huesca A.E., Delgado Granados H., Kääb A., 2005, Glacier melting formation during January 22 2001, eruption, Popocatépetl volcano (Mexico). *Z. Geomorphol.,* 140, 95–102.

Julio-Miranda P., Delgado Granados H., Huggel C., Kääb A., 2008, Impact of the eruptive

activity on glacier evolution at Popocatépetl volcano (México) during 1994–2001. *J Volcanol. Geotherm. Res.,* 170,86–98. doi:10.1016/j.jvolgeores.2007.09.011.

Kaminski E. and Jaupart. C., 1998, The size distribution of pyroclasts and the fragmentation sequence in explosive volcanic eruptions. *J. Geophys. Res.,* 103 (B12), 29759–29779.

Kavanagh J.L., Engwell S., and Martin. S., 2018, A review of analogue and numerical modelling in volcanology. Solid Earth Discuss. 9, 531-571 doi:10.5194/se-2017-40.

Korvin, G. 1992. Fractal models in the Earth Sciences. Elsevier, Amsterdam, 396 pp.

Koyaguchi, T. and Mitani, N. K., 2005, A theoretical model for fragmentation of viscous bubbly magmas in shock tubes. *J. Geophys. Res.*, 110, B10202, doi:10.1029/2004JB003513.

Koyaguchi T., Scheu B., Mitani N. and Melnik O., 2008, A fragmentation criterion for highly viscous bubbly magmas estimated from shock tube experiments. *J. Volcanol. Geotherm. Res.,* 178, 58-71.

Kremers S., Scheu B., Cordonnier B., Spieler O. and Dingwell D.B., 2010, Influence of decompression rate on fragmentation processes: An experimental study. *J. Volcanol. Geotherm. Res.,* 193, 182-188.

Kueppers U., Scheu B., Spieler O. and Dingwell D.B., 2006a, Fragmentation efficiency of explosive volcanic eruptions: A study of experimentally generated pyroclasts. *J. Volcanol. Geotherm. Res.,* 153, 125-135.

Kueppers U., Perugini D. and Dingwell D.B., 2006b, "Explosive Energy" during volcanic eruptions from fractal analysis of pyroclasts. *Earth Planet. Sci. Lett.*, 248, 800–807.

Linares C. 2001. Estudios granulométricos en cenizas emitidas por el volcán Popocatépetl entre 1994 y 1998 (B.S. thesis): Mexico, Faculty of Engineering, Universidad Nacional Autónoma de México, México, 139 pp. (in Spanish).

Macías J.L. and Siebe C., 2005, Popocatépetl's crater filled to the brim: significance for hazard evaluation. *J. Volcanol. Geotherm. Res.,* 141,327–330.

Macias J.L., Carrasco G., Delgado H., Martin Del Pozzo A.L., Siebe C., 1995, Mapa de Peligros del Volcán Popocatépetl. IGF-UNAM, Mexico City.

Mader H.M., Manga M. and Koyaguchi T., 2004. The role of laboratory experiments in volcanology. *J. Volcanol. Geotherm. Res*., 129, 1-5.

Martin-Del Pozzo A.L., 2012, Precursors to eruptions of Popocatépetl Volcano, Mexico. *Geofis. Intl.* 51(1), 87–107.

Martín del Pozzo A.L., Cifuentes G., Cabral-Cano E., Bonifaz R., Correa F. and Mendiola I.F., 2003. Timing magma ascent at Popocatépetl Volcano, Mexico, 2000-2001. J. Volcanol. Geotherm. Res., 125, 107-120.

Martin-Del Pozzo A.L., Cifuentes G., Gonzalez E., Martínez A., Mendiola F., 2008, Magnetic signatures associated with magma ascent and stagnation at Popocatépetl Volcano, Mexico during 2006. *Geological Society of London Bull*., 304, 117-131.

Martin-Del Pozzo A.L., Rodríguez A. and Portocarrero J., 2016, Reconstructing 800 years of historical eruptive activity at Popocatépetl Volcano, Mexico. Bull. Volcanol., 78, 18. https://doi.org/10.1007/s00445-016-1010-y.

Mastin L.G., and Ghiorso M.S., 2000. A numerical program for steady-state flow of magma-gas mixtures through vertical eruptive conduits. U.S. Geol. Surv. Open-file Report, 00-209.

Mendoza-Rosas A.T., De la Cruz-Reyna S., 2008, A statistical method linking geological and historical eruption time series for volcanic hazard estimations: applications to active polygenetic volcanoes. J. Volcanol. Geotherm. Res., 176, 277–290.

Mendoza-Rosas, A.T., Gómez-Vázquez, Á., De la Cruz-Reyna, S., 2017, Statistical analysis of the sustained lava dome emplacement and destruction processes at Popocatépetl volcano, Central México. Bull. Volcanol., 79, 43. https://doi.org/10.1007/s00445-017-1127-7

Mueller S., Melnik O., Spieler O., Scheu B. and Dingwell, D.B., 2005, Permeability and degassing of dome lavas undergoing rapid decompression: an experimental determination. *Bull. Volcanol.,* 67, 526-538.

Mueller S., Scheu B., Spieler O. and Dingwell D., 2008, Permeability control on magma fragmentation. *Geology*, 36 (5), 399–402.

Novelo-Casanova D. and Valdes-Gonzalez C., 2008, Seismic pattern recognition techniques to predict large eruptions at the Popocatepetl volcano, Mexico. *J. Volcanol. Geotherm. Res.,* 176, 583-590.

Ogden, D., 2011, Fluid dynamics in explosive volcanic vents and craters, *Earth Planet. Sci. Lett.,* 312(3–4), 401–410, doi:10.1016/j.epsl.2011.10.032.

Perugini D. and Kueppers U., 2012, Fractal Analysis of Experimentally Generated Pyroclasts: A tool for Volcanic Hazard Assessment. *Acta Geophysica*, 60, 682-698. DOI: 10.2478/s11600-012-0019-7.

Richard D., Scheu B., Mueller S.P., Spieler O., and Dingwell D. B., 2013, Outgassing: Influence on speed of magma fragmentation, *J. Geophys. Res. Solid Earth*, 118, 862–877, doi:10.1002/jgrb.50080.

Scharff L., Hort M., and Varley N.R., 2015, Pulsed Vulcanian explosions: A characterization of eruption dynamics using Doppler radar. *Geology,* 43(11), 995–998. doi:10.1130/G36705.1.

Scheu B., Spieler O. and Dingwell D.B., 2006. Dynamics of explosive volcanism at Unzen volcano: an experimental contribution. *Bull. Volcanol*., 69, 175-187.

Scheu B., Ichihara M., Spieler O., Dingwell D.B., 2008b, A closer look at magmatic fragmentation. *Geophysical Research Abstracts*, 10, EGU2008-A-04786.

Siebe C. and Macías J.L., 2006, Volcanic hazards in the Mexico City metropolitan area from eruptions at Popocatépetl, Nevado de Toluca, and Jocotitlán stratovolcanoes and monogenetic scoria cones in the Sierra de Chichinautzin volcanic field. *Geol. S. Am. S.,* 402, 253–329. doi:10.1130/2004.VHITMC.PFG.

Siebe C., Abrams M., Macías J.L., Obenholzner J., 1996, Repeated volcanic disasters in Prehispanic time at Popocatépetl, Central Mexico: past key to the future? *Geology*, 24, 399– 402.

Siebe C., Salinas S., Arana-Salinas L., Macías J.L. Gardner J., Bonasia R., 2017, The ~23,500 yr 14 C BP White Pumice Plinian eruption and associated debris avalanche and Tochimilco lava flow of Popocatépetl volcano, México. *J. Volcanol. Geotherm. Res.,* 333, 66-95.

Smithsonian Institution, 2000, Popocatépetl. December set records in tremor, dome extrusion rates, SO2 flux, and tilt. *Bull. Glob. Volcanism Netw.,* 25, 12.

Smithsonian Institution, 2003, Popocatépetl. Cycles of dome growth and destruction; continuing activity. *Bull. Glob. Volcanism Netw*., 28, 2.

Sosa-Ceballos G., Gardner J., Siebe C., Macías J.L., 2012, A caldera-forming eruption ~14100 14C yr BP at Popocatépetl volcano, México. Insights from eruption dynamics and magma mixing. *J. Volcanol. Geotherm. Res.*, 213/214, 27–40. http://dx.doi.org/10.1016/j.volgeores.2011.11.001.

Spieler O., Kennedy B., Kueppers U., Dingwell D.B., Scheu B., and Taddeucci J., 2004, The fragmentation threshold of pyroclastic rocks. *Earth Planet. Sci. Lett.,* 226, 139-148.

Straub S.M. and Martin-Del Pozzo A.L., 2001, The significance of phenocryst diversity in tephra from recent eruptions at Popocatépetl volcano (central Mexico). *Contrib. Mineral. Petrol.,* 140, 487-510.

Taddeucci J., Alatorre-Ibargüengoitia M. A., Cruz-Vázquez O., Del Bello E., Scarlato P., and Ricci T., 2017, In-flight dynamics of volcanic ballistic projectiles. *Rev. Geophys.,* 55, 675–718, doi:10.1002/2017RG000564.

Turcotte D.L., 1997. Fractals and chaos in geology and geophysics. Cambridge University Press, United States, 398 pp.

Witter J.B., Kress V.C. and Newhall C.G., 2005, Volcán Popocatépetl, Mexico. Petrology, Magma Mixing, and Immediate Sources of Volatiles for the 1994-Present Eruption. *Jour. Petrol.,* 46 (11), 2337-2366.

Woods A.W., 1995, A model for Vulcanian explosions. *Nucl. Eng. Design*., 155, 345-357.

Wright R., De La Cruz-Reyna S., Harris A., Flynn L., Gomez-Palacios J.J., 2002, Infrared satellite monitoring at Popocatepétl: explosions, exhalations, and cycles of dome growth. *J. Geophys. Res.,* 107, 2–16.

Geofísica Internacional (2019) 58-1: 73-79

Original paper

A method for a rapid measurement of geostrophic currents in coastal waters: A bay case study

Anatoliy Filonov*, Diego A. Pantoja, Omar Mireles-Loera, Iryna Tereshchenko, Lydia Betty Ladah and Cesar Monzon

Received: January 17, 2018; accepted: September 20, 2018; published on line: January 18, 2019

Resumen

Mediante el método de CTD ondulante se calculan las corrientes geostróficas en un par de secciones paralelas cerca de la costa. Las componentes de la velocidad se estiman en cada cuadrilátero formado entre las secciones y las estaciones consecutivas. Con ésta metodología una campaña se puede realizar en tan solo 5 horas, si por ejemplo se considera un transecto de 20 km de longitud, con estaciones a cada 1 km y hasta una profundidad de 300 m. Para verificar esta metodología, se usaron datos de una campaña hidrográfica en Bahía de Banderas donde se tomaron hasta 120 perfiles en dos días de trabajo, con los cuales se realizó una malla regular con técnicas de mapeo objetivo de los campos hidrográficos que al final se compararon con las corrientes geostróficas calculadas mediante las rutinas GSW-TEOS10. La diferencia entre los resultados de la malla regular y las secciones paralelas resulto menor del 3.5%. En el presente estudio, la metodología se probó en una bahía, donde las corrientes observadas mostraron una estructura bien definida y persistente durante el muestreo, por lo que aplicar esta metodología en otras partes de la zona costera, por ejemplo en mar abierto, podría presentar más variabilidad en los resultados.

Palabras clave: Bahía de Banderas, CTD ondulante, Líneas Paralelas de hidrografía, Corrientes geostróficas.

Abstract

Geostrophic currents were computed using the method of fast thermohaline measurements from data obtained with an undulating CTD along two parallel transects in coastal waters. The method allows for the calculation of geostrophic currents in every quadrilateral set formed by each consecutive cast of the parallel hydrographic lines. With this methodology, it was possible to obtain very rapid data; for example, if the length of a section was 20 km, the distance between soundings was 1 km and the measuring depth was up to 300 meters, it would only take ~5 hours to complete the survey. Validation of the proposed method was carried out in Banderas Bay, México, where a very dense survey was taken; almost 120 casts were sampled over 2 days. With this sampling it was possible to construct a regular mesh where hydrographic data were objectively mapped and then the geostrophic currents were calculated in the traditional way using the GSW_TEOS10 toolbox. The root-mean-square deviation between both calculations was less than 3.5 %. In the case of the present study, the methodology was tested in a bay, where currents showed relatively stable patters that were persistent and well structured, suggesting this methodology may be applied to other sites, but caution is suggested in sites with large variability.

Key words: Banderas Bay, undulating CTD measurements, parallel hydrographic lines, geostrophic currents.

A. Filonov*
D. A. Pantoja
O. Mireles-Loera
I. Tereshchenko
C. Monzon
Universidad de Guadalajara
Blvd. Marcelino García Barragán #1421
Esq. Calzada Olímpica, C.P. 44430
Guadalajara, Jalisco, México

L. B. Ladah
CICESE, Carretera Ensenada Tijuana # 3918
Zona Playitas, Ensenada 22860
Baja California, Mexico
*Corresponding author: afilonov@prodigy.net.mx

Introduction

In oceanography, it is often necessary to compute geostrophic currents in deep bays or high seas. For this purpose, the data from oceanographic surveys are often collected at sea on vessels equipped with a winch to lower a CTD profiler. In order to measure the temperature and salinity profiles at a fixed point in the ocean, it is necessary to stop the ship and spend valuable time to lower and raise the probe on board the vessel. It takes tens of minutes to an hour or more to obtain every cast in each station depending on depth. In an earlier study (Filonov *et al*., 1996a), a simple method to take a fast oceanographic survey using an undulating CTD was proposed, which could be applied from an unequipped ship or marine boat such as a panga without a winch, shortening the data acquisition time by a factor of 3-5 and certainly reducing costs.

In coastal seas it is well-know that the calculation of geostrophic currents should be taken carefully due to the variability caused by many factors, especially internal waves (Defand, 1950). These waves can cause the hydrographic measurements on the continental shelf to be considerably different depending on the tidal phase in which they were taken. Therefore it is important to carry out a quick survey to capture the internal waves in the ocean and their nonlinear transformation, change of amplitude, direction of motion and spectral composition (Filonov, 2010). This method has been used in many papers (Filonov *et al*., 1996a; Filonov, 2000; Filonov *et al*., 2005; Filonov *et al*., 2014 and others). In this paper, we propose the use of the method of fast measurements to obtain the geostrophic currents in a coastal oceanographic transect which is composed of a forward and a backward parallel section.

Method of measurement

The survey is commonly performed along a line perpendicular to the coast. The thermohaline structure is captured using a towed autonomous undulating CTD, placed in a special box with a hydrodynamic shape (Figure 1), which can take rapid vertical profiles while mostly underway. When the vessel is at full speed, about 15-20 km/h, the CTD skimmed the surface, then when the boat stopped for the cast, the profiler fell freely, to a depth determined by the length

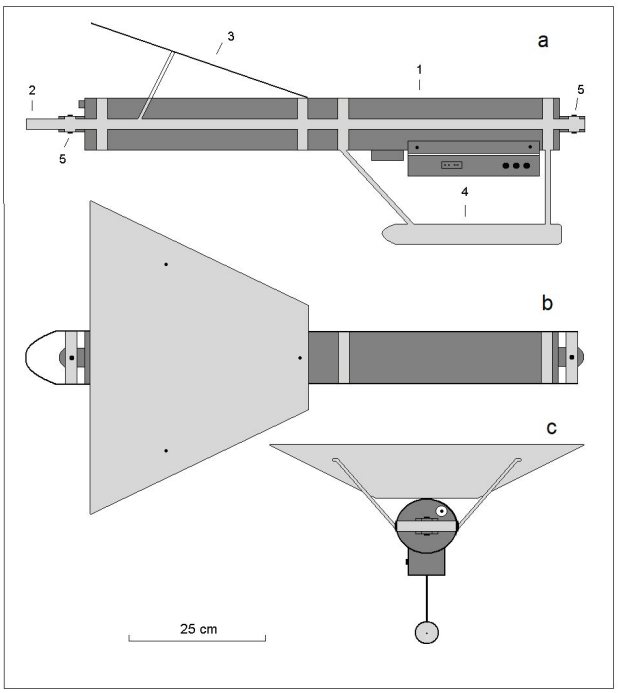

Figure 1. (a). Constructive scheme of an undulation CTD profiler (lateral view). Figures (b) and (c) show the plan and frontal views, respectively. The numbering means 1- CTD profiler SBE-19 plus or TDR XR-620. 2- The metal structure for fixing the profiler body. 3- A wing that generates lift during towing the vehicle. 4 - Directional keel to avoid rotation while towing. 5 - Bolts of fastening device to a metal structure.

of the tow rope. When resuming to full vessel speed, the CTD surfaced again till the next station, and so on (Filonov *et al*., 1996). The method requires two parallel sections with the most nearly uniform spatial distribution of vertical soundings in forward and backward directions. The distance between casts can be typically 1-2 km. The navigation data logged can be made by means of a GPS. The survey can be taken very quickly. For instance, a survey taken in Banderas bay (~ 60 km long and 30 km wide) lasted nearly two days to complete more than 120 casts. That is, when the vessel reaches the measurement point, the undulating CTD sinks freely by its own weight. In our measurements this was at a rate of 1-1.5 m/s. Then, for a vertical cast is takes about 2-3 min, depending on the depth.

The measurements used in this study were obtained by two types of CTD profilers: SBE-19 plus (www.seabird.com) and RBR XR-620 (www. rbr-global.com). The latter is preferable, as it is more easy to use (in water it weighs only 0.39 kg). The latter has a higher frequency of measurement (6 Hz sampling) and provides sufficient memory for 2,400,000 readings, which can be logged using one set of high-powered 3V lithium cell batteries. It is also important to implement into the XR-620, a RDB 6 Inductive sensor, which excludes "emission" of salinity values that ensures a smooth vertical profile. The logger range is able to support additional sensors to measure pH, dissolved oxygen, fluorescence, turbidity and transmittance (www. rbr-global.com).

Calculation of geostrophic currents

The geostrophic method is based on a simplification of oceanic dynamics, where the effects of friction, high frequency movement and lateral boundaries are neglected (Cushman-Roisin & Beckers, 2011). The balance is given only between the horizontal pressure gradient force and the Coriolis force:

$$fu = -\frac{1}{\rho_0}\frac{\partial p}{\partial y},\ fv = \frac{1}{\rho_0}\frac{\partial p}{\partial y} \qquad (1)$$

Where (u, v) are the (eastward, northward) components of the velocity, ρ_0 is the reference density, p is the pressure and f is the Coriolis parameter.

For calculation of the geostrophic currents, the package GSW-TEOS10 (McDougall and Barker, 2011) was used, which transforms temperature and salinity to the new convention, and also estimates geopotential anomalies and geostrophic velocity, that is, the component of the average horizontal velocity that is perpendicular to the imaginary line that joins CTD casts relative to a level of no movement (Figure 2b). The entire set of raw hydrographic data were cleaned and smothered in order to use the GSW-TEOS10.

It is clear that with one oceanographic transect in the sea, only one component of the geostrophic flow is retrieved perpendicular to that section. If two parallel transects are conducted, then two components can be obtained from the quadrilateral set formed between both transects (see Figure 2a, 2c).

Depending on the angle between the north (or east) and the direction of the survey (Figure 2c), the geostrophic currents will be analogous to eq. (1). As a result, the parallel transects allow for the estimation of the module and horizontal direction of currents for a chosen level within any quadrilateral formed by the four nearest vertical soundings, as shown in Figure 2c, d. In this simple case, the number of combinations of any quadrilateral set taken as two points can retrieve up to six sections (see Figure 2c).

In each pair of vertical soundings, the coordinates can be obtained by a GPS to find the angle α between the north (or east) and the direction of the transect line. After that the components of the geostrophic currents are obtained between each of the six pairs of casts: ba, cd, ad, bc, ca and bd, shown on Figure 2c, where the obtained values of the currents were projected onto their corresponding coordinate u (east) and v (north) , and the final horizontal vector of geostrophic currents is obtained as the vector average of components in the center of mass of each quadrilateral set (Figure 2d).

Filtering out the fluctuations caused by internal waves

The dynamics of water masses on the continental shelf of the Mexican Pacific coast is affected by barotropic and baroclinic tides. Internal tides are known to cause significant vertical variations in all the hydrophysical parameters on the continental shelf. Defand (1950) first showed that internal tides may cause the temperature and salinity measurements on the continental shelf to provide different results with respect to the geostrophic currents, depending on the tidal phase in which they were taken.

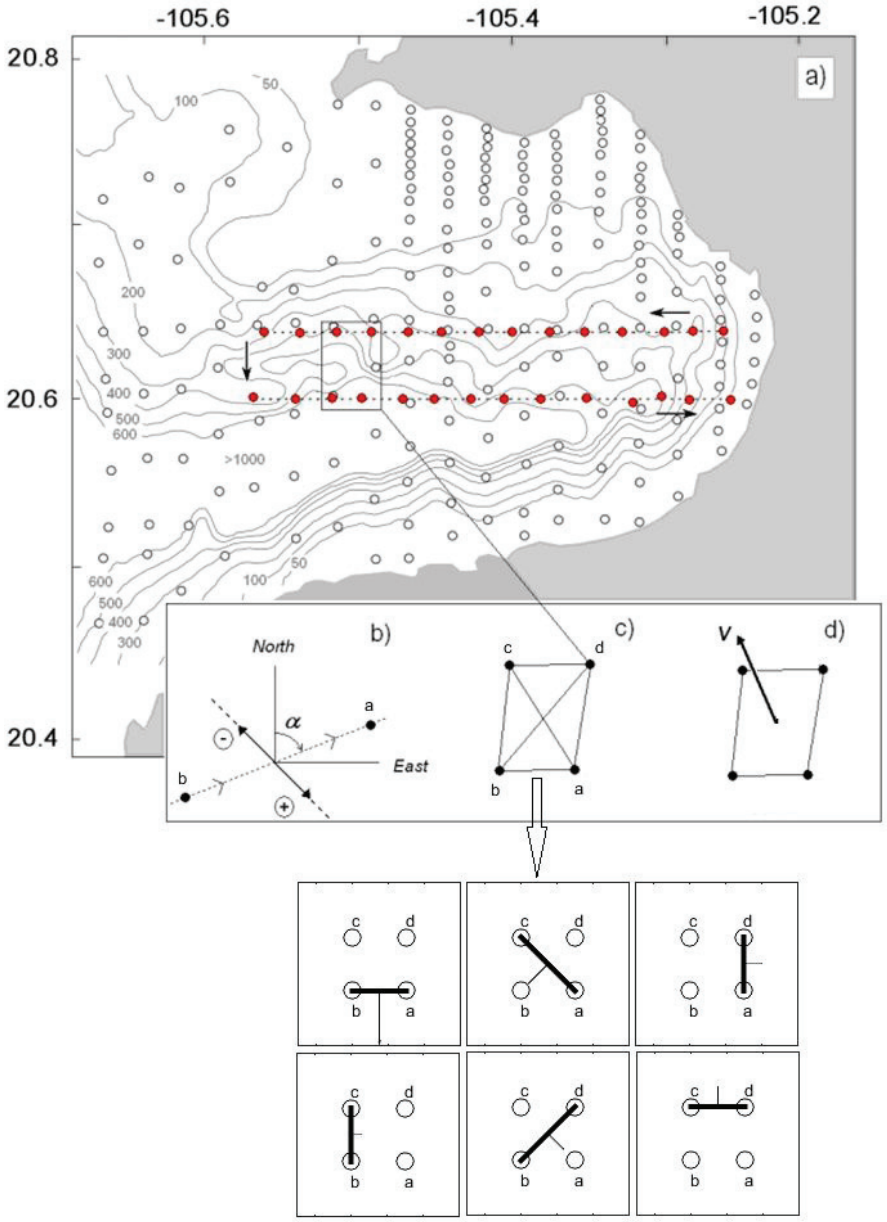

Figure 2. a) Position of profiles sounding made at Banderas bay on 16-18 October 2009. Open circles show the position of vertical sounding by undulated CTD profiler SBE-19 plus. Red circles show the two lines made to validate this methodology. b) Scheme of measurement the component of geostrophic flow between two vertical soundings. The thick arrows show the positive and negative components of the geostrophic flow, perpendicular to the direction of the section. c) Four points to determine the geostrophic vector and the corresponding section for each pair. d) Average vector of geostrophic current obtained from the calculation of six components perpendicular the lines: ab, ac, ad, bc, and cd.

Filonov *et al*. (2000) proposed a method to conduct a rapid oceanographic survey with an undulating CTD in a grid of numerous and successive casts that would allow them to filter out the data to remove the influence of internal waves. In this study, we employ the filtering method proposed by Filonov (2000), which is based on smoothing the fields of temperature and salinity with a filter whose parameters are determined by the shape of the spatial correlation function of the field's pulses. The filtering method was successfully tested using data from rapid oceanographic surveys during measurements in different areas of the Mexican continental slope (Filonov, 2000; Plata *et al*., 2006; Filonov, 2011; Filonov *et al*., 2014).

Results and discussion

The validation of the proposed method was checked out using the data from two parallel transects made in October 2009 in the central part of Banderas Bay. From these data, the average of geostrophic currents in the 10 m layer were found referenced to a depth of 200 m. The corresponding vectors for these currents are shown in Figure 3. In the same figure, the pressure anomaly distribution of the bay and the surface geostrophic currents calculated from a regular mesh using objectively mapping according to the spatial oceanographic survey in October 2009 is shown (see Figure 2). The surveys was carried out using the undulating CTD SBE-19 plus.

The current pattern comprises an alternating movement from north to south directions along the whole transect. The most intense currents reach 0.06 cm/s near the west end of the transect (entrance to the bay). At the inner section of the bay, the currents present slower speeds (around 0.01 cm/s). From surface and below (not shown), within the first 50 m, the currents present speeds of 0.04 cm/s, whereas below that, from 50-100 m, the intensity decreases almost 30% (0.02 cm/s). This behavior is due to the position of the thermocline within the bay, which typically lies around 40-50 m deep.

To quantify the error, the normalized root mean square error was computed from

$$NRMSE = \frac{\sqrt{\frac{\Sigma_N (U_g - U_{obj})^2}{N}}}{\overline{U_{obj}}} \qquad (2)$$

Where U_g corresponds to the computed geostrophic velocity, U_{obj} is the geostrophic velocity from objectively mapping, N the total station in a specific level, and $\overline{U_{obj}}$ is the mean. The root-mean-square deviation between both calculations was less than 3.5 %.

As in earlier studies (Pantoja *et al.*, 2016), the circulation of the bay constantly presents the formation of 2-3 vortices with diameters of 15-30 km, located along the axial line of the bay because of the deep submarine canyon. The eddies are formed due to the interaction of the local topography (the southern and northern capes, and the submarine canyon) with jets of the Mexican Coastal Current that penetrates into the bay from the south. At the early stage of the eddy generation, the nonlinear components of the advection are dominant, but once the jet of the Mexican Coastal current ceases, geostrophic currents form a well-defined structure into the bay that remains up to 15 days. In the upper layer

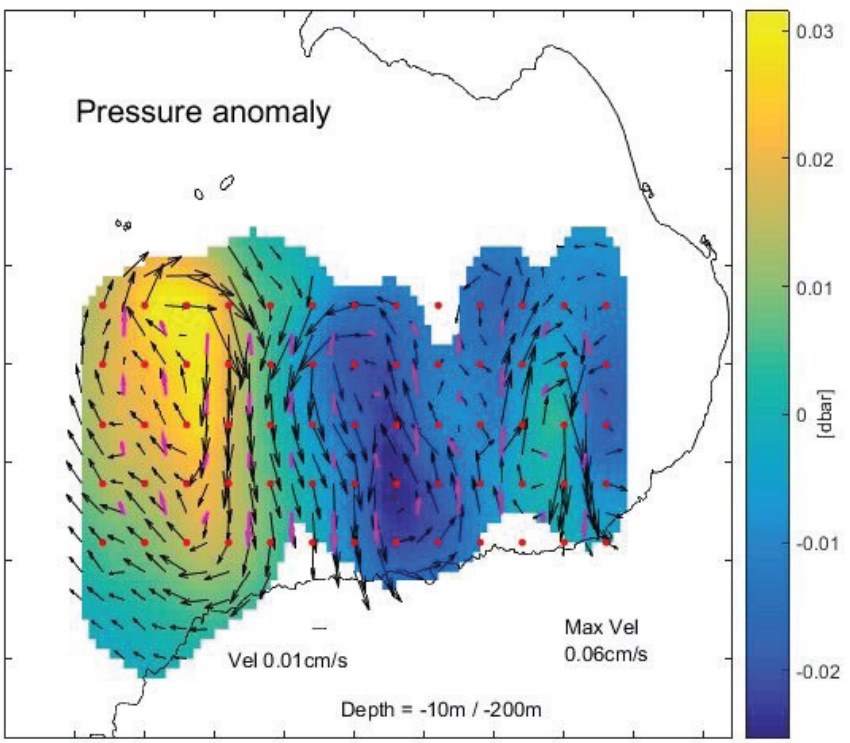

Figure 3. Field of geostrophic currents velocities computing with objective mapping (black arrows) vs. vectors of geostrophic currents (magenta vectors) generated with the proposed method at different sections. The background color represents the ocean pressure anomaly at 10 m depth, measured 16-18 October 2009. Note that every quadrilateral formed is a subset of the total set of observations. Only CTD casts greater than 200 m were considered.

(at least above 500 m) the currents can be considered in geostrophic balance, yet below this depth the currents obey a direction given by the pressure gradient force due to the narrowness of the canyon.

Conclusions and final Remarks

As it is known, CTD cast cannot be used to compute geostrophic currents when they are shallower than 100 m. Fortunately along the Mexican coast, there are several regions (as in other places around the word) where the continental shelf is narrow and one can reach the 200 m isobaths around 5-8 km offshore, where the geostrophic circulation can be computed without the variability present close to the coast (see for example, Obeso-Nieblas *et al*. (2014) in Bahía de la Paz, and Salinas and Pinet (1991) in Bahía Magdalena). Also, since internal tides are known to cause significant vertical variations in all the hydrophysical parameters on the continental shelf, we suggest a separation between casts should be at least 1 and 2 km to avoid further misinterpretation of the hydrography data due to the presence of internal waves which with an additional treatment can be filtered out with one of the methods mentioned in section 3.2.

Therefore, the proposed method is recommended for rapid measurement of the thermohaline structure of the sea from a marine boat (working at sea during daylight hours) and the subsequent calculation of geostrophic currents in the remote areas of the Mexican coast, where there are no specially equipped oceanographic ships. This method cannot be used in coastal zones, but in deeper waters where the geostrophic current implies length scales of the order of tens to hundreds of km. In the case of the present study, the region is a small scale bay (Banderas Bay), where the currents have been described as being stable with patterns that are persistent and well-structured due to the deep submarine canyon. In other coastal sites, as in the open seas, the geostrophic current might have much more variability and perhaps this method must be applied cautiously as the regional coastal current pattern might or might not be extrapolated providing realistic currents. However, as a first approximation this method can be used with confidence for a rapid view of observational outputs.

Acknowledgements

This work was supported by the regular budget of Universidad de Guadalajara, and through the PRODEP-Project UDG-PTC-1268 to DAP. We also are very grateful to two anonymous reviewers for the interesting and helpful suggestions on the paper which have greatly helped us to improve the manuscript, making it more clear, complete and readable.

References

Cushman-Roisin, B and Beckers, J, M. 2011. Introduction to Geophysical Fluid Dynamics, Volume 101, 2nd Edition, 875 pp, Academic Press.

Defant A. 1950. Reality and illusion in oceanographic surveys. J. Mar. Res. 9: 15–31.

Filonov, A., Monzón, C., Tereshchenko, I. 1996. Acerca de las condiciones de generación de las ondas internas de marea en la costa occidental de México. Ciencias Marinas, 22(3): 255 – 272.

Filonov, A., Monzón, C., Tereshchenko, I. 1996. A technique for fast conductivity-temperature-depth oceanographic surveys. Geofísica Internacional, 35(4): 415 – 420.

Filonov A.E., 2000. Spatial structure of the temperature and salinity fields in the presence of internal waves on the continental shelf of the states of Jalisco and Colima (Mexico). Ciencias Marinas, 26: 1-21.

Filonov, A., V. Novotryasov. 2005. Features of the nonlinear internal wave spectrum in the coastal zone, Geophys. Res. Lett., 32, L15602, doi:10.1029/2005GL023046.

Filonov, A., 2011. Inclined internal tide waves at a narrow Mexican Pacific shelf, Ocean Dynamics, doi: 10.1007/s10236-011-0409-4.

Salinas González Felipe, Pinet Plasencia René. Corrientes geostróficas frente a Bahía Magdalena Baja California Sur, México Inv. Marinas CICIMAR, 1991. Vol 6 No. 2 México.

McDougall, T.J. and P.M. Barker, 2011: Getting started with TEOS-10 and the Gibbs Seawater (GSW) Oceanographic Toolbox, 28 pp., SCOR/IAPSO WG127, ISBN 978-0-646-55621-5. http://- www.cmar.csiro.au/datacentre/extdocs/seawater.htm

Obeso-Nieblas Maclovio, Gaviño-Rodríguez Juan Heberto, Obeso-Huerta Hipolyto and Muñoz-Casillas Sandra Isaura.Spatial thermohaline variability, water masses and

geostrophic circulation in Bahia de La Paz, Gulf of California. Revi sta de B iologí a Marina y Oceanografía Vol. 49, Nº3: 413-426, diciembre 2014. DOI 10.4067/S0718-19572014000300002.

Pantoja D.A., Marinone S.G., Filonov A. 2016. Modeling the Effect of a Submarine Canyon on Eddy Generation in Banderas Bay, México. Journal of Coastal Research. doi: http://dx.doi.org/10.2112/JCOASTRES-D-15-00201.1

Plata L., Filonov A., Tereshchenko I., Nelly L., Monzon C., Avalos D., Vargas C. 2006 Geostrophic current in the presence of an internal waves field in Bahia de Banderas, Mexico. e-Gnosis. Vol 4, pp 1-43.

Pond, S & Pickard, G.L. 1983. Introductory Dynamical Oceanography. PERGAMON PRESS, EUA, 249 pp.

Geofísica Internacional (2019) 58-1: 81-99

Original paper

Injection into the shallow aquifer-aquitard system beneath Mexico City for counteracting pore pressure declines due to deeper groundwater withdrawals: Analysis of one injection well

Felipe Vázquez-Guillén* and Gabriel Auvinet-Guichard

Received: April 24, 2018; accepted: September 20, 2018; published on line: January 18, 2019

Resumen

Los acuíferos están siendo severamente sobre-explotados en muchas partes del mundo conforme al continuo aumento de las poblaciones urbanas. Además, la excesiva extracción del agua subterránea de los acuíferos ha acelerado dramáticamente la consolidación de los acuitardos sobre-yacientes, creando severos hundimientos del terreno y muchos otros problemas relacionados. La Ciudad de México, con una población de 20 millones de habitantes y un acuífero principal exhausto, es un sitio que ofrece excelentes condiciones para experimentar técnicas de compensación. En este artículo, se propone una estrategia con el propósito específico de mitigar el hundimiento del subsuelo de la Ciudad de México. La estrategia consiste en aumentar la presión de poro en el acuífero somero por debajo de la Ciudad de México con la intención de inducir un proceso de difusión a través de los acuitados superior e inferior, para generar incrementos de presión de poro en el sistema que contrarresten los actuales descensos de presión de poro asociados a las extracciones de agua subterránea en la unidad acuífera principal. La estrategia se analiza analíticamente y se utilizan parámetros hidráulicos típicos del sistema acuífero-acuitado somero por debajo de la Ciudad de México sujeto a un pozo de inyección. Los resultados proporcionan, por primera vez, las respuestas hidráulicas acopladas del sistema sujeto a la inyección de agua y proporcionarán datos útiles cuando se realicen pruebas de inyección en el futuro cercano.

Palabras clave: Difusión inducida. Soluciones analíticas. Respuestas hidráulicas acopladas. Hundimiento del terreno.

Abstract

Aquifers are being severely overexploited in several sites around the world as urban populations continue to grow. Excessive groundwater subtraction of aquifers has also accelerated the consolidation of the overlying aquitards dramatically, creating severe land subsidence and many other related issues. Mexico City, with its population of 20 million inhabitants and depleted main aquifer, is a prime site for experimental approaches for redress. In this paper, a purpose-specific strategy for the land subsidence mitigation of Mexico City is suggested. The strategy consists of rising depleted pore pressure in the shallow aquifer beneath Mexico City to induce a diffusion process through the upper and lower aquitards that generate increments of pore pressure in the system to counteract current pore pressure declines associated to groundwater withdrawals of the main aquifer unit. The strategy is analyzed on the basis of analytical solutions and typical hydraulic parameters for the shallow aquifer-aquitard system beneath Mexico City subject to one injection well. The results provide for the first time the coupled hydraulic responses of the shallow aquifer-aquitard system beneath Mexico City subject to water injection and provides useful data for field injection tests to be conducted in the near future.

Key words: Induced diffusion. Analytical solutions. Coupled hydraulic responses. Land subsidence.

F. Vázquez-Guillén*
G. Auvinet-Guichard
Instituto de Ingeniería
Coordinación de Geotecnia
Universidad Nacional Autónoma de México
Ciudad Universitaria, Apdo. Postal 70-472
Coyoacán, 04510
CDMX, México.
Corresponding author: fvazquezg@exii.unam.mx

Introduction

Mexico City is located within the southwestern portion of the Basin of Mexico (Figure 1). Conventionally, the Valley of Mexico refers to the lowest area of this basin. It is essentially an extensive plain at an average altitude of 2240 m above sea level formed by low strength, very compressible, lacustrine clayey aquitards partially overlying highly productive regional aquifers of volcanic and sedimentary origin. Over 20 million people in Mexico City and its metropolitan area rely on groundwater as their main water resource. Currently, greater rates than can be naturally replenished are being subtracted from one of these aquifer units, so in several detected locations it is overexploited (Conagua, 2009; NRC, 1995).

Consequences of such excessive groundwater exploitation extend well beyond decreasing freshwater availability for residents in Mexico City. This exploitation has also accelerated the aquitard's consolidation dramatically, creating non-uniform spatially distributed land subsidence all over the Valley of Mexico. Areas where aquitards are at their thickest, subsidence may reach rates of 0.40 m per year (Auvinet *et al*., 2017). Zones where thickness and/or compressibility of aquitards vary steeply, differential settlements (from point-to-point) become so disparate that, beyond a certain limit, the soil begins to fracture (Auvinet *et al*., 2013). Soil fracturing has caused the collapse of buildings, breakage of water and sewage pipelines, wastewater flooding and leakages (Jimenez *et al*., 2004). Several studies have confirmed that through such fractures, aquifers are directly exposed to pollution caused by wastewater and garbage leaching (Mazari and Mackey 1993). In addition, large portions of the lacustrine sediments in the valley exhibit piezometric depressions (Figure 2a) and increments of effective stresses (grain-to-grain) (Figure 2b). As water exploitation continues, rates of subsidence and differential settlements increase constantly. This cumulative process makes both the size of the subsiding area and the damage on the built-up environment to increase. Under these conditions, building and/or maintaining the operational capacity of any engineered work within the valley requires prognoses of piezometric losses, rates of ground consolidation and subsoil deformations at the site in question (Reséndiz *et al*., 2016).

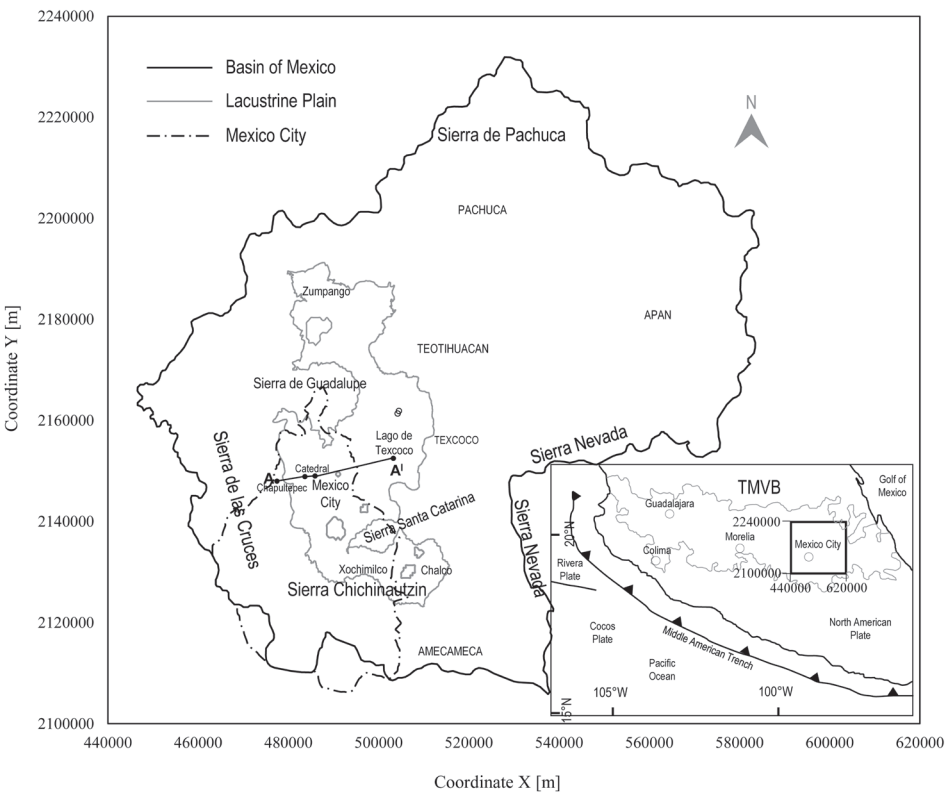

Figure 1. The location of Mexico City within the context of the Basin of Mexico. TMVB stands for Trans-Mexican Volcanic Belt.

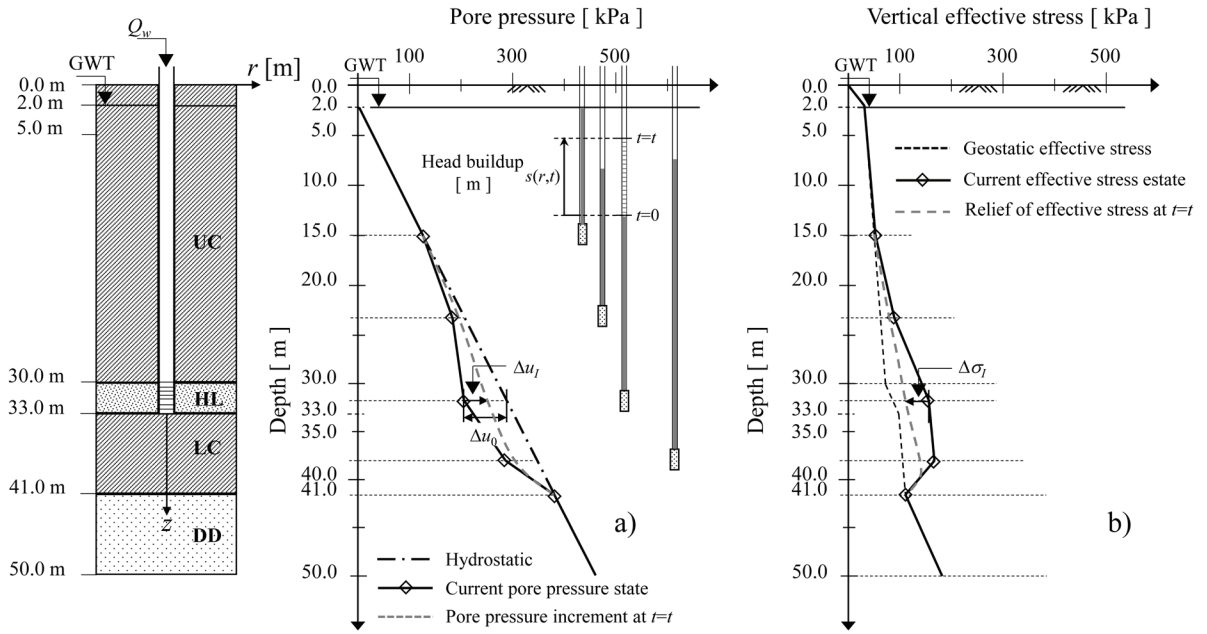

Figure 2. Profiles illustrating typical conditions in the lacustrine plain beneath Mexico City and the purpose of the injection well studied in our investigation: a) Pore pressure, b) Vertical effective stress. UC: Upper Clay; HL: Hard Layer; LC: Lower Clay; DD: Deep Deposits.

Over the last few decades, Comisión Nacional del Agua (Conagua) and Sistema de Aguas de la Ciudad de México (Sacmex) have implemented a program in Mexico City to deal with aquifer overdraft and meet the ever increasing water demand (Conagua, 2006; DGCOH, 1997; DGCOH and Lesser, 1991). Among the main actions of this program, one consists of artificially recharging the main production aquifer with treated waste water and/or rainfall water at a rate of 10 m^3/s using injection wells located to an average depth of ~150 m (DGCOH, 1997). Artificial recharge attempt to reduce the aquifer's overdraft within Mexico City's area estimated in ~22 m^3/s (World Bank, 2013). The authorities also expect to reduce land subsidence through this program, but this benefit is seen as a collateral effect; they are mostly concerned with restoring abstracted volumes of water to the main production aquifer safely.

The most significant efforts to implement a recharge program began at the end of the past century when water injection tests were conducted as part of the activities of "Proyecto Texcoco" (Cruickshank, 1998). This project aimed to create a storage wastewater reservoir consisting of several artificial lakes by consolidation of in-situ soils through groundwater extraction wells. Around the same time, aquifer recharge activities were implemented in other sites in Mexico City, specifically around the treatment plants in "Cerro de la Estrella" (19°20'11.58" N; 99° 4'29.21" O) and "San Luis Tlaxialtemalco" (19°15'29.87" N; 99° 1'46.31" O). Single-well injection rates of 0.05 m^3/s and of 0.06 m^3/s were used to recharge the main aquifer unit in these two sites (DGCOH, 1997). In 2007, as a result of these investigations, Conagua published the first official standards in the country regarding the recuperation of aquifers and protection of groundwater (NOM-014-Conagua-2007; NOM-015-Conagua-2007). Presently, the artificial recharge technique and the interaction between the native water and the injected water are still under examination (Huizar *et al*., 2016; Conagua, 2006).

Artificial recharge studies relating to Mexico City have examined the general performance of injection wells in the field (Cruickshank, 1998), the feasibility of using reclaimed wastewater as the injected water (Carrera and Gaskin, 2007; DGHOH, 1997), the impact of injecting treated wastewater on the quality of the native water (Conagua, 2006; DGHOH, 1997) and the rates at which water can be injected at specific sites (Cruickshank, 1998; DGCOH and Lesser, 1991). However, there has not been a study of underground injection for

land subsidence mitigation. Thus, this paper examines underground injection specifically as a strategy for the land subsidence mitigation of Mexico City. In other words, we investigated an injection well whose main purpose was not to restore abstracted volumes of water to the main aquifer unit, but rather, to counteract current pore pressure declines in the aquitards as a result of groundwater withdrawals. Figure 2 illustrates the setting of the injection well considered in our investigation. The results of this study provide for the first time the coupled hydraulic responses of the shallow aquifer-aquitard system beneath Mexico City subject to water injection and provides useful data for field injection tests to be conducted in the near future.

Principles of water injection into aquifer-aquitard systems

In alluvial, lacustrine and shallow-marine environments, clayey aquitards often appear interbedded and interfingered with sandy and gravelly aquifers. Aquifers may be confined and semiconfined by aquitards. Most of the times, there is a large permeability contrast between aquifers and aquitards and also aquitards are of a highly compressible nature. These characteristics make that an aquifer-aquitard system respond to fluid injection as a leaky-aquifer system for practical purposes. Leaky-aquifer systems are represented by alternating layers of aquifers and aquitards, each of which is characterized with its hydraulic conductivity, specific storage and thickness. Thus, the coupled hydraulic responses of leaky-systems (pore pressure responses, head buildup in aquifers and leakage rates through aquitards) involve the hydraulic parameters of both aquifers and aquitards. Several authors have discussed the hydrodynamics of wells in such systems (e.g. Neuman and Witherspoon, 1969; Herrera and Figueroa, 1969; Herrera, 1970; Herrera, 1976; Cheng and Morohunfola, 1993; Cihan *et al*., 2011). The theory of effective stress and one-dimensional consolidation (Terzaghi, 1925), is directly applicable to the understanding of the behavior of aquifer-aquitard systems subject to water injection (Domenico and Mifflin, 1965). Alternatively, the aquitard-drainage model can be used for the same purpose (Tolman and Poland, 1940).

In the following, a leaky-aquifer system consisting of one aquifer underlying one aquitard is considered. To better appreciate the impact of water injection on land subsidence mitigation, the phenomenon of land subsidence is explained first. Figure 3 illustrates a typical compressibility curve of Mexico City's clay that represents the consolidation of the overlying aquitard subject to the influence of groundwater withdrawals in the underlying aquifer. Due to the large permeability contrast between the aquifer and aquitard, head declines in the aquifer give rise to excess pore pressure in the aquitard that diminishes toward the land surface. A transient downward movement of water through the aquitard is thus induced that reaches a steady state condition when the hydraulic head in the aquitard equilibrates with the head change in the adjacent aquifer.

During the transient state condition, total stress in the aquifer-aquitard system remains constant, so changes in pore pressure are associated with equal and opposite changes in effective stress. As a result, effective stress (σ'_v) increases and a reloading of the aquitard takes place. Initially, the increment in effective stress in the aquitard may be small and thus, land subsidence may be so as well. However, as soon as the preconsolidation stress (σ'_p) is surpassed, the aquitard suffers deformations on the virgin loading curve with a sudden increase in compressibility and subsidence rate (stress path 1-2). This inelastic compression of the aquitard is responsible for the vast majority of land subsidence.

The injection well studied in our investigation attempts to counteract this ongoing process by increasing pore pressure in the aquitard by diffusion. As a result of this practice, the effective stress is decreased causing the aquitard to recover a small portion of the total deformation (stress path 2-3). Evidence of this response has been found during underground injection tasks conducted in several sites around the world (Zhang *et al*., 2015; Zhou and Burbey, 2014; Amelug *et al*., 1999), where decrements in effective stress have been indirectly verified by measuring expansions at specific hydro-stratigraphic units of the injection formation. For the shallow aquifer beneath Mexico City, the limiting value of the increment in pore pressure may be bounded by the hydrostatic profile, yet theoretically, only a small value is needed in order to mitigate subsidence. In practice, however, it is necessary that further increments of effective stress in the aquitard associated to groundwater subtraction of the main aquifer unit be counteracted by the injection well. After increments of effective stress in the aquitard have been counteracted, subsidence in Mexico City can be mitigated or even arrested. Otherwise, the tendency of subsidence will continue unabated (stress path 2-4).

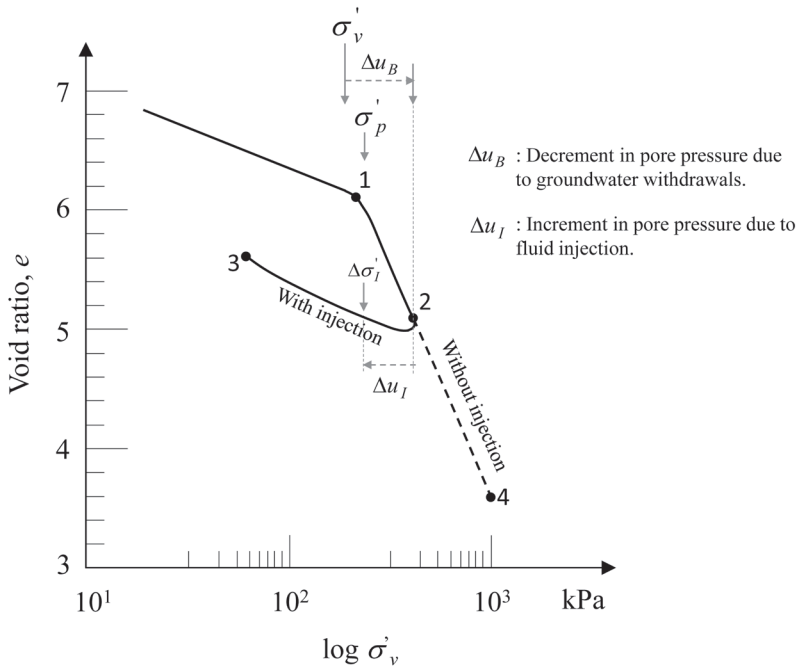

Figure 3. Typical compressibility curve of the Mexico City's clay illustrating the effects of groundwater extraction and water injection.

Previous applications of underground injection

The first applications of underground injection addressing land subsidence issues appeared within the oil industry. At the end of the 1950's, water injection into the subsurface was used to mitigate excessive surficial settlements originated by oil extraction in the Wilmington field, Long beach, California (Otott and Clarke, 1996). Later on, this strategy was adopted by several countries as a complementary policy for land subsidence mitigation and its implementation showed promising results (Poland, 1972; Poland, 1984). Cities where this practice has successfully been implemented include: Las Vegas (Amelug *et al*., 1999; Bell *et al*., 2008), Shanghai (Zhang *et al*., 2015; Shi *et al*., 2016) and Bangkok (Phien *et al*., 1998), among others. Depending on the magnitude of the induced expansions and the management of the groundwater extractions, land subsidence in these cities has been controlled, mitigated or arrested. Moreover, a water injection project led by the University of Padua which aims to uplift the city of Venice in order to protect it from periodic floods is at a very advanced stage of development (Gambolati and Teatini, 2014). Recently, the project has been studied carefully through numerical simulations (Teatini *et al*., 2010) and researchers expect to perform injection tests for calibrating the developed computational tools in the near future (Teatini *et al*., 2011). In Mexico City, however, injection sites have not been studied for their potential ability to mitigate land subsidence, despite several decades of injections for the purpose of water replenishment.

Shallow aquifer-aquitard system beneath Mexico City

The fill of the Mexico Basin comprises lacustrine and alluvial deposits. The upper most ~100-150 m of this fill has been described by several researchers (Marsal and Mazari, 1959; Zeevaert, 1982; Vázquez and Jaimes, 1989). For illustrative purposes, one stratigraphic cross-section E-W of the upper ~90 m of such fill is shown in Figure 4a. Specifically, the lacustrine deposits of the basin fill consist of low strength, highly compressible clays and allophanes (Ovando *et al*., 2013). The average thickness of the lacustrine deposits is ~40-50 m beneath Mexico City but increases significantly outside the city limits. Beneath Mexico City, lacustrine deposits are present in two formations –the upper and lower clay formations-- clearly divided by a lens of only a few meters thick composed mainly of sands, gravely sands, and thin lenses of soft silty clays (Ovando *et al*., 2013). The National Research Council called this permeable unit the "shallow aquifer" because it provided freshwater to

Mexico City in the mid to late 1800s (NRC, 1995). The soil mechanics community refers to this soil stratum as the first "hard layer" after Marsal and Mazari (1959). Overlying the upper clay formation, a crust of dried low plasticity silty clays is found, which in turn underlies an anthropogenic fill. The alluvial deposits of the basin fill, in contrast, comprise very consistent silts and sandy silts interbedded with hard clays. Marsal and Mazari (1959) refer to these soils as the "deep deposits" when they appear underlying the lower clay formation.

The vertical hydraulic conductivity of the aquitards varies between ~$5x10^{-9}$ ms^{-1} and ~$20x10^{-9}$ ms^{1}, whereas their specific storage coefficient is found in the range of ~$1x10^{-2}$ s^{-1} to ~$15x10^{-2}$ s^{-1} (Herrera *et al*., 1989). Marsal and Mazari (1959) demonstrated through geotechnical explorations that the clay sediments become stiffer and less permeable with depth. Some authors have found evidence of reduced hydraulic conductivity during field-permeability tests. Near the aquifer-aquitard interface, Rudolph *et al*. (1991) found values in the range of $2.5x10^{-9}$ ms^{-1} to ~$3.5x10^{-9}$ ms^{-1} in the Texcoco area, and Vargas and Ortega (2004) found values between $3x10^{-11}$ ms^{-1} and $3x10^{-10}$ ms^{-1} in one site near downtown Mexico City. For the hard layer, Rudolph *et al.* (1989) report average values of $1x10^{-4}$ ms^{1} and of $8x10^{-5}$ ms^{-1} for the hydraulic conductivity and values of $1x10^{-3}$ m^{-1} and of $2x10^{-3}$ m^{-1} for the specific storage coefficient. Herrera *et al.* (1989) report values for the horizontal hydraulic conductivity of the deep deposits generally ranging between $1x10^{-5}$ ms^{-1} and $15x10^{-5}$ ms^{-1} with isolated values of $0.01x10^{-5}$ ms^{-1} and values from $1x10^{-6}$ m^{-1} to $10x10^{-6}$ m^{-1} with isolated values of $0.01x10^{-6}$ m^{-1} for the specific storage coefficient.

Before extensive groundwater withdrawal from the shallow aquifer in the mid to late 1800s, both the regional aquifer and shallow aquifer were subject to artesian pressure (NRC, 1995), so natural discharge paths caused water to move upward through the aquitards (Durazo and Farvolden, 1989). Currently, extensive groundwater subtraction has inverted the gradients and water is now moving downward in most of this area (Ortega and Farvolden, 1989). Thus, aquitards are now contributing to the aquifer's yield by leakage flux which is derived mainly from a depletion of storage in the clayey aquitards.

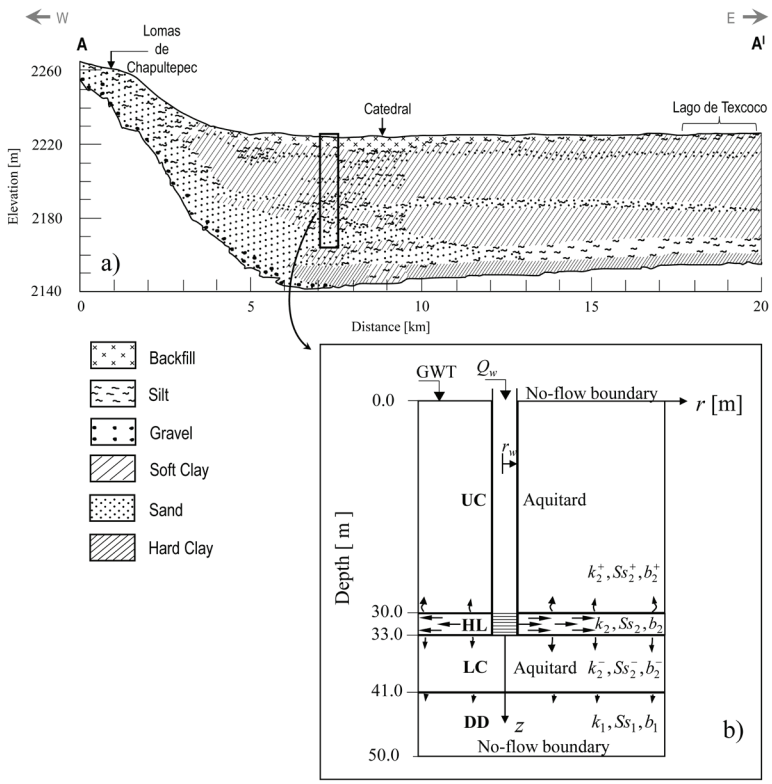

Figure 4. Illustration of the subsoil beneath Mexico City (Modified after Marsal and Mazari, 1959): a) Cross-section W-E through the lacustrine plain; the location of cross-section AA' is indicated in Figure 1, b) Conceptual model of the shallow aquifer-aquitard system.

On the basis of field and laboratory data collected over the last decades related to the compression of the upper aquitard in the central part of Mexico City (Ovando *et al*., 2003), it is estimated that leakage of the upper aquitard may account for ~50-60% of total land subsidence in this area. Leakage flux of aquitards together with the initial exploitation of the shallow aquifer may also explain the typical conditions for pore pressure decline observed in most of the lacustrine plain. Pore pressures in the upper ~15 m are often found at hydrostatic conditions, yet in deeper sandy layers within the clays, pore pressure depletion rates from 0.002 to 0.014 kPa per year have been reported by some research (Ovando *et al*., 2003). Hence, any injection project designed to mitigate aquitard's consolidation process induced by the depletion of pore pressures as a consequence of the exploitation of the main aquifer should increase pore pressure in aquitards to a faster rate. This paper provides a first estimate of pore pressure restoration rates taking into account the coupled flow in aquifers and aquitards on the basis of the following mathematical model.

Mathematical model for water injection

The mathematical model for water injection adopted here is based on a set of governing equations formulated to represent transient groundwater flow in a homogeneous and isotropic, confined multilayered aquifer-aquitard system of infinite horizontal extension with one injection well screened over the entire thickness of selected aquifers. Figure 4b illustrates one such system consisting of two aquifers and two aquitards. The flow pattern induced by the injection well is assumed to be horizontal in aquifers and vertical in aquitards. This assumption is widely used in practice as long as the hydraulic conductivity contrast between aquifers and adjacent aquitards is at least of one order of magnitude (Neuman and Witherspoon, 1969). The exchange of water that occurs through the aquifer-aquitard interfaces as a result of the injection of water is called leakage. In such leaky-systems, horizontal flow in aquifers is coupled with each other by accounting for diffuse leakage through aquitards according to the following system of governing equations.

Governing equations for multilayered systems

In terms of the hydraulic head buildup $s_i = s_i(r,\ t)$ [L], single-phase radial flow in aquifer i of the multilayered system is described by the following governing equation (Cihan *et al*., 2011):

$$\frac{1}{r}\frac{\partial}{\partial r}\left(r\frac{\partial s_i}{\partial r}\right)=\frac{1}{D_i}\frac{\partial s_i}{\partial t}+\frac{w_i^-}{T_i}+\frac{w_i^+}{T_i};\ i=1,\ldots,N, \tag{1a}$$

where $s_i = h_i(r,\ t)-h_{i0}$ with h_i [L] being the hydraulic head in aquifer i and h_{i0} the initial head in that aquifer. $D_i = k_i/Ss_i$ [L^2T^{-1}] is the hydraulic diffusivity where k_i [LT^{-1}] is the hydraulic conductivity and Ss_i [L^{-1}] is the specific storage coefficient of aquifer i. $T_i = k_i b_i$ [L^2T^{-1}] is the transmissivity with b_i [L] being the thickness of aquifer i. r [L] is the radial distance from the center of the well and t [T] is the time. w_i^α [LT^{-1}] denotes the rate of diffuse leakage (i.e. specific discharge) through the aquifer-aquitard interface from aquifer i into the overlying ($\alpha = +$) or underlying ($\alpha = -$) aquitard, and can be calculated according to:

$$w_i^\alpha=-\frac{k_i^\alpha}{b_i^\alpha}\frac{\partial s_i^\alpha}{\partial z_{D_i}^\alpha}\bigg|_{z_{D_i}^\alpha=0} \tag{1b}$$

where $s_i^a = s_i^a(r, z_{D_i}^a, t)$ [L] is the hydraulic head buildup in aquitard $(i,\ \alpha)$, k_i^a [LT^{-1}] is the hydraulic conductivity and b_i^a [L] is the thickness of that aquitard. $z_{D_i}^a = z_i^a / b_i^a$; $\{0 \le z_{D_i}^a \le 1\}$ is the dimensionless local vertical coordinate and z_i^a [L] is the local vertical coordinate, with $z_i^a = 0$ at the interface between aquifer i and aquitard $(i,\ \alpha)$, and $z_i^a = b_i^a$ at the interface between aquifer $i+\alpha$ and aquitard $(i,\ \alpha)$. Note that $i+\alpha = i+1$ for $\alpha = +$, while $i+\alpha = i-1$ for $\alpha = -$.

The vertical flow through aquitard $(i,\ \alpha)$ is described by the well-known diffusion equation:

$$\frac{\partial^2 s_i^\alpha}{\partial z_{D_i}^{\alpha\ 2}}=\frac{(b_i^\alpha)^2}{D_i^\alpha}\frac{\partial s_i^\alpha}{\partial t};\ 0 \le z_{D_i}^\alpha \le 1 \tag{2a}$$

subject to boundary conditions at aquifer-aquitard interfaces:

$$\begin{aligned} s_i^\alpha(r,0,t) &= s_i(r,t) \\ s_i^\alpha(r,1,t) &= s_{i+\alpha}(r,t), \end{aligned} \tag{2b}$$

where $D_i^\alpha = k_i^\alpha / Ss_i^\alpha$ is the hydraulic diffusivity and Ss_i^α is the specific storage coefficient of aquitard $(i,\ \alpha)$. In equation (2b), there is a relationship such that $s_i^+(r, z_{D_i}^+, t) = s_{i+1}^-(r, z_{D_{i+1}}^-, t)$ for $z_{D_{i+1}}^- = 1 - z_{D_i}^+$.

Assuming that the entire system of aquifers and aquitards is at hydrostatic pressure at $t = 0$, the initial conditions for the system can be written as:

$$s_i(r, t=0) = 0, \quad s_i^{\alpha}(r, z_{D_i}^{\alpha}, t=0) = 0. \tag{3}$$

Outer boundary conditions are:

$$s_i(\infty, t) = 0, \quad s_i^{\alpha}(\infty, z_{D_i}^{\alpha}, t) = 0. \tag{4}$$

The top and bottom boundaries of the system may have either a zero head buildup or a non-flow condition:

$$s_1^{-}(r,1,t) = 0 \text{ or} \tag{5a}$$

$$\partial s_1^{-}(r,1,t) / \partial z_{D_1}^{-} = 0, \tag{5b}$$

$$s_N^{+}(r,1,t) = 0 \text{ or} \tag{6a}$$

$$\partial s_N^{+}(r,1,t) / \partial z_{D_N}^{+} = 0. \tag{5a}$$

As mentioned above, Equations (1)-(6) couple the one-dimensional radial flow in aquifers with each other through the vertical flow in aquitards.

Boundary conditions for one injection well

In presence of one injection well with constant or time-dependent injection rate, the boundary condition at the radial wall of the cylindrical well interval screened in any aquifer is written as:

$$-2\pi r_{wi} T_i \frac{\partial s_i(r_{wi}, t)}{\partial r} = Q_i(t); \; i = 1, \ldots, N, \tag{7}$$

where $Q_i(t)$ is the injection rate through the injection well with radius r_{wi} fully screened into aquifer i, and s_i is the corresponding head buildup in that aquifer. Conventionally, $Q_i(t) > 0$ is used for injection. As a first approximation, no skin effect nor well bore storage are taken into account.

Analytical solutions for one injection well

Analytical solutions to Equations (1)-(7) were obtained by Cihan *et al*. (2011a,b) using the Laplace transform method. The solution procedure essentially consists of transforming the governing equations into the Laplace-domain (Cihan *et al*., 2011a; Cheng and Morohunfola, 1993; Zhou *et al*., 2009) and solving the resulting system of ordinary differential equations by applying the eigenvalue analysis method (Churchill, 1966; Hunt, 1985). The set of analytical solutions used in this paper are explained in the sequel.

The head buildup in the aquifers of a multilayered system with one injection well and diffuse leakage is given by:

$$\tilde{s}_i = \sum_{j=1}^{N} c_j^I \xi_{i,j} K_0\left(r\sqrt{\lambda_j}\right), \text{ or} \tag{8a}$$

$$c_j^I = 1 \Big/ \left(2\pi E_{i,j}^I\right) \sum_{k=1}^{N} \tilde{Q}_k(p) \xi_{k,j}, \tag{8b}$$

where c_j^I are the coefficients obtained from the boundary condition at the injection wellbore which are expressed as a function of the Laplace variable p (representative of time), $\tilde{Q}(p)$ is the Laplace transform of Equation (7) (Cihan *et al*., 2011), K_0 is the zeroth-order modified Bessel function of second kind, $E_{i,j}^I = r_{wi}\sqrt{\lambda_j} K_1(r_{wi}\sqrt{\lambda_j})$ with $E_{i,j}^I = 1$ as $r_{wi} \to 0$, where K_1 is the first-order modified Bessel function of second king. λ and ξ are the eigenvalues and eigenvectors, respectively, of the eigenvalue system $(\mathrm{A}' - \lambda \mathrm{I})\xi' = 0$ with $\mathbf{A}' = \mathbf{T}^{1/2}\mathbf{A}\mathbf{T}^{-1/2}$ and $\xi' = \mathrm{T}^{1/2}\xi$, where $\mathbf{A}$ is a matrix of dimension N x N referred to as the diffuse-leakage-coupling matrix, $\mathbf{T}$ is the diagonal transmissivity matrix of dimension N x N with components T_i and $\mathbf{I}$ is a unit diagonal matrix.

The rate of diffuse leakage through the aquifer–aquitard interface between aquifer i and its neighboring aquitard (i, α) can be calculated by integration of the diffuse leakage over the entire interface area (Zhou *et al*., 2009):

$$\tilde{Q}_i^{\alpha} = 2\pi \int_0^{\infty} \tilde{w}_i^{\alpha}(r,p) r dr = \sum_{j=1}^{N}\sum_{k=1}^{N} \frac{\left(f_i^{\alpha}\xi_{i,j} - g_i^{\alpha}\xi_{i+\alpha,j}\right)}{\lambda_j} \xi_{k,j}\tilde{Q}_k(p); \quad i = 1, \ldots, N. \tag{9}$$

where $\tilde{w}_i^{\alpha}(r,p) = f_i^{\alpha}\tilde{s}_i - g_i^{\alpha}\tilde{s}_{i+\alpha}$ is the Laplace transform of the diffuse leakage. f_i^{α} and

g_i^{α} are functions that depend on the type of boundary conditions specified at the top and bottom boundaries of the system.

For the particular case of a multilayered system with no-flow condition specified at the bottom boundary (Equation 5b) or at the top boundary (Equation 6b), the corresponding equations for the head buildup in aquitards become:

$$\tilde{s}_i^{\alpha} = \left(r, z_{D_i}^{\alpha}, p\right) = \tilde{s}_i \frac{\cosh\left[\kappa_i^{\alpha}\left(1 - z_{D_i}^{\alpha}\right)\right]}{\cosh(\kappa_i^{\alpha})}, \quad (10a)$$

with:

$$\kappa_i^{\alpha}\left(p\right) = \sqrt{p/D_i^{\alpha}}\, b_i^{\alpha}, \quad (10b)$$

and the functions f_i^{α} and g_i^{α} are given by:

$$f_i^{\alpha}\left(p\right) = \left(\kappa_i^{\alpha}/b_i^{\alpha}\right)\kappa_i^{\alpha}\tanh\left(\kappa_i^{\alpha}\right), \quad (11a)$$

$$g_i^{\alpha}\left(p\right) = 0. \quad (11b)$$

Solutions to Equations (8)-(11) are obtained here using the computational code ASLMA (Cihan *et al*., 2011b). Details of the analytical solution procedure and its verification process can be found elsewhere (Cihan *et al*., 2011a; Cheng and Morohunfola, 1993). Analytical solutions calculate the transient behavior of pressure buildup in aquifers and aquitards and the rate of diffuse leakage through aquitards.

Conceptual model and its hydraulic characterization

In the present analysis, one cross-section that is deemed to be representative of the shallow aquifer beneath Mexico City is considered (Figure 4a). Then, it is simplified to a multilayered aquifer-aquitard system which consists of two-aquifers and two aquitards (Figure 4b). The aquifer between aquitards represents the shallow aquifer, whereas the overlying and underlying aquitards characterize the upper and lower clay formations. The lower aquifer represents the deep deposits. An injection well with a radius of 0.15 m is drilled vertically through the upper three layers. Then, the injection well is cased throughout the upper two layers, but it is screened over the entire thickness of the intermediate aquifer, which is the shallow aquifer. Layers of the system are assumed to be horizontal. A confined system whose lateral boundaries extend to infinity is assumed. Thus, the ground surface and bottom of the model are no-flow boundaries. The system is assumed to be under hydrostatic equilibrium with respect to the hydraulic head. Hence, computed pore pressures are in fact values in excess of the hydrostatic profile and the effect of a non-hydrostatic initial equilibrium on the relative increments in pore pressure with depth is assumed to be negligible. The conditions under which the analysis is conducted are also assumed to be representative of one injection well outside the influence range of any pumping well into the deeper production aquifer. For this analysis, hydraulic properties typical of the shallow aquifer-aquitard system beneath Mexico City area are chosen (Table 1). Values of specific storage for the upper and lower clay formations used in the analysis consider the less compressible character of the soils under the unloading stress paths imposed by the injection well, in agreement with the recommendations of several authors (Marsal and Mazari, 1959; Teatini *et al*., 2010; Teatini *et al*., 2011; Gambolati and Teatini, 2014).

Table 1. Hydraulic properties used in the conceptual model of the shallow aquifer-aquitard system beneath Mexico City subject to one injection well. UC: Upper Clay; HL: Hard Layer; LC: Lower Clay; DD: Deep Deposits.

Unit	Material	b [m]	k [ms^{-1}]	T [m^{2}s^{-1}]	Ss [m^{-1}]	S [--]
UC	Very soft and highly compressible clay.	30.0	5.0x10-9	1.5x10-7	0.015	0.45
HL	Very dense clayey sand.	3.0	5.0x10-5	1.5x10-4	1x10-4	0.0003
LC	Soft and highly compressible clay.	8.0	1.0x10-9	8.0x10-9	0.005	0.04
DD	Very dense silty sand and gravel.	9.0	1x10-4	9.0x10-4	5x10-5	0.00045

Computed hydraulic responses and discussion

Coupled hydraulic responses as a function of time of the shallow aquifer-aquitard system beneath Mexico City subject to water injection are analyzed in this section. Injection rates of 0.002 m^3s^{-1} and of 0.004 m^3s^{-1} and injection periods of 1000 d and of 5000 d are considered for analyzing the hydraulic responses. The analyzed responses comprise pore pressure responses in the entire system, head buildup in aquifers and leakage rates through aquitards. The assessment of leakage rates through the aquitards is necessary to quantify the amount of water that is transferred from the injection aquifer to adjacent aquifers through the aquitards.

Pore pressure responses

Plots of Figure 5 show the effect of the injection rate on pore pressure development at the contact between the injection aquifer (HL) and the upper clay (UC) formation. Pore pressure is plotted as a function of the radial distance from the injection well center for two injection periods. The results shown in Figure 5a and Figure 5b correspond to injection rates of 0.004 m^3s^{-1} and 0.002 m^3s^{-1}, respectively. From both plots, it is observed that pore pressure decreases as injection rate decreases and dissipates very fast near the injection well. Away from 15 m of the injection well center, pore pressure reduction becomes more gradual. The dashed line plotted in both figures indicates an upper threshold for pore pressure development calculated as the sum of the vertical effective stress at the bottom of the UC formation and the undrained shear strength of this formation at that depth. Assuming an average undrained resistance for the UC formation equal to 70 kPa at 30 m depth on the basis of the values reported by Marsal and Mazari (1959) and reading from Figure 2b a typical value for the effective vertical stress equal to 140 kPa at that depth, the upper threshold for pore pressure development yields 210 kPa. This is an estimated upper limit that should not be exceeded in order to avoid hydraulic fracturing of the UC at the contact with the HL. As can be observed in Figure 5a, an injection rate of 0.004 m^3s^{-1} induces pore pressure slightly higher than such limit very near the injection well and therefore this rate may not be adequate in some practical situations. However, the numerical value for avoiding the hydraulic fracturing of the clay may vary from site to site, and therefore it should be accurately determined in all cases.

The effect of the injection period can also be seen in the plots of Figure 5. It shows that in passing from 1000 d to 5000 d of injection, pore pressure does not increase significantly near the injection well. As the distance increases, pore pressure is increased around 15-20 kPa for an injection rate of 0.004 m^3s^{-1} (Figure 5a) and around 10 kPa for an injection rate of 0.002 m^3s^{-1} (Figure 5b).

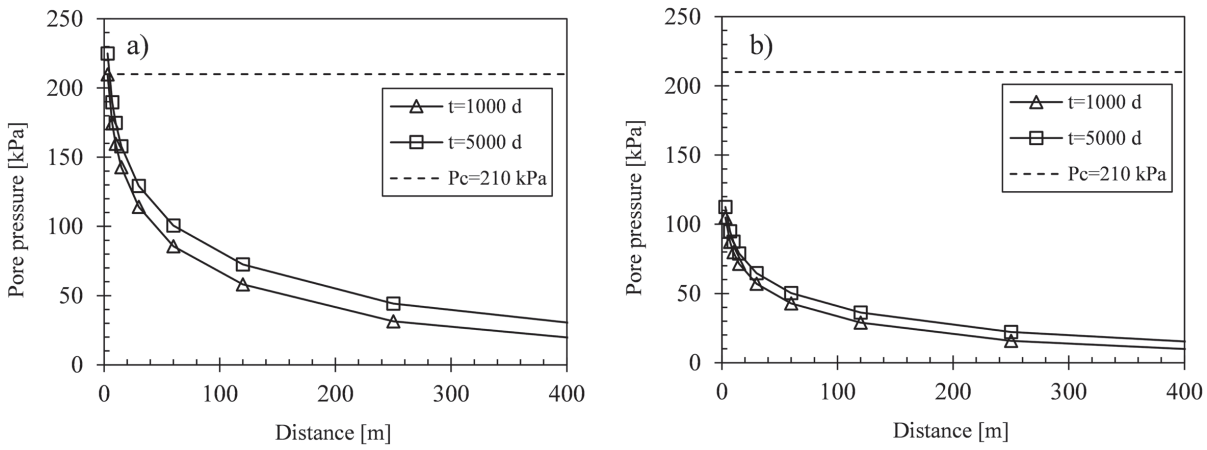

Figure 5. Effect of the injection rate and injection period on pore pressure development at the interface between the injection aquifer and the upper clay formation: a) The injection rate is Q_w=0.004 m^3s^{-1}, b) The injection rate is Q_w=0.002 m^3s^{-1}. Pc is an estimated upper threshold for pore pressure development below which hydraulic fracturing of the UC is avoided.

In order to evaluate the impact of the transmissivity of the injected formation on pore pressure development, two additional cases are now considered. The results of these analyses are shown in the plots of Figure 6. In the first case (Figure 6a), the transmissivity of the injection aquifer is increased by one order of magnitude and in the second case (Figure 6b) the transmissivity is decreased by one order of magnitude. Again, the dashed line in both plots represents the estimated upper limit for pore pressure development. It can be observed from Figure 6a that as the transmissivity of the injection aquifer increases, a higher rate of water can be injected into the aquifer without inducing pore pressure beyond the limit for hydraulic fracturing of the clay. The injection rate may even be as high as 0.03 m^3s^{-1}. However, Figure 6b indicates that as transmissivity of the injection aquifer decreases, it is necessary to reduce the injection rate dramatically in order to avoid hydraulic fracturing. In this last case, the injection rate may be as low as 0.00045 m^3s^{-1}. Therefore, the transmissivity of the injection aquifer is one of the variables with higher impact in the water injection task and this parameter should be accurately determined in the field. This finding is consistent with the results of stochastic simulations of multiphase flow. The importance of the permeability of the injection formation in application to geological CO_2 storage was pointed out in González *et al*. (2015). Authors found that the aquifer permeability have a significant influence on the pore pressure producing a wide-spread range of fluid overpressure in their stochastic analysis. As explained above, the injection period does not increase pore pressure significantly, especially near the injection well, even though the injection period increases from 1000 d to 5000 d.

Pore pressure fields through the aquifer-aquitard system generated by the injection well are shown in Figure 7 and Figure 8. The pore pressure fields of Figures 7a and 7b correspond to an injection rate of 0.002 m^3s^{-1} and injection periods of 1000 d and 5000 d, respectively. Figures 8a and 8b show pore pressure fields corresponding to an injection rate of 0.004 m^3s^{-1} and injection periods of 1000 d and 5000 d, respectively.

For both injection rates and injection periods, the highest increments in pore pressure are observed very near the injection well, at the interface between the HL and the UC and LC formations. As the injection period increases, pore pressure propagates longer distances in both directions of the Cartesian plane. Namely, for an injection rate of 0.002 m^3s^{-1}, pore pressure increments are observed at a depth of ~10 m after 1000 d of injection very near the injection well, but when the injection period increases to 5000 d, pore pressure increments extend vertically upward from the injection aquifer significantly. In the horizontal direction, pore pressure increments are observed 800 m away from the injection well center for an injection period of 1000 d and beyond 1000 m for 5000 d of injection. For an injection rate of 0.004 m^3s^{-1} and an injection

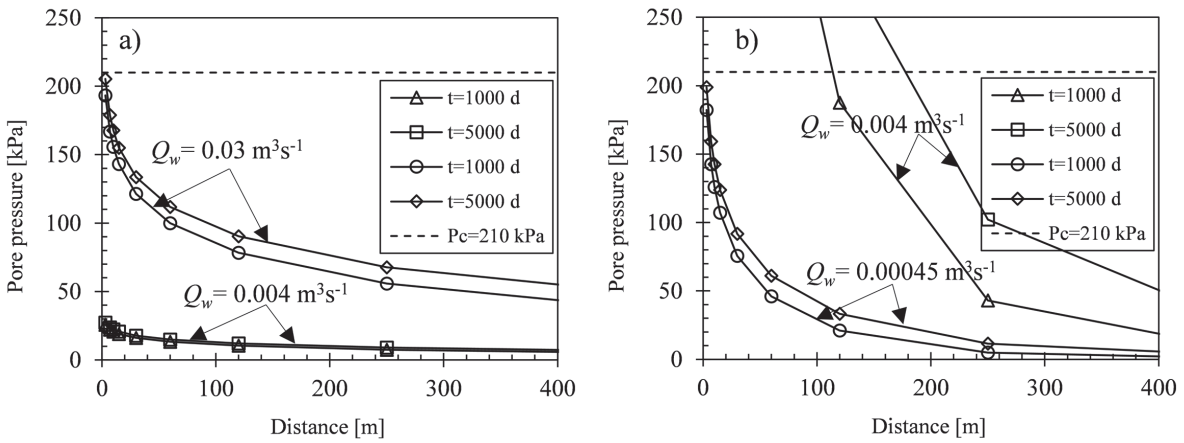

Figure 6. Effect of transmissivity of the injection aquifer on pore pressure development at the interface between the injection aquifer and the UC formation: a) The transmissivity of the injection aquifer is 1.5 x 10^{-3} m^2s^{-1}, b) The transmissivity of the injection aquifer is 1.5 x 10^{-5} m^2s^{-1}.

period of 5000 d, pore pressure propagates vertically upward until it reaches a depth of ~0.25 m near the injection well. According to results in Figure 5a, however, there is a risk of hydraulic fracturing of the UC formation very near the injection well for such an injection rate. Considering the significant benefit of injecting rates of the order of 0.004m^{3}s^{-1}, we suggest that investing sufficient resources is warranted to accurately determine the threshold at which hydraulic fracturing of the clay can occur during underground injection tasks.

Table 2 summarizes increments of pore pressure in the aquifer-aquitard system as a function of the radial distance from the injection well center, depth from the surface and injection rate after 1000 d of injection (see Figure 2a for explanation of the variables). The percentages reported in the table are calculated as the ratio of the increment in pore pressure generated by the injection well and the initial decrement in pore pressure, which is calculated as the difference between the actual and the hydrostatic profiles at corresponding

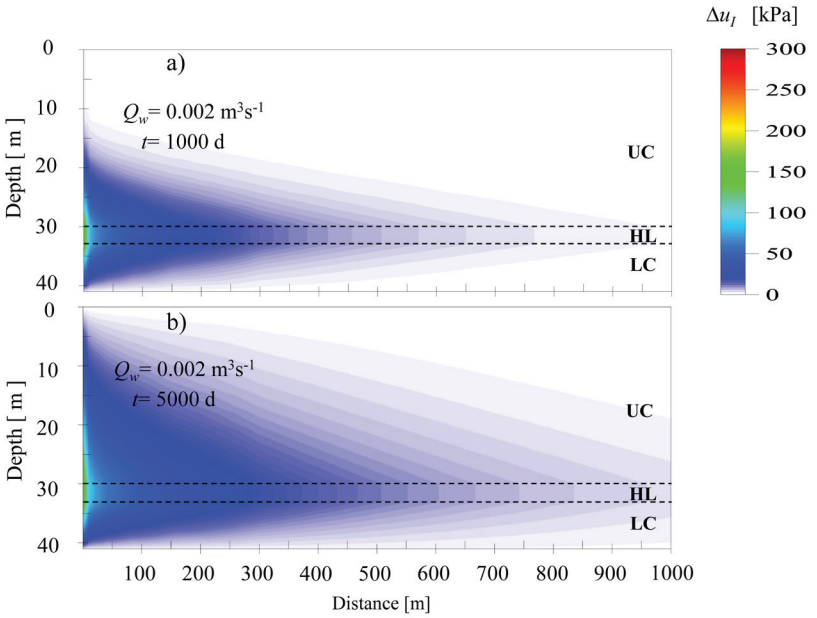

Figure 7. Pore pressure fields for an injection rate equal to 0.002 m^{3}s^{-1}: a) After 1000 d of injection, b) After 5000 d of injection.

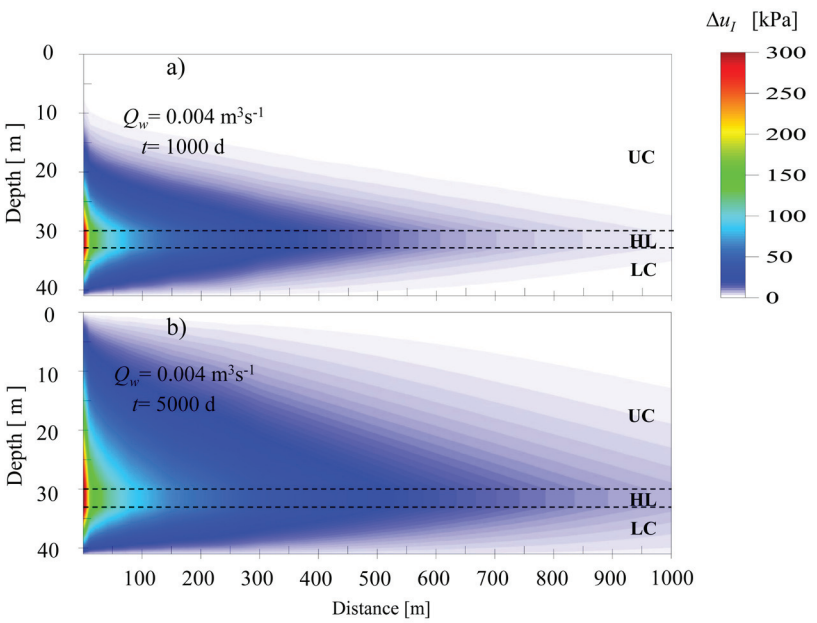

Figure 8. Pore pressure fields for an injection rate equal to 0.004 m^{3}s^{-1}: a) After 1000 d of injection, b) After 5000 d of injection.

depths (Figure 2a). The results reported in Table 2 indicate that for an injection rate of 0.002 m^3s^{-1}, ~19% of the initial deficit in pore pressure is restituted in UC formation at a depth of 23.5 m and 250 m away from the injection well center. At a depth of 38 m, ~7% of the initial deficit in pore pressure is restituted in the LC formation at 250 m away from the injection well. Note also that for the same injection rate, pore pressure in the Hard Layer (HL) does not exceed the hydrostatic conditions since only ~25.8% of the initial deficit in pore pressure is restituted in that formation. As the radial distance from the injection well increases, such values become smaller. Note, too, that pore pressure can be raised safely by maintaining the same injection rate of 0.002 m^3s^{-1}, but increasing the injection period. The corresponding values achieved by injecting a higher amount of water into the HL, for instance 0.004 m^3s^{-1}, indicates more appealing results, yet such injection rates should not be considered in pore pressure restitution projects within the lacustrine semiconfined aquifer of Mexico City unless the integrity of the UC formation can be confirmed.

Computed pore pressure restoration rates (r_u) as a function of the injection rate for different depths and radial distances from the injection well center are reported in Table 3. For an injection rate of 0.002 m^3s^{-1}, pore pressure in the UC formation (23.5 m depth) increases at a rate of 1.82-0.22 kPa per year, whereas in the LC formation (38.0 m depth), pore pressure increases at a rate of 1.64-0.23 kPa per year. Higher pore pressure restoration rates are found in the injection formation, as expected, and also when the injection rate increases. The reported restoration rates are significantly higher than the pore pressure depletion rates measured in the field by some researchers (Ovando *et al*., 2003). However, it should be noted that the present analysis is conducted in the absence of any pumping well into the deeper production aquifer. Thus, lower pore pressure restoration rates than those reported here may be expected in the field. This is particularly true in the area of the shallow aquifer-aquitard system that remains confined, which according to Carrera and Gaskin (2007) is located toward the central part of the lacustrine plain.

Table 2. Percentages of pore pressure restituted in the aquifer-aquitard system after 1000 d of injection.

					r=250 m		r=500 m		r=750 m	
Q_w [m^3s^{-1}]	Unit	z [m]	u_0 [kPa]	Δu_0 [kPa]	Δu_I [kPa]	$\Delta u_I/\Delta u_0$ [%]	Δu_I [kPa]	$\Delta u_I/\Delta u_0$ [%]	Δu_I [kPa]	$\Delta u_I/\Delta u_0$ [%]
0.002	UC	23.5	182.8	26.4	4.99	18.90	1.66	6.29	0.60	2.27
	HL	31.5	224.8	60.8	15.69	25.80	6.00	9.87	2.48	4.08
	LC	38.0	282.4	62.4	4.48	7.18	1.58	2.53	0.62	0.99
0.004	UC	23.5	182.8	26.4	9.97	37.76	3.33	12.61	1.20	4.54
	HL	31.5	224.8	60.8	31.38	51.61	12.02	19.77	4.96	8.16
	LC	38.0	282.4	62.4	8.96	14.36	3.16	5.06	1.24	1.99

Table 3. Computed pore pressure restoration rates.

			r=250 m	r=500 m	r=750 m
Q_w [m^3s^{-1}]	*Unit*	z [m]	r_u [kPa/year]	r_u [kPa/year]	r_u [kPa/year]
0.002	UC	23.5	1.82	0.61	0.22
	HL	31.5	5.73	2.19	0.91
	LC	38.0	1.64	0.58	0.23
0.004	UC	23.5	3.64	1.21	0.44
	HL	31.5	11.45	4.39	1.81
	LC	38.0	3.27	1.15	0.45

Head buildup in aquifers

Head buildup in aquifers at a distance of 15 m from the injection well center is plotted in Figure 9 as a function of time for an injection rate of 0.004 m^3s^{-1}. As expected, higher head buildup is induced in the injection aquifer (HL, triangles) than in the deep deposits (DD, diamonds). A steady state condition in the injection aquifer is not reached before 10000 d of injection. Thus, a steady state flow condition through the hard layer is not as easily reached as some authors (e.g. Zeevaert, 1982) indicate. After 100 d of injection, head buildup starts developing in the DD (diamonds), but the increments are very small. After 10000 d of injection, the head buildup is lower than 1 m. Therefore, for injection periods shorter than 10000 d, it seems sufficient to measure head buildup in the injection aquifer only during underground injection tasks, since negligible changes in head buildup within the DD should be expected.

Leakage rates through aquitards

Figure 10 plots leakage rates crossing the bottom (squares) and top (triangles) boundaries of the HL as a function of time for an injection rate of 0.004 m^3s^{-1}. From a short period of time after the beginning of injection to 1000 d, the rate of water crossing both boundaries increases. Higher leakage rates cross the top boundary of the injection aquifer during this period of time because the UC formation is more permeable. After 1000 d of injection leakage rates that cross the upper boundary increase and leakage rates that cross the lower boundary decrease because the UC formation has greater storage capacity. Note that such decrement in leakage rates is associated with a decrement in the leakage rates within the DD (Figure 11) because of flow continuity. As the injection period becomes longer, comparatively large amounts of water seep through the UC formation. Leakage rates crossing the bottom boundary of the injection aquifer are lower than 0.001 m^3s^{-1} even for long injection periods.

Figure 11 presents the behavior of leakage rates crossing the top boundary of the DD as a function of time. Again, the injection rate is equal to 0.004 m^3s^{-1}. A quite short period of time (100 d) is needed for the injection of the HL to influence the DD because the thickness of the LC formation is quite small (only 8 m). From 100 d to 1000 d of injection, leakage rates increase. However, a rather small leakage rate (lower than 0.000008 m^3s^{-1}), reaches the DD after 1000 d of injection. As the injection period increases, this leakage rate tends to a very small value. This is in agreement with Figure 9 for DD results. At time t=10000 d, head buildup seems constant. Note that the decrement in leakage rates for longer periods of time corresponds to the steady state condition that is reached in the UC formation, as the leakage rate in the upper aquitard tends to the injection rate value. Considering the leakage rate crossing the LC formation, an insignificant influence is expected of the injected water on the physical-chemistry composition of the native water in the DD, provided the injected and native water are compatible in quality.

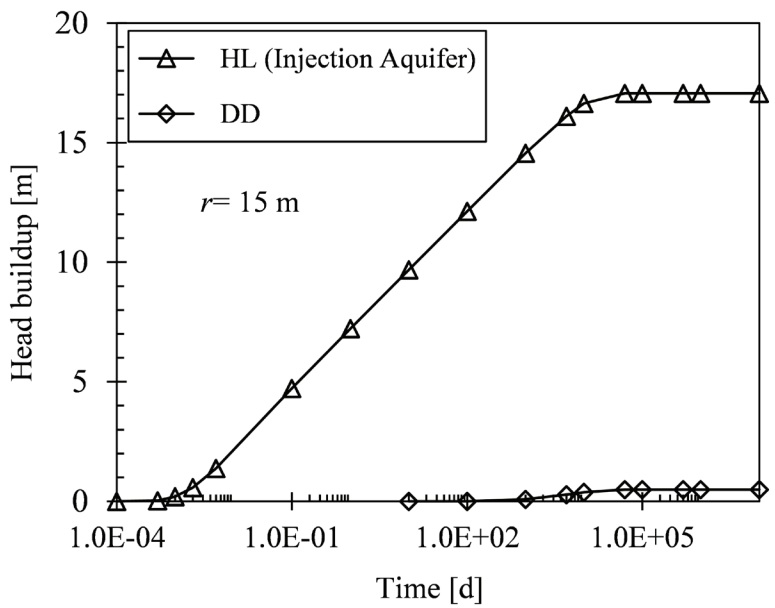

Figure 9. Estimated head buildup versus time for the injection aquifer (HL) and the Deep Deposits (DD).

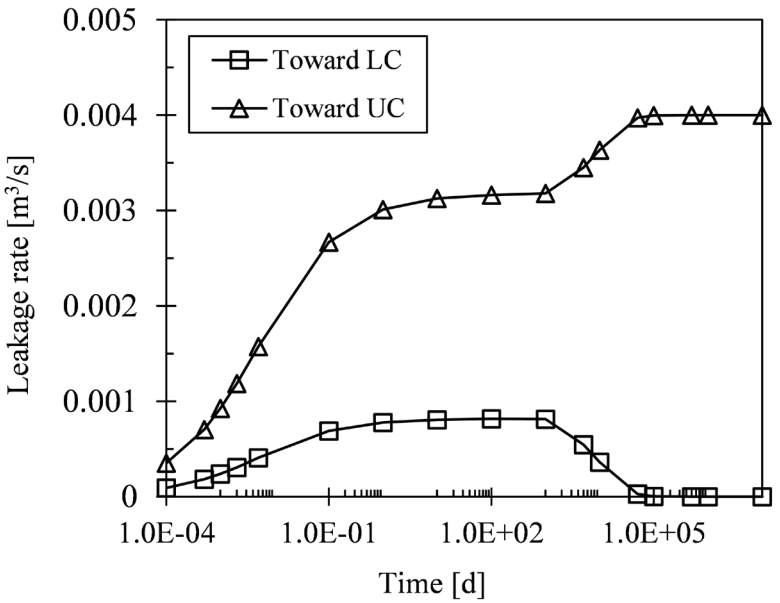

Figure 10. Leakage rates crossing the bottom (squares) and top (triangles) boundaries of the injection aquifer as a function of time.

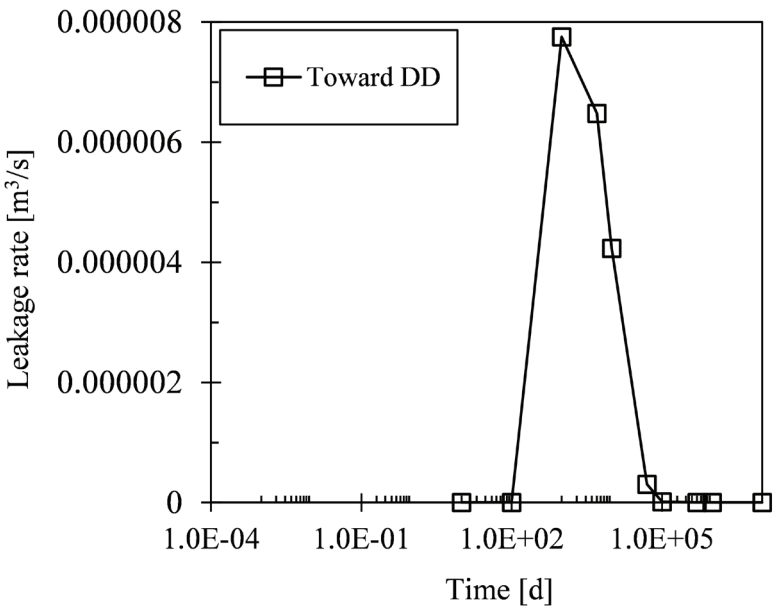

Figure 11. Leakage rates crossing the top boundary of the deep deposits (DD) as a function of time.

Conclusions

In this paper, a purpose-specific strategy for the land subsidence mitigation of Mexico City was suggested. This strategy consists of rising depleted pore pressure in the shallow aquifer beneath Mexico City to induce a diffusion process through the upper and lower aquitards. This diffusion process then generates increments of pore pressure in the system to counteract current pore pressure declines associated to groundwater withdrawals from the main aquifer unit. The analysis of this strategy was conducted under transient flow conditions on the basis of analytical solutions and typical hydraulic parameters for the shallow aquifer-aquitard system beneath Mexico City subject to one injection well. The results of the analysis comprise pore pressure responses in the entire system, head buildup in aquifers and leakage rates through aquitards. The main results of this analysis can be summarized as follows:

1. The transmissivity of the injection formation dominates the amount of pore pressure that is generated at the interface

between the injection aquifer and the upper and lower clay formations near the injection well center.

2. For a give transmissivity of the injection aquifer, injection rate and injection period determine the distance at which pore pressure is propagated through the system. The greater the injection rate and the longer the injection period, the longer the distances pore pressure is propagated through the system in both directions. Considering average values for the hydraulic parameters of the shallow aquifer-aquitard system beneath Mexico City and an injection rate of 0.002 m^3s^{-1}, pore pressure increments are observed 800 m away from the injection well center after 1000 d of injection and well beyond 1000 m after 5000 d of injection.

3. Computed pore pressure restoration rates are significantly higher than the pore pressure depletion rates measured in the field by some research (Ovando *et al*., 2003). Our results are representative of one injection well outside the influence range of any pumping well into the deeper production aquifer.

4. The injection into the shallow aquifer has a minor influence on the head buildup of the deep deposits. After 10000 d of injection, head buildup is lower than 1 m. Furthermore, contrary to some authors' suggestions (Zeevaert, 1982), a steady state condition in the injection aquifer is not easily reached in the short-term. This may take more than 10000 d of injection.

5. The amount of water that is transferred from the injection aquifer to the deep deposits through the lower clay formation is very small. As the injection period increases, this rate tends to zero because the leakage rate in the upper clay formation tends to the injection rate value. Thus, most of the injected water is transferred to the upper clay formation as the injection period increases.

The strategy for land subsidence mitigation advanced here is strongly based on well-established theoretical principles and has been implemented in several cities around the world with success. The benefits of controlling land subsidence in Mexico City are so immense that our strategy is worthy of further exploration. A first estimate of its benefits was provided here. Furthermore, the results reported in this paper are central in designing a field injection test into the shallow aquifer-aquitard system beneath Mexico City. However, it is recognized that in practice the hydraulic responses of the system may be influenced by any pumping well into the production aquifer near the test site, specifically in those locations of the shallow aquifer-aquitard system that remain confined (Carrera and Gaskin, 2007). Therefore, it is recommended to improve the results of the present contribution by accounting for the influence of pumping wells in further analysis.

Acknowledgements

The authors thank Dr. Abdullah Cihan, at Lawrence Berkeley National Laboratory, for provide us with the FORTRAN code ASLMA. We specially thank the two anonymous reviewers for the constructive comments, suggestions and improvements done to the original version of the manuscript.

References

Amelung, F., Galloway, D. L., Bell, J. W., Zebker, H. A. and Laczniak, R. J. (1999). Sensing the ups and downs of Las Vegas: InSAR reveals structural control of land subsidence and aquifer-system deformation. *Geology*, 27(6), pp. 483–486.

Auvinet, G., Méndez, E. and Juárez, M. (2013). Soil fracturing induced by land subsidence in Mexico City, Proceedings of the 18th International Conference on Soil Mechanics and Geotechnical Engineering, Paris, pp. 2921-2924.

Auvinet, G., Méndez, E. and Juárez, M. (2017). El subsuelo de la Ciudad de México, Vol. 3, Supplement to the Third Edition of the book by R.J. Marsal y M. Mazari, Instituto de Ingeniería, UNAM.

Bell, J. W., Amelung, F. Ferretti, A., Bianchi, M. and Novali, F. (2008). Permanent scatterer InSAR reveals seasonal and long-term aquifer-system response to groundwater pumping and artificial recharge, *Water Resources Research*, 44, W02407.

Carrera-Hernández, J. J. and Gaskin, S. J. (2007). The Basin of Mexico aquifer system: regional groundwater level dynamics and database development, *Hydrogeology Journal*, 15, pp. 1577–1590.

Carrera-Hernández, J. J. and Gaskin, S. J. (2009). Water management in the Basin of Mexico: current state and alternative scenarios, *Hydrogeology Journal*, 17, pp. 1483–1494.

Cheng, A. H.-D., and Morohunfola, O. K. (1993). Multilayered leaky aquifer systems: Pumping well solutions, *Water Resources Research*, 29(8), pp. 2787–2800.

Churchill, R. V. (1966). Operational mathematics, 2nd Edition, McGraw-Hill.

Cihan, A., Zhou, Q. and Birkholzer, J. T. (2011a). Analytical solutions for pressure perturbation and fluid leakage through aquitards and wells in multilayered-aquifer systems, *Water Resources Research*, 47, W10504.

Cihan, A., Zhou, Q. and Birkholzer, J. T. (2011b). User Guide for Analytical Solution of Hydraulic Head Changes, Focused and Diffuse Leakage in Multilayered Aquifers (ASLMA), Ernest Orlando Lawrence Berkeley National Laboratory, Earth Sciences Division, pp. 72.

Conagua, (2006). Hacia una estrategia de manejo sustentable de agua en el Valle de México y su zona metropolitana, Gerencia regional XIII, Aguas del Valle de México y Sistema Cutzamala, Comisión Nacional del Agua, México, D.F.

Conagua (2009). Actualización de la disponibilidad media anual de agua subterránea: Acuífero (0901) Zona Zetropolitana de la Cd. de México, Diario oficial de la Federación.

Cruickshank, G. G. (1998). Proyecto Lago de Texcoco: Rescate hidrogeológico, Comisión Federal de Electricidad, CFE, México, D.F.

De Cserna, Z., Aranda-Gómez, J.J., Mitre-Salazar, L.M. (1988). Estructura geológica, gravimetría, sismicidad y relaciones neotectónicas regionales de la cuenca de México: *Boletín del Instituto de Geología*, UNAM, México, 104, 1–71.

DGCOH (1997). Estudio de factibilidad para el reúso de las aguas residuales y pluviales del Valle de México para satisfacer la demanda de agua potable a mediano plazo, a través de la recarga de acuíferos, Instituto de Ingeniería, UNAM.

DGCOH and Lesser (1991). Recarga artificial de agua residual tratada al acuifero del Valle de Mexico, *Ingeniería Hidráulica en México*, pp. 65–70.

Domenico, P. A. and Mifflin, M.D. (1965). Water from low-permeability sediments and land subsidence, *Water Resources Research*, 1(4), pp. 563-576.

Downs, T. J., Mazari-Hiriart, M., Dominguez-Mora, R. and Suffet, I. H. (2000). Sustainability of least cost policies for meeting Mexico City's future water demand, *Water Resources Research*, 36(8), pp. 2321-2339.

Durazo, J. and Farvolden, R. N. (1989). The groundwater regime of the Valley of Mexico from historic evidence and field observations, *Journal of Hydrology*, 112, pp. 171-190.

Enciso-de la Vega, S. (1992). Propuesta de nomenclatura estratigráfica para la cuenca de México, Universidad Nacional Autónoma de México. Instituto de Geología, *Revista*, 10(1), pp. 26–36.

Fries, C. (1960). Geologia del estado de Morelos y de partes adyacente de Mexico y Guerrero, region central meridional de Mexico: Instituto de Geologia, UNAM, Boletin 60, pp. 236.

Gambolati, G., and Teatini, P. (2014). Venice Shall Rise Again—Engineered Uplift of Venice Through Seawater Injection, Elsevier Insights, 100 pp., Elsevier, Amsterdam, Netherlands.

González-Nicolás, A., Baù, D., Cody, B. M., and Alzraiee, A. (2015). Stochastic and global sensitivity analyses of uncertain parameters affecting the safety of geological carbon storage in saline aquifers of the Michigan Basin, *International Journal of Greenhouse Gas Control*, 37, pp. 99-114.

Herrera, I. and Figueroa, G. E. (1969). A correspondence principle for the theory of leaky aquifers, *Water Resources Research*, 5, pp. 900-904.

Herrera, I. (1970). Theory of multiple leaky aquifers, *Water Resources Research*, 6, pp. 185-193.

Herrera, I. (1976). A review of the integrodifferential equations approach to leaky aquifer mechanics, In: Advaces in groundwater hydrology, Ed. Z Saleem, Am. Water Resources Association, pp. 29-47.

Herrera, I., Martínez, R. and Hernández, G. (1989). Contribución para la Administración Científica del Agua Subterránea de la Cuenca de México, *Geofísica Internacional*, 28, pp. 297-334.

Huizar-Álvarez, R., Ouysse, S., Espinoza-Jaramillo, M. M., Carrillo-Rivera, J. J. and Mendoza-Archundia, E. (2016). The effects of water use on Tothian flow systems in the

Mexico City conurbation determined from the geochemical and isotopic characteristics of groundwater, *Environmental Earth Sciences*, 75:1060, pp. 1-17.

Hunt, B. (1985). Flow to a well in a multiaquifer system, *Water Resources Research*, 21, pp. 1637–1641.

Jiménez, C. B., Mazari, H. M., Domínguez, M. R. and Cifuentes, G. E. (2004). El Agua en el Valle de Mexico, In: El agua en Mexico vista desde la academia, Academia Mexicana de Ciencias, Mexico, D.F., pp. 15-32.

Marsal, R. and Mazari, M. (1959). The Subsoil of Mexico City, Contribution to First Pan-American Conf. on Soil Mechanics and Found. Engineering, Facultad de Ingeniería, UNAM, Mexico, 1 and 2.

Mazari, M. and Mackey, D. M. (1993). Potential for groundwater contamination in Mexico City, *Environmental Science and Technology*, 27(5), pp. 794-802.

Mooser, F. (1975). Historia geológica de la Cuenca de México, *In*: Memoria de las obras de drenaje profundo del Distrito Federal, México, D.F., Departamento del Distrito Federal, 38 p.

Mooser, F. and Molia, (1993). Nuevo modelo hidrogeológico para la Ciudad de México, Boletín del Centro de Investigación Sísmica de la Fundación Javier Barros Sierra, 3(1), México.

Neuman, S. P. and Witherspoon, P. A. (1969). Coupled solution for forced recharge in confined aquifers, *Water Resources Research*, 5, pp. 803-816.

NOM-014-CONAGUA-2007. Requisitos para la recarga artificial de acuíferos con agua residual tratada.

NOM-015-CONAGUA-2007. Infiltración artificial de agua a los acuíferos. Características y especificaciones de las obras y del agua.

NRC (1995). Mexico City's water supply: improving the outlook for sustainability. National Academy of Sciences, Washington, DC.

Ortega, G. A. and Farvolden, R. N. (1989). Computer analysis of regional groundwater flow and boundary conditions in the Basin of Mexico, *Journal of Hydrology*, 110, pp. 271-294.

Ortega, G. A., Rudolph, D. L. and Cherry, J. A. (1999). Analysis of long-term land subsidence near Mexico City: Field investigations and predictive modeling, *Water Resources Research*, 35(11), pp. 3327-3341.

Otott, G.E. and Clarke, D.D., (1996). History of the Wilmington field—1986–1996. In: AAPG Pacific Section, Old Oil Fields and New Life: A Visit to the Giants of the Los Angeles Basin, pp. 17–22.

Ovando-Shelley, E., Romo, M. P., Contreras, N. and Giralt, A. (2003). Effects on soil properties of future settlements in downtown Mexico City due to ground water extraction, *Geofísica Internacional*, 42(2), pp. 185-204.

Ovando-Shelley, E., Ossa, A., and Santoyo, E. (2013). Effects of regional subsidence and earthquakes on architectural monuments in Mexico City, *Boletín de la Sociedad Geológica Mexicana*, 65(1), pp. 157-167.

Phien-wej, N., Giao, P.H. and Nutalaya, P. (1998). Field experiment of artificial recharge through a well with reference to land subsidence control, *Engineering Geology*, 50, pp. 187–201.

Poland, J. F. (1972). Subsidence and its control, *In*: Underground Waste Management and Environmental Applications, Cook, T. D. ed., The American Association of Petroleum Geologists, Oklahoma, USA. pp. 50-71.

Poland, J. F. (1984). Guidebook to studies of land subsidence due to groundwater withdrawal, 305 pp., UNESCO, Paris.

Reséndiz, D., Auvinet, G. Méndez, E. (2016). Subsidencia de la Ciudad de México: un proceso centenario insostenible, Instituto de Ingeniería, UNAM, pp. 29.

Rudolph, D. L., Herrera, I. and Yates, R. (1989). Groundwater flow and solute transport in the industrial well fields of the Texcoco saline aquifer system near Mexico City, *Geofísica Internacional*, 28(2), pp. 363–408.

Rudolph, D. L., Cherry, J. A. and Farvolden, R. N. (1991). Groundwater flow and solute transport in fractured lacustrine clay near Mexico City, *Water Resources Research*, 27(9), pp. 2187-2201.

Rudolph, D. L. and Frind, E. O. (1991). Hydraulic response of highly compressible aquitards during Consolidation, *Water Resources Research*, 27(1), pp. 17-30.

Schlaepfer, C. (1968). Hoja Mexico 14Q-h(5), con resumen de la geologia de la hoja Mexico, Distrito Federal y estados de Mexico y Morelos: Instituto de Geologia, UNAM, Carta Geologica de Mexico, Serie de 1:100,000, mapa con texto explicativo en el reverso.

Shi, X., Jiang, S., Xu, H., Jiang, F., He, Z. and Wu, J. (2016). The effects of artificial recharge of groundwater on controlling land subsidence and its influence on groundwater quality and aquifer energy storage in Shanghai, China, *Environmental Earth Sciences*, 75(195), pp. 1-18.

Teatini, P., Ferronato, M., Gambolati, G., Baù, D. and Putti, M. (2010). Anthropogenic Venice uplift by seawater pumping into a heterogeneous aquifer system, *Water Resources Research*, 46, W11547.

Teatini, P., Castelletto, N., Ferronato, M., Gambolati, G. and Tosi, L. (2011). A new hydrogeologic model to predict anthropogenic uplift of Venice, *Water Resources Research*, 47, W12507.

Terzaghi, K. (1925). Principles of soil mechanics, IV—Settlement and consolidation of clay. *Eng. News. Rec.* 95:874–878.

Tolman, C. F. and Poland, J. F. (1940). Groundwater, salt water, infiltration, and ground surface recession in Santa Clara Valley, Santa Clara County, California, American Geophysical Union, pp. 23–34.

Vargas, C. and Ortega, G. A. (2004). Fracture hydraulic conductivity in the Mexico City clayey aquitard: Field piezometer rising-head tests, *Hydrogeology Journal*, 12, pp. 336–344.

Vázquez, S. E. and Jaimes, P. R. (1989). Geología de la Cuenca de México, *Geofísica Internacional*, 28(2), pp. 133–174.

World Bank (2013). Urban Water in the Valley of Mexico: A Green path for Tomorrow. Mexico City, Report 75917, The Word Bank, Washington, USA.

Zhang, Y., Wu, J., Xue, Y., Wang, Z., Yao, Y., Yan, X., and Wang, H. (2015). Land subsidence and uplift due to long-term groundwater extraction and artificial recharge in Shanghai, China, *Hydrogeology Journal*, 23, pp. 1851–1866.

Zhou, Q., Birkholzer, J. T. and Tsang, C. F. (2009). A semi-analytical solution for large-scale injection-induced pressure perturbation and leakage in a laterally bounded aquifer-aquitard system, *Transport in Porous Media*, 78(1), pp. 127–148.

Zhou, X. and Burbey, T. J. (2014). Deformation characteristics of a clayey interbed during fluid injection, *Engineering Geology*, 183, pp. 185–192.

Zeevaert, L. (1982). Foundation Engineering for Difficult Subsoil Conditions, 2nd ed., Van Nostrand-Reynhold Company, New York, NY, USA.